UNIVERSIDADE FEDERAL DE SANTA CATARINA
CAMPUS TRINDADE
PROGRAMA DE PÓS-GRADUAÇÃO EM ENGENHARIA MECÂNICA

Oscar Javier Ospina Pineda

INVESTIGATION OF THE MEASUREMENT OF THROUGH-THICKNESS RESIDUAL STRESS BY COMBINING DIGITAL SPECKLE PATTERN INTERFEROMETRY AND THE SLITTING METHOD

Florianópolis
2020

Oscar Javier Ospina Pineda

INVESTIGATION OF THE MEASUREMENT OF THROUGH-THICKNESS RESIDUAL STRESS BY COMBINING DIGITAL SPECKLE PATTERN INTERFEROMETRY AND THE SLITTING METHOD

Submitted in partial fulfillment of the requirements for the degree of Master of Science in Mechanical Engineer, in the Mechanical Engineer Program at Universidade Federal de Santa Catarina.

Advisor: Prof. Armando Albertazzi Gonçalves Jr., Dr. Eng.

Joint advisors:
Matias Roberto Viotti, Dr. Eng.
Celso Luiz Nickel Veiga, Dr. Eng.

Florianópolis
2020

Identification form of the Dissertation

Ospina, Oscar
INVESTIGATION OF THE MEASUREMENT OF THROUGH-THICKNESS RESIDUAL STRESS BY COMBINING DIGITAL SPECKLE PATTERN INTERFEROMETRY AND THE SLITTING METHOD / Oscar Ospina ; orientador, Armando Albertazzi Gonçalves Jr., coorientador, Matias Roberto Viotti, coorientador, Celso Luiz Nickel Veiga, 2020.
89 p.

Dissertação (mestrado) - Universidade Federal de Santa Catarina, Centro Tecnológico, Programa de Pós-Graduação em Engenharia Mecânica, Florianópolis, 2020.

Inclui referências.

1. Engenharia Mecânica. 2. Tensões Residuais. 3. Interferometria. I. Albertazzi Gonçalves Jr., Armando . II. Viotti, Matias Roberto. III. Nickel Veiga, Celso Luiz IV. Universidade Federal de Santa Catarina. Programa de Pós Graduação em Engenharia Mecânica. V. Título.

Oscar Javier Ospina Pineda

INVESTIGATION OF THE MEASUREMENT OF THROUGH-THICKNESS RESIDUAL STRESS BY COMBINING DIGITAL SPECKLE PATTERN INTERFEROMETRY AND THE SLITTING METHOD

This Master Dissertation was evaluated and approved by the following examination committee:

Prof. Armando Albertazzi Gonçalves Jr., Dr. Eng. – Advisor
Universidade Federal de Santa Catarina

Prof. Tiago Loureiro Figaro da Costa Pinto, Dr. Eng.
Universidade Federal de Santa Catarina

Prof. Marco Antonio Martins Cavaco, Ph.D.
Universidade Federal de Santa Catarina

Prof. Cristiano Binder, Dr. Eng.
Universidade Federal de Santa Catarina

We certify that this is the **original and final version** of the dissertation that was approved to obtain the degree of Master of Science in Mechanical Engineer.

Documento assinado digitalmente
Jonny Carlos da Silva
Data: 06/04/2020 14:38:17-0300
CPF: 514.515.064-49

Prof. Jonny Carlos da Silva, Dr. Eng.
POSMEC Coordinator

Armando Albertazzi Goncalves Junior:23249501549

Assinado de forma digital por Armando Albertazzi Goncalves Junior:23249501549
Dados: 2020.04.05 20:05:07 -03'00'

Prof. Armando Albertazzi Gonçalves Jr., Dr. Eng.
Advisor

Florianópolis, 2020.

Dedicated to my beloved Parents

Lily and Oscar.

ACKNOWLEDGEMENTS

I would like to thank above all my advisor Prof. Armando Albertazzi Gonçalves Jr. His guidance and support were essential to do this work, I am fortunate to have had him as my research advisor.

I would also like to thank my joint advisors Dr. Matias Roberto Viotti and Dr. Celso Luiz Nickel Veiga for their continued help and assistance during the course of the research. It has been a great pleasure working with them.

My special thanks go to Dr. Mike Prime, of Los Alamos National Laboratory, for his invaluable contribution. I really appreciate his willing.

I would like to thank my colleagues, professors, and all the staff of the LABMETRO for the support and encouragement I have received during this time.

I want to express my gratitude towards LABCONF, where were carried out the normalizing treatments of the beams.

I also extend my gratitude toward PETROBRAS for funding my Master project and providing all the financial support needed to carry out the experiments.

Finally, I would like to thank my family and friends for their support and encouragement throughout all my life. Especially to my parents, who have inspired me to chase my dreams and never give up. I take the opportunity to give special thanks to my brother and two sisters, their love and support have been very important to go ahead.

RESUMO

O transporte de petróleo e gás do fundo do mar até a superfície em campos *offshore* de aguas profundas é possível mediante dutos não rígidos conhecidos como *risers* flexíveis. A flexibilidade é importante para suportar movimentos de maré, correntes marinhas e ondulações sem comprometer sua integridade. Esses dutos são muitos complexos do ponto de vista construtivo. Possuem internamente uma armadura de tração formada por arames de seção transversal retangular dispostos em forma de hélice, responsáveis de proporcionar resistência mecânica. Para garantir um ótimo funcionamento e evitar falhas estruturais, é necessário conhecer o estado de tensões nos arames que compõem essa armadura. A tensão total que atua nesses arames é dada pela soma da tensão aplicada (devido às condições de operação) e da tensão residual (que resulta do processo de fabricação). As tensões aplicadas podem ser medidas em tempo real usando equipamentos especiais, porém os resultados obtidos não levam em consideração as tensões residuais, o que pode gerar riscos em relação a integridade estrutural do *riser*. Desenvolver e validar uma metodologia apropriada para medir tensões residuais nos arames de tração do *riser* flexível foi a principal motivação para a realização desta pesquisa. O objetivo principal do trabalho é implementar a técnica *slitting* junto com interferometria *speckle* para determinar o perfil de tensões residuais em toda a seção transversal do material. Para validar o procedimento foram preparados corpos de prova com perfis de tensões conhecidos mediante um esquema de flexão a quatro pontos. Os resultados obtidos mostram perfis parecidos aos esperados com diferenças na região próxima à superfície. Embora tenha sido possível validar o procedimento de medição, o trabalho deixa claro que é necessário aperfeiçoar o procedimento experimental para atingir melhores resultados.

Palavras-chave: tensões residuais, *slitting*, interferometria *speckle*.

RESUMO EXPANDIDO

Introdução

Os *risers* flexíveis são dutos usados para transportar fluidos desde o fundo do mar até a superfície em campos *offshore*. Eles possuem internamente várias camadas, entre elas uma armadura de tração responsável de proporcionar resistência mecânica. As falhas estruturais nos *risers* flexíveis acontecem geralmente pelo dano dos arames que compõem a armadura de tração. O principal mecanismo de falha é a fadiga devido aos movimentos aleatórios da plataforma. Como consequência disso a armadura de tração pode estourar, o que poderia causar a ruptura definitiva do duto, tendo isto consequências catastróficas tanto pela vida e segurança dos trabalhadores, mas também obviamente pelo grande prejuízo ambiental. As falhas na armadura de tração acontecem pela soma da tensão aplicada (devido às condições de operação) e da tensão residual (que resulta do processo de fabricação), portanto é necessário conhecer o estado de tensões dos arames desta armadura. As tensões aplicadas podem ser medidas em tempo real usando equipamentos especiais, porém os resultados não levam em consideração as tensões residuais, o que pode gerar riscos em relação à integridade estrutural do *riser*.

As tensões residuais geralmente são avaliadas mediante um alivio de tensões. Existem diferentes técnicas desenvolvidas para tal fim. Entre elas, aquela conhecida como *slitting* tem ganhado relevância devido a que permite calcular as tensões residuais na seção transversal do material. Para isso é necessário cortar uma parte do material e medir as deformações causadas por esse alivio. Posteriormente inserindo as medições num modelo matemático é possível reconstruir o perfil de tensões presente no material antes de ser cortado.

As deformações geradas pelo corte podem ser medidas utilizando a técnica conhecida como interferometria *speckle*, a qual aproveita as características das superfícies e o comprimento de onda do laser para medir pequenos deslocamentos que podem ser transformados em deformações.

O que motivou então esta pesquisa foi o desenvolvimento de uma metodologia que possa ser usada para medir as tensões residuais nos arames que compõem a armadura de tração do *riser*, usando a técnica *slitting* junto com interferometria *speckle*.

Objetivos

O principal objetivo é avaliar a viabilidade do método *slitting* junto com interferometria *speckle* para medir tensões residuais em toda a seção transversal do material. Entre os

objetivos específicos que foram definidos para realizar o trabalho com sucesso destacam-se a preparação de corpos de prova, montagem de sistema ótico, e processamento de imagens.

Metodologia

Para avaliar a viabilidade do método *slitting* junto com interferometria *speckle* inicialmente foi necessário preparar corpos de prova com estados de tensão conhecidos mediante tratamento térmico de normalização, e flexão a quatro pontos. Posteriormente foram realizados três experimentos, dois usando a técnica *slitting* junto com interferometria, e um usando *slitting* junto com um extensômetro, visando comparar a metodologia proposta com a medição tradicional.

Nos dois primeiros experimentos foi usando um interferômetro *speckle* de dupla iluminação com sensibilidade no plano. Os mapas de fase das imagens adquiridas pelo interferômetro foram obtidos mediante o deslocamento de fase usando um PZT acoplado num dos espelhos do interferômetro. As deformações causadas pelo corte foram calculadas fazendo a diferencia de fase entre dois estados consecutivos, e aplicando um algoritmo de remoção do salto de fase.

As tensões residuais foram aproximadas usando um modelo matemático baseado no principio da superposição, usando como funções base polinômios de Legendre desde o grau 2 até o grau 12.

Resultados e Discussão

O experimento 1 mostra um corpo de prova quase zerado em termos de tensões residuais, o que era esperado pois a amostra usada neste experimento foi submetida a um tratamento térmico de normalização para alivio de tensões. Os experimentos 2 e 3 mostram o efeito da flexão a quatro pontos aplicada nas amostras, embora os perfis não sejam exatamente iguais ao esperado, em termos gerais seguem a sua tendência e ordem de grandeza.

O resultado do experimento 2, no qual foram medidas as tensões residuais numa amostra carregada usando *slitting* junto com interferometria *speckle*, é similar ao perfil obtido no experimento 3, no qual foram medidas as tensões residuais numa amostra carregada usando um extensômetro. Isso é bom pois mostra que a metodologia proposta no trabalho fornece resultados parecidos aos obtidos tradicionalmente.

O principal erro que se observa nos resultados é a forma estranha que tem os perfis de tensão nos primeiros passos do corte. Esse comportamento é muito provavelmente devido a tensões

introduzidas pela usinagem da ranhura, porém é necessário um estudo mais aprofundado para conseguir caracterizar este erro.

Considerações Finais

Neste trabalho foi possível validar o procedimento de medição implementando a técnica *slitting* junto com interferometria *speckle*. Porém é necessário aprimorar o procedimento experimental para melhorar os resultados obtidos. A principal modificação a ser realizada é na bancada de corte; deve-se projetar um dispositivo mais robusto e com maior rigidez para assim evitar introduzir tensões indesejadas quando é feita a ranhura. Além disso também é necessário projetar um sistema de flexão a quatro pontos usando roletes nos pontos de carga e de apoio para assim fornecer um estado de flexão pura nos corpos de prova e então poder comparar melhor os resultados obtidos com o perfil inserido.

Palavras-chave: tensões residuais, *slitting*, interferometria *speckle*.

ABSTRACT

The transportation of oil and gas from the seabed to the surface in deep water offshore fields is possible through non-rigid pipes known as flexible risers. Flexibility is important to withstand sea waves and current flows without compromising the integrity of the riser. These pipes are very complex from a constructive point of view. They have an internal tensile armor composed by flat rectangular wires helically wound, responsible for providing mechanical resistance. In order to ensure safe working conditions and avoid structural failures, it is necessary to known the stress state in these tensile armor wires. The total stress in the wires is a combination of the stress created by external loads (during service) and the residual stress (arose from the manufacturing process). The external loads can be measured in real-time by using special equipment, however the obtained results do not take into account the residual stresses, which could be a problem regarding to the structural integrity of the riser. The motivation of this research was to develop and validate a methodology to measure residual stresses in the tensile armor wire of the riser. The aim of the work is to implement the slitting technique combined with digital speckle pattern interferometry to measure through-thickness residual stress in steel specimens. To validate the measurement process, beam samples with known stress profiles were prepared by means a four-point bending scheme. The obtained results show similar profiles to those expected with differences in the near-surface region. Although it was possible to validate the measurement process, it is clear that improvements in the experimental procedure should be done in order to achieve better results.

Keywords: residual stress, slitting, digital speckle pattern interferometry.

LIST OF FIGURES

Figure 1.1 – Typical subsea production system 15
Figure 2.1 – Flexible riser stored on reel 21
Figure 2.2 – Standard flexible riser configurations 21
Figure 2.3 – Typical flexible riser components. 22
Figure 2.4 – Section of a formed tensile wire 23
Figure 2.5 – Fabrication Process for the tensile armor. a) Wire-rewinding; b) Wire wrapping in the tensile armor machine 24
Figure 2.6 – Tensile armor machine 24
Figure 2.7 – Broken tensile armor wires due to tensile fatigue 25
Figure 2.8 – a) Radial buckling; b) Lateral buckling in the tensile armor of a flexible riser 26
Figure 2.9 – a) Welding process; b) Weld metal shrinks more than the surrounding; c) Residual stresses are created to maintain dimensional continuity 27
Figure 2.10 – Superimposing of residual stress and service stress 27
Figure 2.11 – Compact sensor to measure residual stress by combining hole-drilling and DSPI. SB (Supporting base), DM (Drilling module), MM (Measurement module) 30
Figure 2.12 – Miniature X-ray diffractomer 32
Figure 2.13 – Coordinate system and terminology for slitting method 33
Figure 2.14 – Legendre polynomials of various orders: a) $j = 2$; b) $j = 6$; c) $j = 8$; and d) $j = 12$ 37
Figure 2.15 – Slitting model used in [40] 38
Figure 2.16 – Compliances functions when a zero width slit is introduced in a flat block with $E = 1$ and $\nu = 0.3$ for various input stress: a) $L_2(x)$, b) $L_6(x)$, c) $L_8(x)$, and d) $L_{12}(x)$ 38
Figure 2.17 – Unite pulse functions used for residual stress calculation 39
Figure 2.18 – Physical interpretation of the compliances for the unite pulse functions 40
Figure 2.19 – a) Light scattered from a rough surface [13]; b) Typical simulated speckle distribution 43
Figure 2.20 – Correlation fringes 45
Figure 2.21 – Two-beam arrangement for in-plane sensitivity 46
Figure 2.22 – Steps to analyze DSPI specklegram 47
Figure 2.23 – Unwrapped and wrapped phases 49
Figure 2.24 – a) Phase difference map before phase unwrapping ($\Delta\phi_w$); b) Phase difference map after phase unwrapping ($\Delta\phi$) 50

Figure 3.1 – Steel beams specimens 52
Figure 3.2 – Four-point bending of beams 2 and 3 53
Figure 3.3 – Expected residual stress profile after four-point bending 54
Figure 3.4 – Near-surface residual stress measurement for specimens 1 and 2 by hole-drilling (POLAR) 54
Figure 3.5 – Blind holes drilled in specimens 1 and 2 55
Figure 3.6 – Clamped specimen 56
Figure 3.7 – Cutting workbench 57
Figure 3.8 – Milling cutter 58
Figure 3.9 – Dual beam interferometer 59
Figure 3.10 – Procedure to obtain the phase maps 60
Figure 3.11 – Procedure to obtain the wrapped phase difference 61
Figure 3.12 – First nine wrapped phase differences for experiment 1 (relieved beam) 62
Figure 3.13 – First nine wrapped phase differences for experiment 2 (loaded beam) 62
Figure 3.14 – a) Wrapped phase difference; b) Filtered wrapped phase difference; c) Unwrapped (absolute) phase difference 63
Figure 3.15 – Pixel-mm relation of the interferometer 64
Figure 3.16 – a) Area of interest; b) Selected points 65
Figure 3.17 – Cumulative strains in experiment 1 (relieved beam) 68
Figure 3.18 – Cumulative strains in experiment 2 (loaded beam) 68
Figure 3.19 – Strain gage glued in the surface opposite the slit 69
Figure 3.20 – Experiment 3 (slitting – strain gage) 70
Figure 3.21 – Cumulative strains in experiment 3 (loaded beam) 71
Figure 3.22 – Cumulative strains in the three experiments 72
Figure 4.1 – Residual stress profile as function of depth for specimen 1 74
Figure 4.2 – Residual stress distributions as function of depth for specimen 1. Comparison of the results estimated using both, Legendre and unite pulse approaches 75
Figure 4.3 – Residual stress distributions as function of depth for specimen 1. Comparison between slitting and hole-drilling results 76
Figure 4.4 – Residual stress profiles as function of depth for specimen 2. Comparison between expected and calculated distribution 77
Figure 4.5 – Residual stress distributions as function of depth for specimen 2. Comparison of the results estimated using both, Legendre and unite pulse approaches 78

Figure 4.6 – Residual stress distributions as function of depth for specimen 2. Comparison between slitting and hole-drilling results 79
Figure 4.7 – Residual stress profiles as function of depth for specimen 3. Comparison between expected and calculated distribution 80
Figure 4.8 – Residual stress profiles as function of depth for the three specimens. The profiles were estimated using Legendre polynomials 81

LIST OF TABLES

Table 3.1 – Dimensions and stress condition for the beam specimens 52
Table 3.2 – Components of the interferometer 59
Table 3.3 – Cumulative strains in experiment 1 (relieved beam) 66
Table 3.4 – Cumulative strains in experiment 2 (loaded beam) 67
Table 3.5 – Cumulative strains in experiment 3 (loaded beam). 70

LIST OF ABBREVIATIONS

ASTM	American Society for Testing and Materials
CCD	Charged Coupled Device
DSPI	Digital Speckle Pattern Interferometry
EDM	Electric Discharge Machine
LABMETRO	Metrology and Automation Laboratory
ND	Neutron Diffraction
OPD	Optical Path Difference
POLAR	Portable Optical Laser-based device for Residual stress measurement
PZT	Piezoelectric ceramic material
XRD	X-ray Diffraction

LIST OF SYMBOLS

Latin alphabet:

A_j	Amplitude coefficients
$\{A\}$	Vector of amplitude coefficients
a	Slit depth
C_j	Compliance functions
$[C]$	Compliance matrix
d	Displacement of the surface
E	Young modulus
k	Sensitivity vector of the interferometer
k_1, k_1	Illumination vectors of the interferometer
I	Intensity distribution of a specklegram
I_0	Background intensity of a specklegram
$I_1,\ I_2$	Intensities of the interfering beams
I_{12}	Intensity distribution of the fringe pattern
I_{of}	Average intensity of the fringe pattern
L_j	Legendre polynomials basis
$[L]$	Legendre Matrix
P_j	Basis functions to approximate residual stress
t	Thickness of the material
u_j	Unite Pulse Functions
V_f	Contrast of the fringes

Greek alphabet:

γ	Illumination angle of the interferometer
$\Delta\phi$	Phase variation between two specklegrams (unwrapped phase map difference)
$\Delta\phi_w$	Wrapped phase map difference
ε	Expected strains
$\{\varepsilon\}$	Vector of expected strains
ε_{meas}	Measured strains

$\{\varepsilon_{meas}\}$	Vector of measured strains
σ_R	Residual stress field
σ_S	Service stress field
σ_y	Residual stress component in the *y*-direction (normal to the slit)
$\{\sigma_y\}$	Vector of residual stresses
λ	Wavelength of the laser source
ν	Poisson's ratio
ϕ	Relative phase between the interfering beams (phase map of a specklegram)
ϕ_1, ϕ_1	Phase maps of two different states
$\varphi_1,\ \varphi_2$	Phases of the interfering beams

TABLE OF CONTENTS

1 INTRODUCTION 15
1.1 Background and Motivation 15
1.2 Research Aim and Objectives 18
1.3 Dissertation Structure 18

2 LITERATURE REVIEW 20
2.1 Flexible Risers 20
2.1.1 Tensile Armor 23
2.1.1.1 Main Failure Modes 25
2.2 Residual Stress 26
2.2.1 Residual Stress in Tensile Armor Wires 28
2.2.2 Residual Stress Measurement 29
2.2.2.1 Relaxation Measurement Methods 29
2.2.2.2 Diffraction Methods 31
2.3 The Slitting Method 32
2.3.1 Fundamentals 33
2.3.2 Series Expansion for Approximate Residual Stress 34
2.3.3 Forward Problem: Finite Element Approach 35
2.3.3.1 Legendre Polynomials to Compute the Compliances 36
2.3.3.2 Unite Pulse Functions to Compute the Compliances 39
2.3.4 Inverse Problem: Least Square Fit for Stress Estimation 41
2.3.5 Practical Considerations for Through-Thickness Measurement 42
2.3.5.1 Cutting Method 42
2.3.5.2 Strain Measurement 42
2.4 Digital Speckle Pattern Interferometry 43

2.4.1 In-Plane Sensitivity 46
2.4.2 Acquisition Step: Phase-Shifting 48
2.4.3 Processing Step: Unwrapping of the Phase Difference 48

3 EXPERIMENTAL PROCEDURE 51
3.1 Experimental Planning 51
3.2 Specimens 51
3.3 Cutting Process 56
3.4 Strain Measurement by Using a Dual Beam Interferometer 58
3.4.1 Optical Setup 59
3.4.2 Data Acquisition 60
3.4.3 Strain Calculation: Image Processing 63
3.5 Strain Measurement by Using Strain Gage 69

4 RESULTS AND DISCUSION 73
4.1 Residual Stress Aproximation 73
4.2 Experiment 1: slitting-DSPI (stress-relieved beam) 74
4.3 Experiment 2: slitting-DSPI (loaded beam) 76
4.4 Experiment 3: slitting-strain gage (loaded beam) 79
4.5 Discussion 81

5 CONCLUSIONS AND SUGGESTIONS FOR FUTURE WORK 84

REFERENCES 86

1 INTRODUCTION

1.1 Background and Motivation

Despite of the development of alternative energy sources, oil and gas continue to be the major source of the world´s energy [1]. The growth of the energy consumption over the years has increased the oil demand, leading to search new fields in order to ensure a constant supply.

The exploitation of reservoirs under the seabed by means of oil rigs has been one of the attempts to increase the overall oil and gas production. The development of these fields subject the workers to a hazardous environment because facilities are under extreme conditions combining high pressure, high temperature, and high stresses. Additionally to them, that can put the operation of the whole offshore system at risk, working in sea locations is a challenge in itself because the risk of contamination. Consequently, all components and equipment should be controlled in order to achieve safe working conditions. Figure 1.1 shows a typical subsea production system.

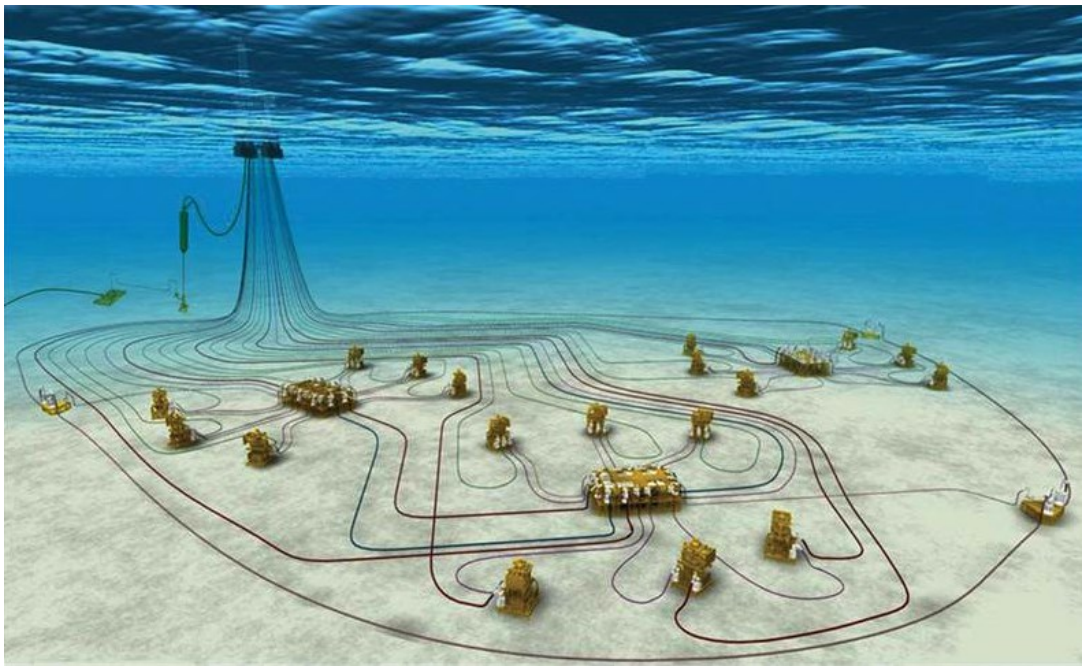

Figure 1.1 Typical subsea production system [2].

A critical matter in offshore fields is the transfer of petroleum and service fluids by linking the seabed to the floating platform. This fact is possible due to special pipes called

risers, which can be rigid or flexible. In deep water locations like pre-salt fields in Brazil, the use of flexible risers is mandatory. The main characteristic of these flexible pipes is their low relative bending resistance to axial stiffness. This is achieved by using a number of layers of different materials in the pipe wall fabrication, which are able to slip past each other when under the influence of applied loads.

During the service life the riser is under dynamic stresses from different sources, introducing challenges with respect to failure modes. A limiting factor of the riser lifetime is the performance of the tensile armor layer that provides resistance to axial loads. One of the major reasons for structural failures in flexible risers is the damage of the wires composing the tensile armors [3].

Failures in the tensile armors can cause the rupture of the riser, having catastrophic consequences. To guaranty the integrity of the pipe, real-time monitoring during operation should be done by a set of techniques and special equipment. However, the internal stresses in the armor material are usually not taken into account for this kind of analysis [3].

The tensile armor is constructed from steel wires that undergo plastic deformations during manufacturing process, setting up residual stresses in the material that are further developed during service life [4, 5]. These internal stresses exist in every type of material independent on the presence of any external load. Residual stresses are self-equilibrated. Thus, tensile and compressive areas are added to create a zero force moment resultant [6]. Due to this particular feature, their presence may not be readily apparent and may be overlooked or ignored during the riser design and operation.

Disregarding residual stresses in the tensile armor could lead to several problems because they could be harmful depending on the sign and location. The total stress in the armor during service is a combination of the residual stress as well as the stresses created by an external loading. Tensile residual stresses are generally detriment. Its addition to applied stresses can cause premature failures in the riser. Alternatively, their contribution can be beneficial when they are compressive magnitudes. In this case, they can improve the performance and the strength of the pipe [4]. An accurate assessment of the residual stresses in the tensile armor wires is essential for an appropriate design as well as for the prediction the magnitude of the stresses during the riser fabrication and operation.

Finite element model can be used to simulate the material deformation process and to predict the residual stresses in the wires. However, these simulations often consider homogeneous material without imperfections; which is a different condition from the real

material composition. Therefore, the result will not accurately represent the residual stress distribution in the material [4]. Additionally to the finite element analysis, it is possible to measure residual stress in these wires by experimental techniques.

Residual stress measurement methods can be divided into two distinct categories. The first one includes the traditional relaxation and diffraction methods, in which the strain field is measure and the stress is calculated by the theory of elasticity. The second category includes magnetics and ultrasonic techniques, where proprieties other than strains are measured. Among all, mechanical relaxation methods are the more used because their proved good results and relative low cost [6, 7, 8].

Relaxation methods are destructives or semi destructives. The strain field or the changes in the strains are consequence of the release of the residual stresses by cutting or material removal. These strains are typically elastic in nature. Therefore, there is a linear relationship between their magnitudes and the released residual stresses [6].

The slitting method is highlighted because is able to measure residual stresses in deeper layer of the material. It is necessary to introduce a planar slit by an incremental cutting and measure the deformation as a function of the slit depth. The method has an analytical portion that should be solved to obtain the stress field in the normal direction to the cut plane prior to slitting [9].

There is not any standard procedure for the slitting methodology, commonly series expansion approach and strain gages measurements are used to estimate the best fit for the residual stresses [8, 9, 10]. However, the use of strain gages in relaxation methods have some practical drawbacks such as high installing time consumption, careful surface preparation and significant error sensitivity to misalignments [11].

Alternatives methods based on light interference overcome the difficulties mentioned above. Among them, digital speckle pattern interferometry (DSPI) provides an accurate non-contact measurement with low time consumption. The technique exploits the rough surface feature and short wavelength of light to allow high sensitivity measurements of local displacements [12, 13, 14]. Digital images of the deformed surface are processed to obtain the optical phase distribution, which is related to the magnitude of the deformation.

According to the previous paragraphs, the measurement of residual stresses in the tensile armor material of a riser is a very important endeavor. The purpose of this research is to develop a methodology by combining DSPI with the slitting method and to evaluate the

feasibility to measure through-thickness residual stress in these tensile armor wires in a near future. For that, beam samples with special stress conditions are used as reference to validate the procedure.

The results will provide the viability of the experimental and numerical approaches here presented, as well as the corrections that should be done to improve the measurements.

1.2 Research Aim and Objectives

The main goal of this work is to evaluate the feasibility of the slitting method combined whit digital speckle pattern interferometry to measure through-thickness residual stresses in steel beam specimens.

In addition, eight key objectives are identified in order to meet the aim:

- Investigate the state of the art of DSPI and the slitting method.
- Prepare the steel beams to be used as specimens.
- Define an appropriate cutting process to introduce a stress relief into the specimen.
- Set the optical layout of the interferometer to measure the surface displacements caused by the slit.
- Perform image processing of the fringe pattern to obtain strain values.
- Compare the strain measurement obtained with traditional electric-resistance gages and DSPI.
- Solve the analytical part of the slitting method in order to obtain residual stresses.
- Compare the residual stress solutions experimentally obtained with the expected values.

1.3 Dissertation Structure

A brief overview for the research was presented in this chapter. Additionally, the need for measuring residual stress in tensile armor wires of flexible risers was highlighted.

Henceforth, the work is organized as follows:

- Chapter 2 presents a review of the literature in reference to flexible risers, residuals stress, and speckle interferometry.
- Chapter 3 describes the workbench developed to measure residual stresses by combining the slitting method and DSPI. It also defines the experimental planning, including specimens, methodology, and strains measurements.
- Chapter 4 reports the experimental results corresponding to the residual stress profiles.
- Chapter 5 contains an overall assessment of the contributions, limitations of the work as well as recommendations for future researches.
- Chapter 6 lists the references cited in this work.

2 LITERATURE REVIEW

This chapter is divided in four sections covering theoretical and technical aspects about risers, residual stress, slitting and DSPI. The first section describes the composite structure of the flexible risers emphasizing the tensile armor. It provides information about the fabrication process and the most common problems associated to tensile wires during service.

The second section describes the physical quantitate of interest, the residual stress, and the mainly residuals stress measurement methods.

In the third and fourth sections the techniques used in this work to measure residual stress are described. Section 2.3 defines the experimental considerations and the analytical model of the slitting method. Finally, section 2.4 explains the speckle phenomenon, and the procedure to measure surface displacements by using digital speckle pattern interferometry.

2.1 Flexible Risers

Flexible pipes are conduits composed by layered materials that allow the deflection without a significant increase in the bending stress. Depending on the application, layers could be bonded forming a homogeneous structure, or non-bonded allowing internal relative movements between them. Typical materials used for the construction include polymers, textile, and steel [15].

Flexible pipes adopted for marine riser in deep water locations are non-bonded type. Offshore industry introduced them in the seventies as an attempt to overcome problems related with sea waves; conductor pipes transferring fluids or power between subsea units and topside floaters should adjust depending on seawater currents flows. Currently, flexible risers are technically acceptable, besides represent the unique solution in the ocean hostile environment [15, 16]. Figure 2.1 shows a flexible riser stored on a reel.

Figure 2.1. Flexible riser stored on reel [17].

Flexible risers accommodate floating platform motion and hydrodynamic loading. It can be installed in a number of different configurations depending on the environmental conditions and the field layout. The optimal arrangement should avoid problems such as interference between vicinity risers, and clashing between the pipe and the seabed. In addition to those factors, the analysis for riser design and installation include adverse weather conditions and natural events (hurricanes, earthquakes, tsunamis, and seabed erosion). Figure 2.2 shows main configurations for flexible riser.

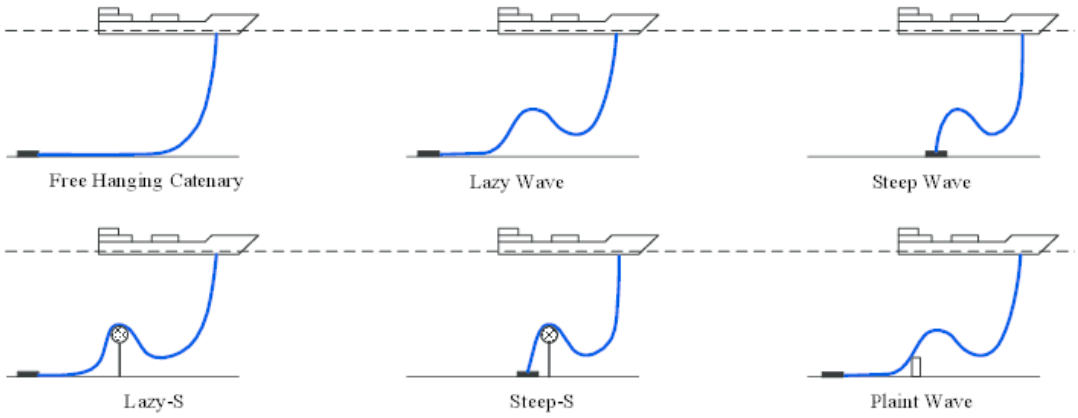

Figure 2.2. Standard flexible riser configurations [16].

The riser must be strong enough to withstand loading. Contrariwise, it should be as light as possible to minimize tensioning. Additionally, it must have enough flexibility to resist fatigue. All those requirements are achieved through the use of a number of layers of different materials in the wall fabrication of the pipe. Consequently, the obtained riser will have a suitable combination between provided strength and low relative bending to axial stiffness.

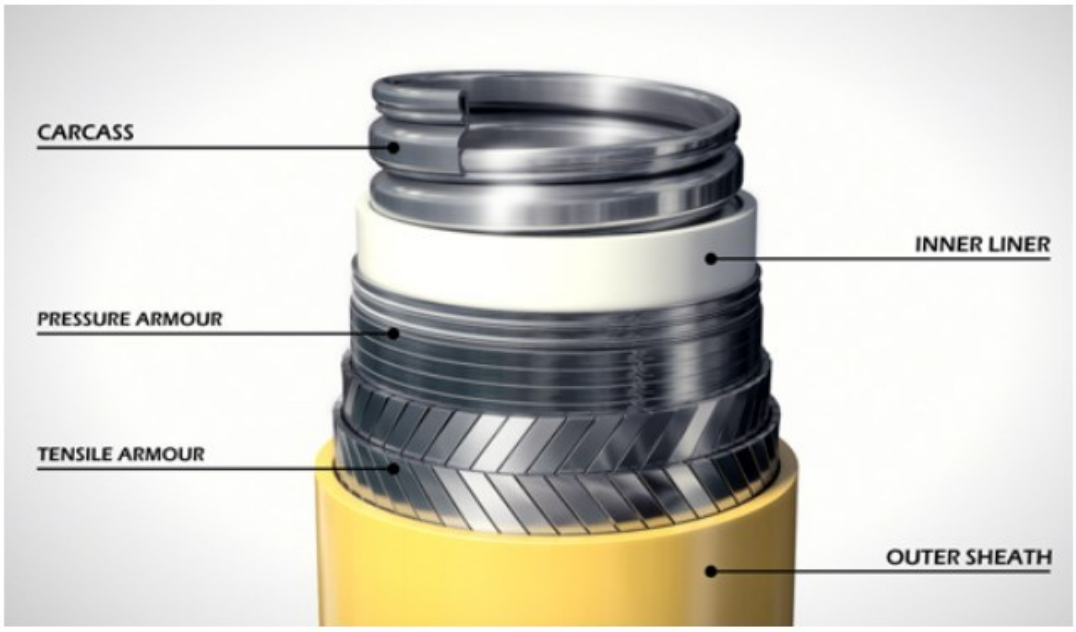

Figure 2.3. Typical flexible riser components [18].

Figure 2.3 shows the typical components of a flexible riser: carcass, inner liner, pressure armor, tensile armor and outer sheath. The following is a brief description of them [16, 18]:

- The carcass is an interlocking structure manufactured from a metallic strip. It prevents the collapse of the inner liner and provides a mechanical protection against tools and abrasive particles.
- The inner liner is an extruded polymer layer providing an internal bore fluid integrity.
- The pressure armor layer is made up of helically wound C-shaped metallic wires. It provides resistance to radial loads caused by the inner bore fluid pressure.
- The tensile armor layers are composed by helically wound flat metallic wires. They always are crossed in pairs in order to provide resistance to axial tension

loads. Because the current work is inspired in the residual stress of these wires, further information about them will be described in next.

- The outer sheath is an external polymer that shields the structural elements of the pipe from the external environment. Additionally, it gives mechanical protection.

2.1.1 Tensile Armor

Usually, flexible risers have two tensile armors responsible for providing axial strength to the pipe. They are constructed by flat rectangular wires helically wound that laid about 30º - 55º to the longitudinal axis of the pipe [16]. These wires are manufactured from carbon steel by hot rolling followed by cold rolling to the final shape [4]. Figure 2.4 shows a section of a formed tensile wire.

Figure 2.4. Section of a formed tensile wire.

After manufacturing, the wire is wounded in coils and transported to the assembly plant. In the factory, the wire is released and deformed by passing through rollers before be re-wounded in the bobbins of the tensile armor machine. This process ensures the integrity of the wire with assured defect tolerance [4]. Figure 2.5 shows the different phases of the fabrication process for the tensile armor.

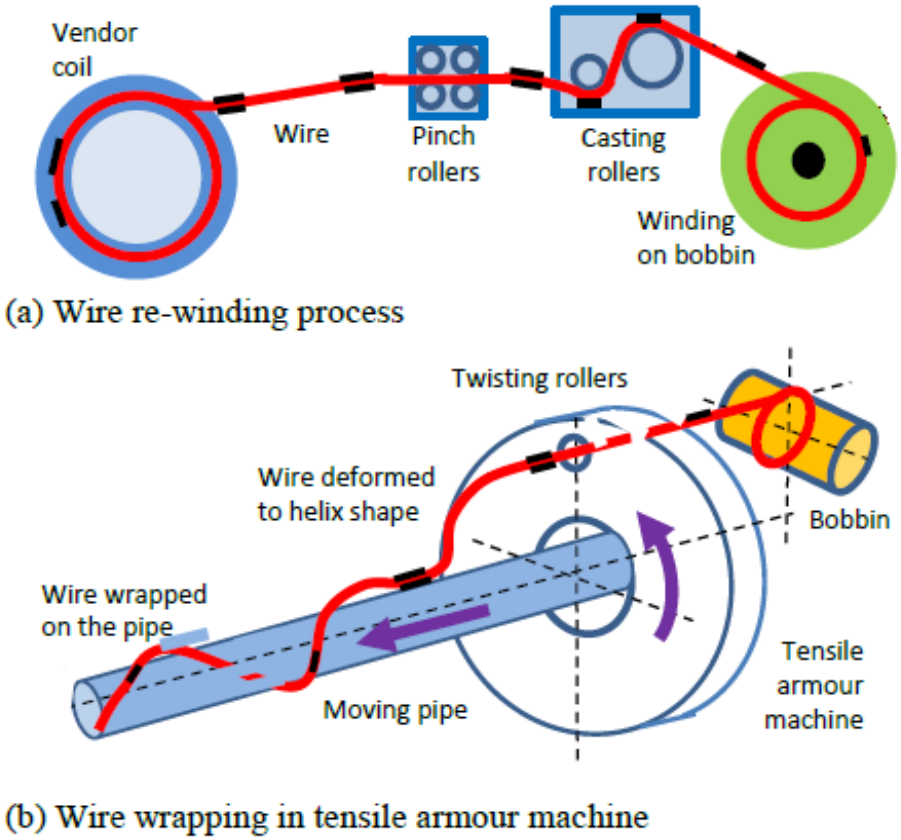

Figure 2.5. Fabrication Process for the tensile armor. a) Wire-rewinding; b) Wire wrapping in the tensile armor machine. (Adapted from [4]).

The wires in the bobbins are uncoiled and pass through the tensile armor machine where are lead onto the pipe body and spirally wound around it. The machine can produce a few meters of pipe before it needs to be stopped for welding the wires [19]. Figure 2.6 shows a tensile armor machine.

Figure 2.6. Tensile armor machine [20].

The manufacturing process must be controlled in order to guarantee the integrity of the pipe for dynamic service. Errors in the manufacture of this armor may induce progressive failures in the riser that can significantly shorten its life and even lead to rupture.

2.1.1.1 Main Failure Modes

During service life, the riser is subjected to a large number of stresses from different sources, such as to the effect of the seawater current flow, loading due to its own weight, the internal pressure of the fluid being transported and the external pressure which is larger as the sea depth increases. These conditions may damage the riser components and can lead the pipe to failure. There are a high number of potential failure modes that can occur in the composite structure of a flexible riser, major of them due to problems in the tensile armor layers [3, 21].

The tensile fatigue in armor wires is the main failure mode when operating in deep waters. The dynamic bending of the riser due to random vessel movements creates a cyclic axial stress in the wires and makes them prone to break as show in Figure 2.7. Although the failure of flexible riser only occurs when there is a significant rupture of the tensile armor wires, the metal fatigue may compromise the overall structure of the pipe [22].

Figure 2.7. Broken tensile armor wires due to tensile fatigue [22].

Another common mode of failure in the tensile armor wires is buckling, shown in Figure 2.8. This is caused by compressive stresses due to the external pressure in deep waters and excessive torsional force. Buckling is an expansion of the tensile armor layer that can lead to instabilities in the radial and lateral directions causing structural damage in the riser [23].

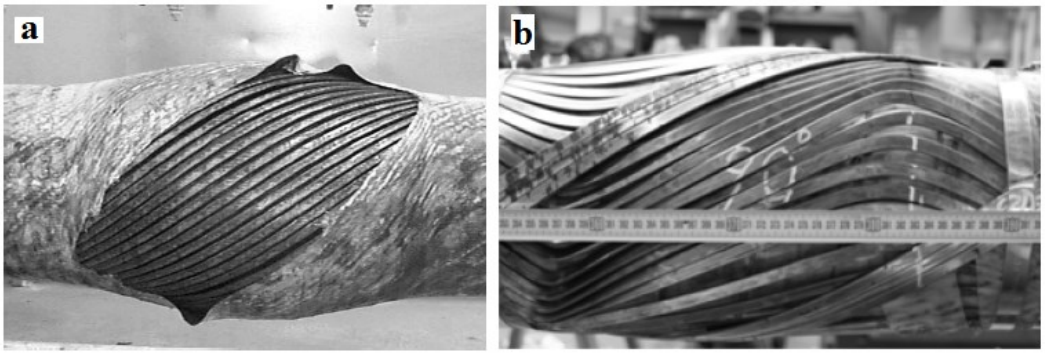

Figure 2.8. a) Radial buckling; b) Lateral buckling in the tensile armor of a flexible riser [24].

The failures in the tensile armor are not only due to the external loads but also due to residual stress. Therefore, the knowledge of residual stresses is crucial to guaranty service conditions without compromising the integrity of the riser. The fundamentals of residual stresses and an overview of the measurement methods will be described in the following section.

2.2 Residual Stress

Residual stress is defined as the stress that remains in mechanical parts even though they are not subjected to outside loadings. In general, any manufacturing process such as machining or rolling involves plastic deformations that lead to residual stresses. The final stress distribution depends on both the material properties and the deformation process the part has undergone [25].

A typical example about how residual stresses are created is shown in Figure 2.9. In a welding process, the very hot weld metal cools over a larger temperature range than the surrounding material and therefore shrinks more (see Figure 2.9.b). Thus, to maintain dimensional continuity through compatible longitudinal strains, large longitudinal tensile residual stresses are created in the weld metal balanced by compressive stresses in the surrounding material (see Figure 2.9.c). This example shows also a fundamental feature of

residual stresses: they are self-equilibrating, that is, tensile stresses are always balanced by compressive stresses and vice versa. Therefore, they are combined to create zero force and moment resultant within the whole volume or structure material [6, 9].

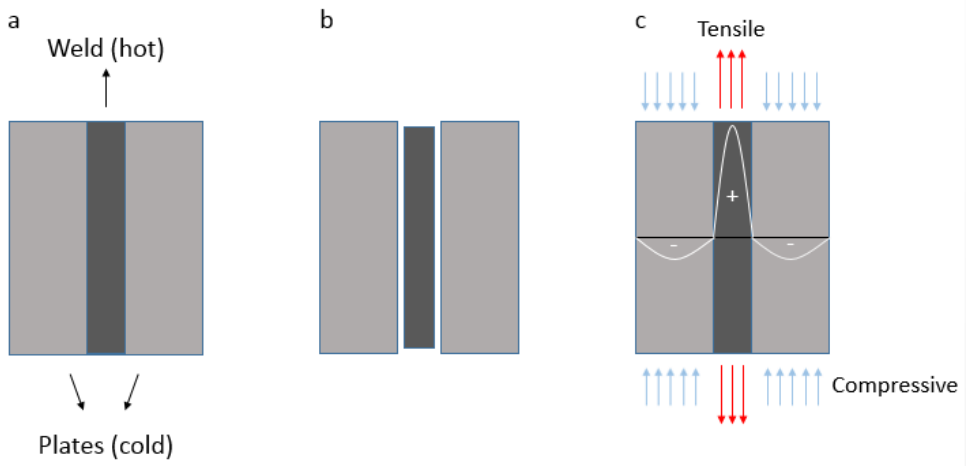

Figure 2.9. a) Welding process; b) Weld metal shrinks more than the surrounding; c) Residual stresses are created to maintain dimensional continuity. (Adapted from [6]).

Because they satisfy the equilibrium condition, residual stresses offer no external evidence of their existence and they could be ignored. Consequently, a failure caused by them would be often more difficult to predict and least to be expected. In terms of material strength, the main effect of the residual stresses is their capability to be added to external loads. When a mechanical part under the effect of a residual stress field characterized by a tensor σ_R, is subjected to a service stress field (σ_S), the real stress in the part will be characterized by the tensor $\sigma_R + \sigma_S$ (Figure 2.10) [25].

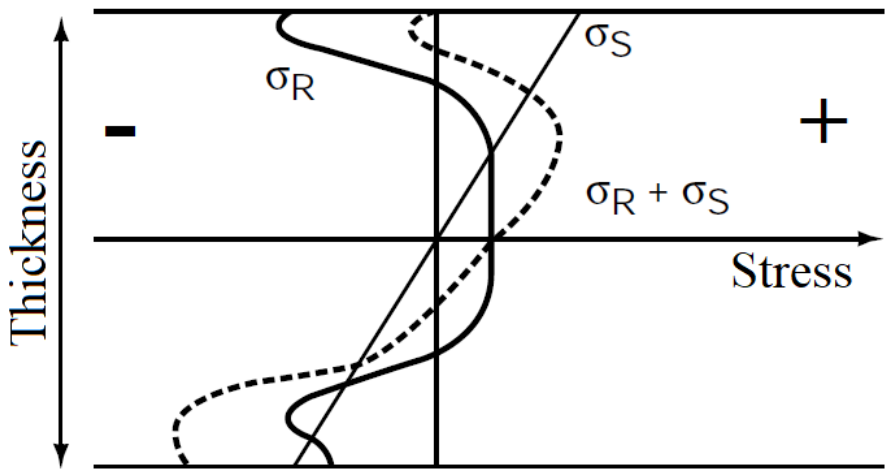

Figure 2.10. Superimposing of residual stress and service stress. (Adapted from [25]).

Depending on the situation, residual stresses can be beneficial or harmful. For example, in mechanical components under tensile load, the presence of tensile residual stress near the surface reduces the material strength. On the other hand, compressive residual stress near the surface enhances fatigue life and increases the local tensile stress supported by the material [6, 9].

2.2.1 Residual Stress in Tensile Armor Wires

During fabrication, the armor wires are subjected to an arduous deformation scheme (as described in section 2.1.1). Twisting and repeated bending in different planes involve plastic deformations that create a significant residual stress field in the wires [4].

Consequently, the lifetime of the riser is dependent on the residual stress level because, as previously mentioned, they are added to stresses caused by external loadings. Residual stresses influence the fatigue behavior, fracture strength and even resistance to corrosion [25]. Therefore, an accurate knowledge of the magnitude of the residual stress field in the tensile armor wire is essential for appropriated design decisions in order to meet material utilization requirements and subsequently predict the integrity and fatigue durability of the pipe.

Fernando *et al.* [4] examined the evolution of residual stresses in tensile armor wires during various stages of the riser manufacturing process. They developed a finite element model to simulate the wire deformation and predict the residual stress distribution. Additionally, three different methods; neutron diffraction, high energy X-ray synchrotron diffraction and contour, were used to measure the residual stress distribution in the wires. The comparison between results showed that the residual stresses measured by the three methods are similar. However, they were different from the predicted values by numerical methods.

The prediction of residual stress distribution in the wire is complex because the real material condition is different from an ideal homogeneous material without imperfections. A great effort must be made to ensure that the plasticity model and boundary conditions imposed in the finite element analysis simulate properly the wire material and deformation process [4]. Considering the factors mentioned above, it is more convenient to evaluate the residual stress in the wires experimentally than by finite element simulations.

2.2.2 Residual Stress Measurement

Stress is an extrinsic physical quantity that must be calculated from other measurable properties. The most common residual stress measurement methods, mechanical relaxation and diffraction, use some type of deformation along with applicable considerations to obtain the internal stress field in materials [7].

The choice of the appropriate measurement method for a given application depends on several factors [6]:

- Nature of the residual stresses: type of gradient along the depth (uniform or non-uniform).
- Specimen damage: is it reasonable to destroy the specimen? What type of damage is acceptable?
- Specimen shape: simple geometry or complex shape?
- Measurement environment: laboratory or field use?
- Accuracy and spatial resolution: detailed or approximate results are needed?
- Cost and duration of the test procedure.

The next subsections give an overview of techniques to calculate residual stress based on relaxation and deformation measurement. The alternative methods such as magnetic and ultrasonic were not described here. Further information about them can be found in [6, 25].

2.2.2.1 Relaxation Measurement Methods

Relaxation methods rely on the stress redistribution (deformations) that occurs when residual stresses are released by cutting or material removal. These deformations are typically elastic in character, and so there is a linear relationship between the deformation size and the released residual stress [6].

After the measurement of the deformations, the originally existing stress profile can be determined using suitable equations. Usually, the mathematical models are based on assumptions made about the stress field including magnitude, gradient, and stress direction [6, 25].

Relaxation methods can be categorized as destructive or semi destructive depending on the relative amount of material removed. Despite they damage or destroy the measured

specimen, these methods are frequently chosen because of their proved good results and relative low cost [6].

The hole-drilling is probably the most widely used relaxation method. It involves drilling a shallow hole in the surface of the specimen and measuring the deformations of the surrounding surface [6]. The method is well developed and standardized; the practical procedure and the methodology to calculate the in-plane residual stresses that originally existed at the hole location are described in the standard ASTM E837 [26]. Traditionally, the experimental setup consists of a portable drilling machine and a three-element strain gage rosette. More recently, full-field optical techniques such as DSPI have been used to measure the surface deformations caused by the hole machining. As example, Figure 2.11 shows a portable device for this purpose [27]. This sensor namely POLAR (Portable Optical Laser-based device for Residual stress measurement) is made up of a base (SB) that supports simultaneously a DSPI measurement module (MM) and a hole-drilling module (DM). The working principle of POLAR is an interchanging process between these two modules. After each increment in the hole depth, a rotary plate positions the DSPI module over the drilled area to acquire digital images of the deformed surface surrounding the hole. At the end of the test, the residual stresses are calculated by a computer program using the surface displacement measured by the DSPI module, following the procedure of the standard ASTM E837.

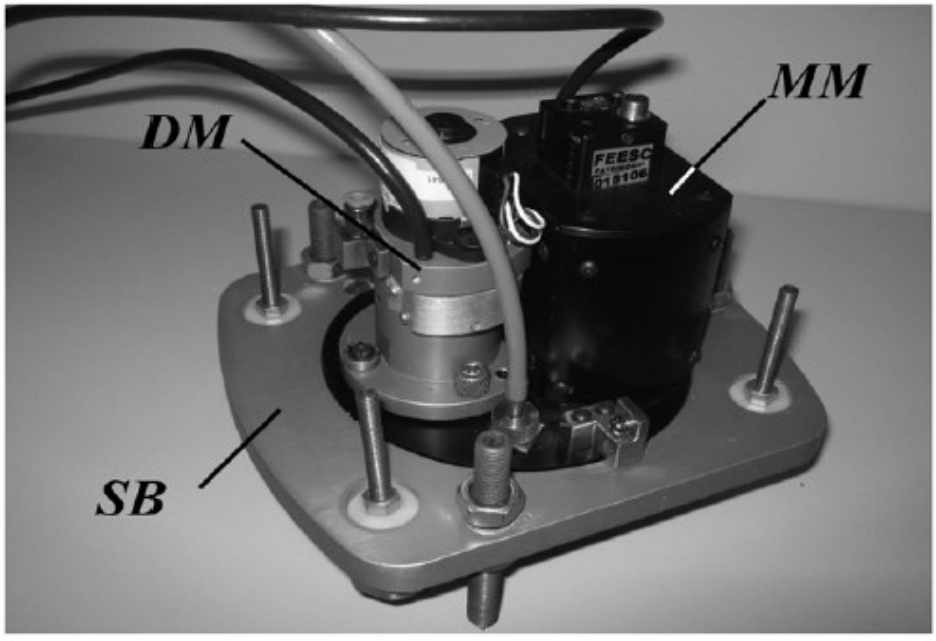

Figure 2.11. Compact sensor to measure residual stress by combining hole-drilling and DSPI. SB (Supporting base), DM (Drilling module), MM (Measurement module) [27].

The hole-drilling method is one of the most popular because it creates only a localized and tolerable damage. Nonetheless is limited to near-surface residual stress measurement, at 1 mm deep [26].

On the other hand, destructive procedures such as slitting or layer removal, are able to measure the residual stress profile in deeper layers of the material. The slitting method is conceptually similar to the hole-drilling, but it uses a planar slit rather than a hole. This method will be described in more detail in section 2.3.

The layer removal method requires the measurement of deformations caused by the removal of a sequence of parallel layers of material from the opposite surface. The method is suited for flat plates and cylindrical specimens where the residual stresses vary with depth but are uniform along the direction parallel to the surface [6, 28].

Recently, a destructive relaxation technique named as the contour method has been used for measuring full-field residual stresses over the entire specimen depth. This newly procedure involves cutting through the specimen cross-section by using a wire electric discharge machine (EDM), and measuring the surface height profiles of the both cut surfaces. The originally existing residual stresses normal to the cut are evaluated from finite element calculations by determining the stresses required to return the deformed surface shape to a flat plane. This technique is remarkable because it gives a two dimensional map of the residual stress distribution over the whole material cross-section. However, accurate results require a high precision metrology equipment to measure the surface height fields, besides that electric discharge machines are often difficult to access [6, 29].

2.2.2.2 Diffraction Methods

Diffraction methods allow residual stresses to be measured in situ, without affect or reduce the mechanical strength of the component being analyzed. They exploit the ability of the electromagnetic radiation to reveal information about the crystal structure of materials, which is used as an internal strain gage [6].

The measurement depth depends on the type of radiation used: X-ray, synchrotron X-ray or Neutron. The conventional X-ray diffraction (XRD) method has low penetration being limited to surface measurements (in the order of 0.025 mm). The XRD is based on the fundamental relation formulated by Bragg in 1913 [30], connecting the spacing between certain lattice planes to the diffraction angle at which the radiation is scattered coherently. The

residual stress values are then calculated from the scattering data assuming a linear elastic distortion of the crystal lattice [6]. Figure 2.12 shows a commercial portable X-ray diffractometer [25].

Figure 2.12. Miniature X-ray diffractomer [25].

In the synchrotron X-ray diffraction the sample is illuminated by a high energy beam, a million times more intense than laboratory base X-rays, penetrating depths on the order of mm in the steel [4, 6].

Neutron diffraction (ND) is capable of measuring residual stresses through a depth of several tens of mm, sometimes hundreds. The basic concept underlying the measurement is the same of the previous two diffraction methods, however, neutrons interact directly with the nucleus of the atom, and the contribution to the diffracted intensity is different from X-rays which interact with electrons [6].

2.3 The Slitting Method

Also known as crack compliance method [31], it is a mechanical relaxation technique able to determine the residual stress variation with depth by incrementally introducing a narrow slit into the material. Like the hole-drilling, strain measurements at each increment of depth are needed.

The method, originally developed by Vaidyanathan and Finnie in 1971 [32], has been used in a variety of materials and geometries such as beams, plates, disks, and cylinders, to both near-surface and through-thickness residual stress measurements [6, 8, 9]. Slitting has become one of the most highlighted relaxation methods because is relatively simple to perform, can be done quickly, and provides useful results with a high degree of repeatability [33].

2.3.1 Fundamentals

The basic assumptions of the method are that the stress does not vary in the transverse direction, and the deformation due to cutting is linear elastic (like all the relaxation techniques) [9]. The residual stress calculation relies on the specific geometry of the part being analyzed. In this work, the implementation of the slitting method in a flat block similar to the tensile armor wire geometry is described. Figure 2.13 defines a rectangular coordinate system and some common terms for the slitting method.

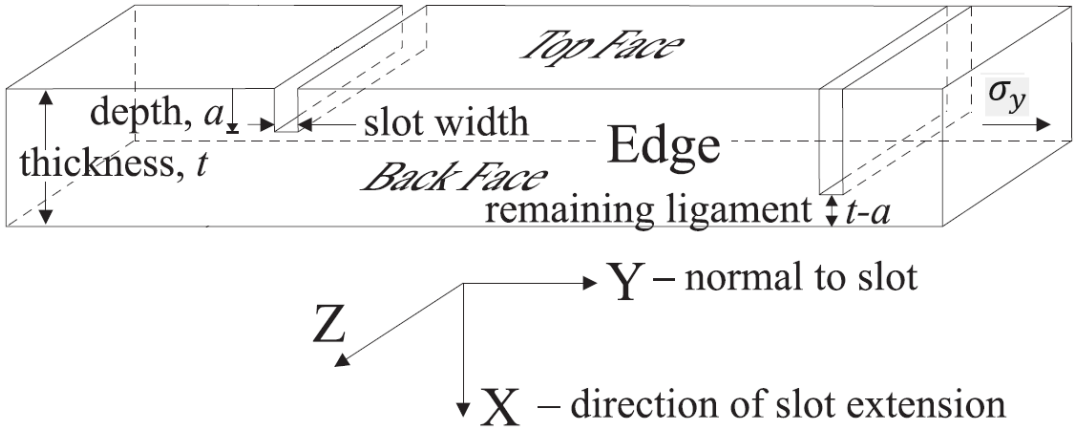

Figure 2.13. Coordinate system and terminology for slitting method. (Adapted from [8]).

According to Figure 2.13, a slit is introduced from the top face of the material and is extended in the *x*-direction towards the back face. The two surfaces normal to the *z*-direction are the edges. The *y*-direction is normal to the slit. The normal stress component measured is σ_y. Stress variation with depth means the stress distribution along the *x*-direction. The slit depth is labeled with *a.* The thickness of the material, *t*, is the dimension in the *x*-direction at the plane of the cut. The remaining ligament is the intact portion of the part in the slit plane given by $a < x < t$ [8].

It does not exist a standard procedure for using the slitting methodology, so there are several analytical and experimental choices to apply it [8, 9]. For the experiment is need to decide how to introduce the slit and how to measure the related strains, subsection 2.3.5 is intended to these issues. After finishing the test, properly data analysis is critical to achieve a good outcome.

The analytical portion of the slitting method can be divided in two components: a forward and an inverse problem. The forward problem gives the strains that would be measured when a slit is introduced into a material with an arbitrary known residual stress distribution. The inverse problem then uses the forward solution to calculate the residual stress distribution that best matches the experimentally measured strains [8, 9]. Different approaches can be used to solve the forward and inverse problem, the following subsections, 2.3.2, 2.3.3 and 2.3.4, are meant to describe the formulation and computation that will be implemented to calculate the residual stress profile in the specimens.

2.3.2 Series Expansion for Approximate Residual Stress

The series expansion approach assumes that the unknown residual stress variation as function of depth $\sigma_y(x)$, may be represented as the sum of convenient n basis functions $P_j(x)$, multiplied by unknown amplitude coefficients A_j [9],

$$\sigma_y(x) = \sum_{j=0}^{n} P_j(x) A_j \qquad (2.1)$$

The variable x in Equation 2.1 defines the distance of the slit from the top face and is expressed over the domain [0, 1], which corresponds to the slit depth normalized by the thickness of the block, i.e., $x = a/t$.

Assuming linear elastic behavior, the strain that would occur as a function of slit depth for the residual stress given by Equation 2.1 can be written as:

$$\varepsilon_y(x) = \frac{1}{E'} \sum_{j=0}^{n} C_j(x) A_j \qquad (2.2)$$

Where $C_j(x)$ are known as compliance functions, i.e., the strains that would be measured at the top or back face due to slitting if the pre-slit residual stress is given by each term of the series 2.1 with an unitary amplitude, i.e., $A_j = 1$. $E' = E$ for plane stress state and

$E' = E/(1-\nu^2)$ for plane strain state [6, 8, 9]. This compliance functions can be computed by solving an elastic boundary value problem using finite element analysis or another forward solution [9].

The resulting strains of Equation 2.2 at each of the m increments of the slit depth, $\varepsilon_1, \ldots, \varepsilon_i, \ldots \varepsilon_m$ are

$$\begin{aligned} \varepsilon_1 &= \frac{1}{E'}\sum_{j=0}^{n} C_{1j}A_j \\ &\vdots \\ \varepsilon_i &= \frac{1}{E'}\sum_{j=0}^{n} C_{ij}A_j \\ &\vdots \\ \varepsilon_m &= \frac{1}{E'}\sum_{j=0}^{n} C_{mj}A_j \end{aligned} \qquad (2.3)$$

Adopting matrix notation:

$$\{\varepsilon\} = \frac{1}{E'}[C]\{A\} \qquad (2.4)$$

Where braces, $\{\}$, denote a vector, and square brackets, [ ], denote a matrix. Equation 2.4 defines a linear system in which the compliance matrix, $[C]$, relates the $(n+1)\times 1$ vector $\{A\}$ of unknown basic functions amplitudes to $m \times 1$ vector $\{\varepsilon\}$ of expected strains. Once the compliance matrix is computed, the Equation 2.4 is inverted to calculate the vector of amplitudes $\{A\}$ from measured strains, and thus determine the residual stress profile using the chosen basis functions [9].

2.3.3 Forward Problem: Finite Element Approach

The compliance matrix is an $m \times (n+1)$ array with rows representing the set of incremental slit depths, and columns representing the set of basis functions [9],

$$[C] = \begin{bmatrix} C_{10} & \cdots & C_{1j} & \cdots & C_{1n} \\ \vdots & \ddots & & \ddots & \\ C_{i0} & & C_{ij} & & C_{in} \\ \vdots & \ddots & & \ddots & \\ C_{m0} & & C_{mj} & & C_{mn} \end{bmatrix}$$

The C_{ij} element is the strain occurring for a slit of depth a_i when the released residual stress is exactly equal to the j^{th} order basis function P_j [9].

The calculation of these strains is a forward problem commonly solved using finite element analysis [6, 8]. The formulation of an accurate compliance matrix requires that the model developed represents properly the experimental setup, including specimen size, cut depth, slit dimension, and strain measurement location. For a flat block such as the Figure 2.13, most of the published works used a two-dimensional mesh (assuming plane stress state) with symmetry condition about the slit plane [34, 35, 36, 37, 38].

The forward solution is based on the Bueckner's superposition principle [39]. This says that the released strain can be estimated by considering the cracked body and loading the crack faces with the residual stresses that originally existed on this plane in the uncracked body.

In practical terms, the residual stress relief due to slitting is simulated by removing the elements adjacent to the symmetry plane that correspond to a given cut depth, and then loading the exposed face of the slit with a normal pressure distribution. The compliances for a particular location are calculated by computing the relative displacement normal to the slit between a pair of nodes in the mesh, and dividing it by the initial length between them [9].

A relevant issue in the forward problem is the selection of the basis functions to obtain the compliances; they must be linearly independent and their combination must be able to represent the solution adequately. Possible choices include unit pulses, power series, and Legendre polynomials [9]. In this work, Legendre polynomials were chosen as basis function so they will be described in the next section. There is also a brief description for the case using unit pulse functions.

2.3.3.1 Legendre Polynomials to Compute the Compliance Functions

The Legendre polynomials basis $L_j(x)$ is convenient for describing through-thickness residual stress because all terms with $j \geq 2$ satisfy the equilibrium conditions of zero resultant force and moment [9]. Figure 2.14 shows $L_j(x)$ functions for $j = 2, 6, 8$ and 12, defined over the normalized domain [0, 1].

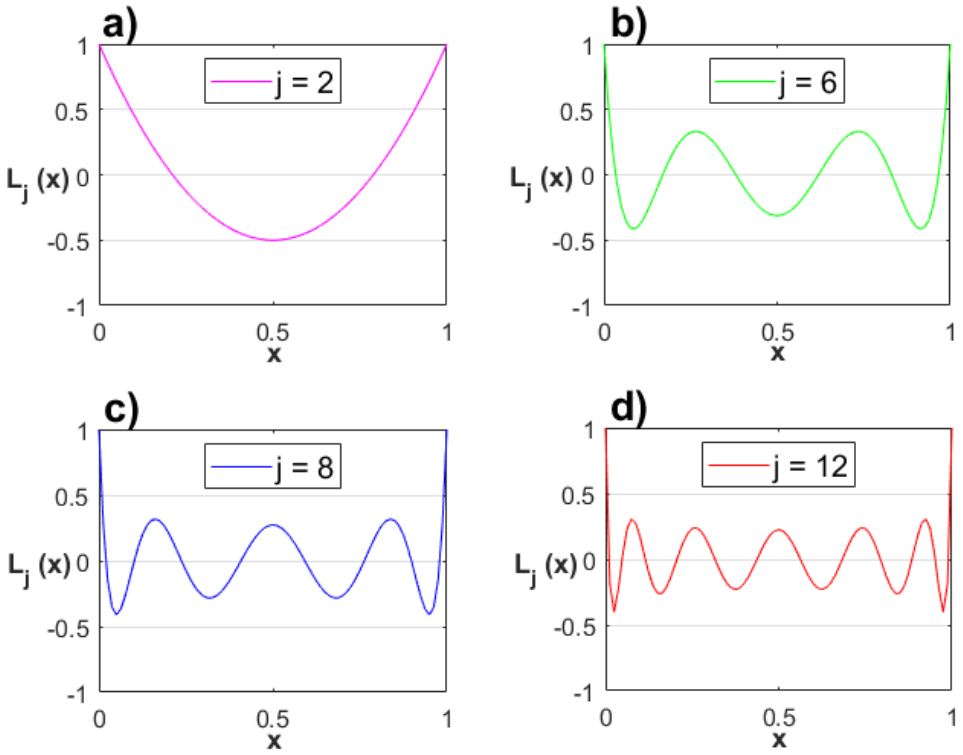

Figure 2.14. Legendre polynomials of various orders: a) $j = 2$; b) $j = 6$; c) $j = 8$; and d) $j = 12$.

In this case, the residual stress is then approximated by the truncated Legendre polynomial,

$$\sigma_y(x) = \sum_{j=2}^{n} L_j(x) A_j \qquad (2.5)$$

The accuracy of the solution given by Equation 2.5 is dependent on the order of Legendre polynomials n. It is generally hoped that as the order of the expansion increases, the result will converge to a solution. But after some points, the fit will diverge [8]. This is because the compliance matrix becomes ill-conditioned when inverted, leading to instabilities in the numerical computation of the residual stress as n increases. The properly selected order is determined during data reduction as detailed in [35, 37]. This methodology must provide the good fit to strain while not magnifying errors too greatly.

This work makes use of the closed form expression provided by Lee and Hill in [40], which allows to compute analytically the compliances at any depth of cut when the slit is introduced in the centerline of a rectangular block having a strain gage mounted on the surface opposite the cut, oriented to measure deformations in the axial direction (see Figure 2.15).

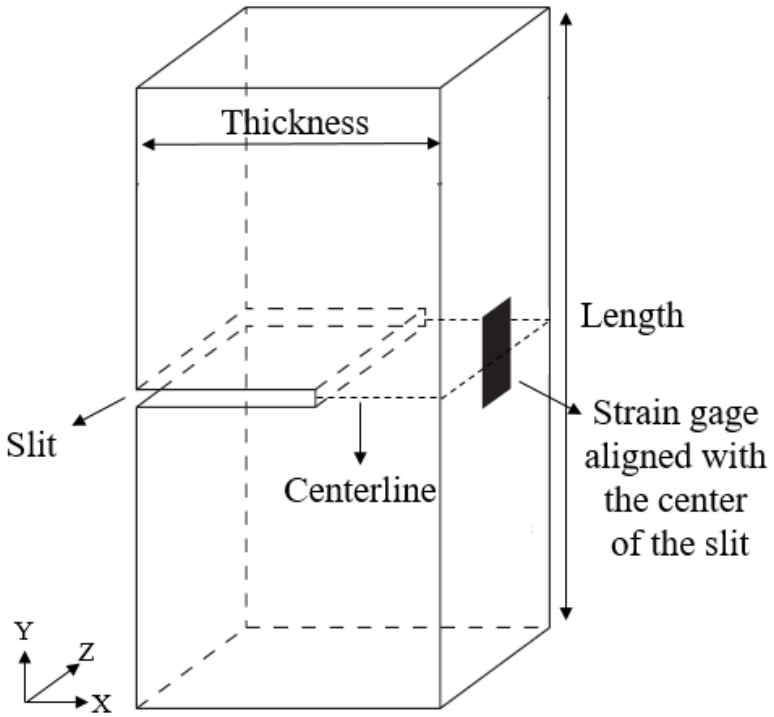

Figure 2.15. Slitting model used in [40]. (Adapted from [6]).

In their work, Lee and Hill used 12^{th} order truncated Legendre polynomials as basis functions. Figure 2.16 shows the compliances $C_j(x)$, resulting from the release of $\sigma_y(x) = L_2(x),\ L_6(x),\ L_8(x),$ and $L_{12}(x)$.

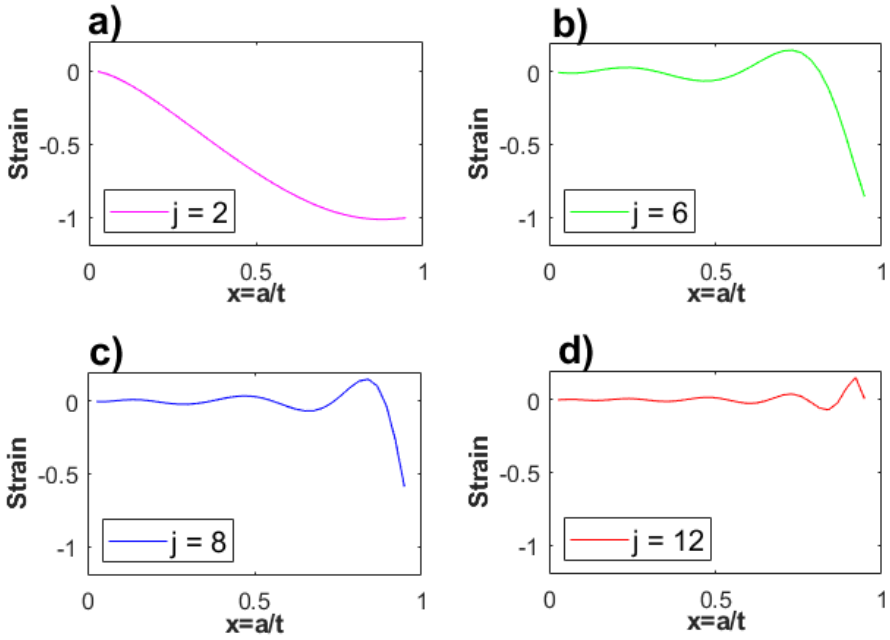

Figure 2.16. Compliances functions when a zero width slit is introduced in a flat block with $E = 1$ and $\nu = 0.3$ for various input stress: a) $L_2(x)$, b) $L_6(x)$, c) $L_8(x)$, and d) $L_{12}(x)$ [40].

2.3.3.2 Unite Pulse Functions to Compute the Compliances

In this case the unknown residual stress is approximated by using unite pulse functions $u_j(x)$,

$$\sigma_y(x) = \sum_{j=1}^{n} u_j(x) A_j \qquad (2.6)$$

A series of four $u_j(x)$ functions is illustrated in Figure 2.17. The width of each pulse corresponds to the successive increments in material removal depth [38].

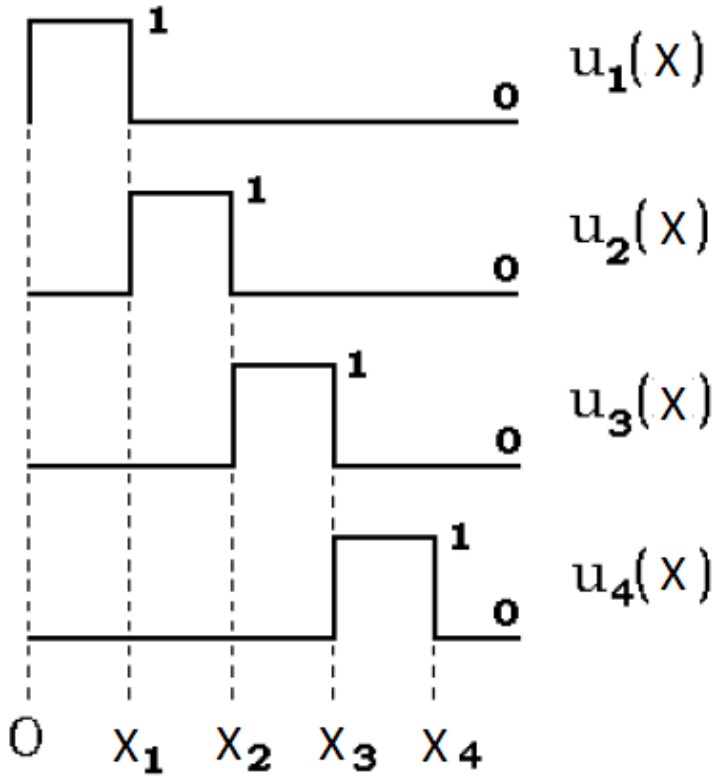

Figure 2.17. Unite pulse functions used for residual stress calculation. (Adapted from [38]).

Here the number of basis functions to be used (n) is equal to the m increments of the slit depth, thus obtaining a square compliance matrix. Figure 2.18 shows the physical meaning of the obtained compliances.

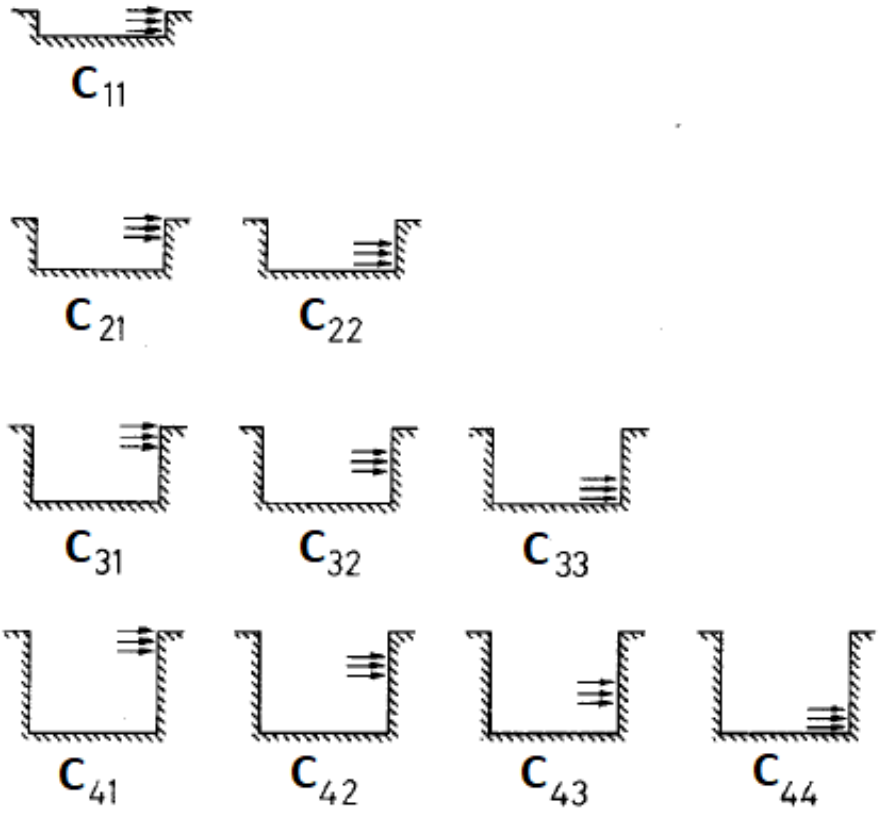

Figure 2.18. Physical interpretation of the compliances for the unite pulse functions. (Adapted from [38]).

Figure 2.18 also shows an important feature of this approach; the compliance matrix for the unite pulse solution is lower triangular. In this case the Equation 2.4 is expressed as:

$$\begin{bmatrix} C_{11} & 0 & 0 & 0 & 0 & \cdots & 0 \\ C_{21} & C_{22} & 0 & 0 & 0 & \cdots & 0 \\ C_{31} & C_{32} & C_{33} & 0 & 0 & \cdots & 0 \\ C_{41} & C_{42} & C_{43} & C_{44} & 0 & \cdots & 0 \\ C_{51} & C_{52} & C_{53} & C_{54} & C_{55} & \cdots & 0 \\ \vdots & \vdots & \vdots & \vdots & \vdots & \ddots & 0 \\ C_{m1} & C_{m2} & C_{m3} & C_{m4} & C_{m5} & \cdots & C_{mn} \end{bmatrix} \begin{Bmatrix} \sigma_1 \\ \sigma_2 \\ \sigma_3 \\ \sigma_4 \\ \sigma_5 \\ \vdots \\ \sigma_n \end{Bmatrix} = \begin{Bmatrix} \varepsilon_{meas1} \\ \varepsilon_{meas2} \\ \varepsilon_{meas3} \\ \varepsilon_{meas4} \\ \varepsilon_{meas5} \\ \vdots \\ \varepsilon_{meas} \end{Bmatrix}$$

When using unite pulses, enforce equilibrium becomes a need because the functions do not automatically satisfy this condition. Therefore, additional constraints should be imposed in the analytical procedure.

2.3.4 Inverse Problem: Least Square Fit for Stress Estimation

The inverse problem aims to find the best-fit solution for the unknown residual stress profile. This is done using a least square fit between the measured strains ε_{meas}, and those estimated by Equation 2.2. The difference between them at the i^{th} step is given by:

$$\Delta\varepsilon(a_i) = \varepsilon(a_i) - \varepsilon_{meas}(a_i) = \frac{1}{E'}\sum_{j=0}^{n} C_j(a_i)A_j - \varepsilon_{meas}(a_i) \qquad (2.7)$$

And over all depths of cut:

$$\sum_{i=1}^{m} \Delta\varepsilon(a_i) = \sum_{i=1}^{m}\left[\frac{1}{E'}\sum_{j=0}^{n} C_j(a_i)A_j - \varepsilon_{meas}(a_i)\right] \qquad (2.8)$$

Squaring the difference to avoid negative values:

$$\sum_{i=1}^{m} \Delta\varepsilon^2(a_i) = \sum_{i=1}^{m}\left[\frac{1}{E'}\sum_{j=0}^{n} C_j(a_i)A_j - \varepsilon_{meas}(a_i)\right]^2 \qquad (2.9)$$

The minimum of the total error is achieved when the partial derivatives with respect to A_j for $j = 0$ to n are equal to zero, that is:

$$\frac{\partial}{\partial A_j}\sum_{i=1}^{m} \Delta\varepsilon^2(a_i) = 0 \qquad (2.10)$$

After solving the derivatives and arranging in matrix notation:

$$\frac{1}{E'}[C]^T([C]\{A\} - \{\varepsilon_{meas}\}) = 0 \qquad (2.11)$$

Where $[C]^T$ is the transpose of the compliance matrix. Isolating the vector $\{A\}$, the Equation 2.11 becomes

$$\frac{1}{E'}\{A\} = ([C]^T[C])^{-1}([C]^T\{\varepsilon_{meas}\}) \qquad (2.12)$$

After finding the basis amplitudes, the residual stress can be calculated using Equation 2.1.

2.3.5 Practical Considerations for Through-Thickness Measurement

As any experimental method, attention to detail in executing a slitting experiment is crucial to obtain satisfactory results. Before starting a test, is necessary to decide the method to cut the sample and the way to measure the released strains. The following subsections review the practical choices available to carry out slitting, their advantages and disadvantages.

2.3.5.1 Cutting Method

Machining the slit is a critical step in the crack compliance method. Several different techniques have been used including saws [32], milling cutters [41, 42], and electric discharge machines (EDM) [33, 35, 36, 38, 43]. The properly choice must take into account the effects on the measurement. Additionally, it depends among other things, on the strain measurement system [8].

Mechanical machining using a saw or milling cutter is universally available but may introduce temperature increase and plastic deformations near the slit. However, strain measurements in the back face are relatively insensitive to this unwanted effects and, thus, only small error in measured residual stress will be inserted [44, 45].

In EDM, a wire is electrically charged in relation to the workpiece and as both approach, a spark jumps the gap and locally melts to remove material. The cutting occurs in a dielectric fluid, usually deionized water, and the wire never actually contacts the workpiece. EDM cutting offers good dimensional control and it performs a much finer slit. Additionally, it does not rely on mechanical force reflecting in the introduction of not significant stresses [8]. However, EDM machines are expensive, and the presence of the fluid used is a drawback for the optical measurement of strains.

2.3.5.2 Strain Measurement

For through-thickness residual stress measurements, strain must be taken at each increment of depth on the back surface [10]. Electric-resistance strain gages are by far the most commonly devices used to this purpose [8]. Although they offer high sensitivity and reliability, their use has some practical drawbacks and limitations [11]:

- Measurement is limited to a few discrete locations;
- High installing time consumption;
- Careful surface preparation;

- Significant error sensitivity to misalignments.

Another possibility is to measure the full field surface deformation using optical systems based on laser interference [42]. The next section will describe one of these techniques, digital speckle pattern interferometry, since it was used to measure the released strains in this work.

2.4 Digital Speckle Pattern Interferometry

Digital speckle pattern interferometry (DSPI) is a non-contacting technique that allows to measure features of surfaces under investigation such displacements, deformations, stresses and vibrations, on laboratory as well as in industrial applications [46]. It is based on the speckle effect; a high-contrast and fine-scale granular pattern produced when a diffuse object is illuminated with a coherent light source.

Figure 2.19.a shows how the speckle is created. A laser beam incident on a rough surface with height variations greater than the wavelength of the light (λ) is scattered in all directions. As a consequence, scattered waves interfere with random individual phases and form an interference pattern consisting of dark spots (destructive interference) and bright spots (constructive interference) randomly distributed in the space. A typical speckle pattern is shown in Figure 2.19.b.

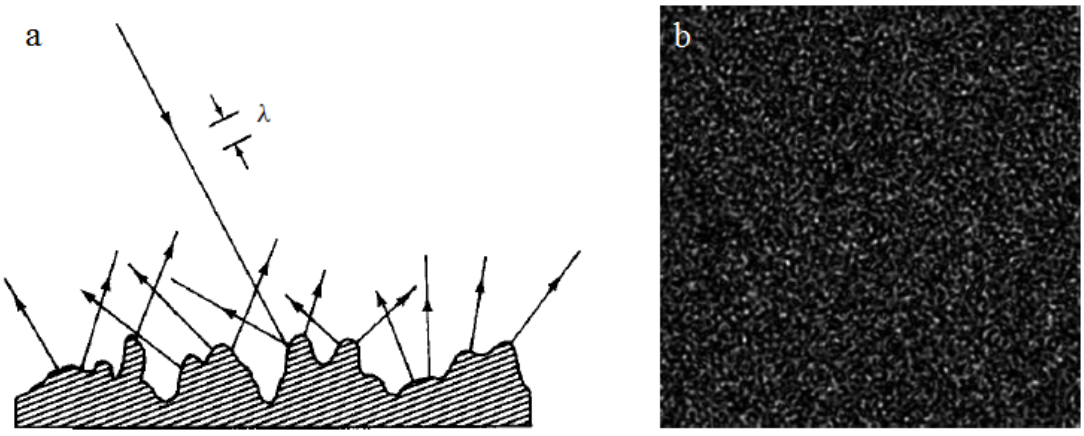

Figure 2.19. a) Light scattered from a rough surface [13]; b) Typical simulated speckle distribution [47].

DSPI acquires digital images of the speckle pattern created by the interference of two beams from the same laser source. Each pixel of these images known as specklegrams has a relative phase and therefore an intensity distribution that can be written as [48]:

$$I = I_1 + I_2 + 2\sqrt{I_1 I_2}\, cos(\varphi_1 - \varphi_2) \qquad (2.13)$$

Where I_1, I_2 are the intensities and φ_1, φ_2 are the phases of the interfering wavefronts. Equation 2.13 can be expressed as:

$$I = I_0(1 + V\, cos\phi) \qquad (2.14)$$

Where $I_0 = I_1 + I_2$ is called background intensity, $V = \frac{2\sqrt{I_1 I_2}}{I_1 + I_2}$ represents the contrast, and $\phi = \varphi_1 - \varphi_2$ is the relative phase between the interfering beams.

The random distribution of the intensity for a specklegram can be modified by displacements of the rough surface, changes in the illumination and observation geometry, and changes in the wavelength of the laser as well as in the refractive medium through which the light travels [49]. Therefore, for a fixed observation geometry, laser light wavelength, and refractive index, only the displacements of the observed surface will modify the intensity of the speckle pattern. This feature is used to determine the surface deformation caused by any perturbation.

The digital subtraction of two specklegrams from different states, one before (as reference) and other after deformation, creates a fringe pattern (depicted in Figure 2.20) that contains information about the relative displacement of the illuminated area. To represent the correlation pattern in Figure 2.20, an expression analog to Equation 2.14 can be written as:

$$I_{12} = I_{0f}(1 + V_f\, cos\Delta\phi) \qquad (2.15)$$

Where I_{of} is the average intensity, V_f represents the contrast of the fringes, and $\Delta\phi = \phi_1 - \phi_2$ is the phase variation between the two specklegrams. These fringes can be interpreted as links between points with equal displacements along the sensitivity direction, which is the displacement direction of the surface that produces the maximum variation of phase. The points where $\Delta\phi = 2n\pi$ $(n = 0, 1, 2, \ldots)$ have identical speckle distributions, and the intensity I_{12} is null, producing dark fringes. Conversely, the points where $\Delta\phi = (2n + 1)\pi$ have bright fringes [47].

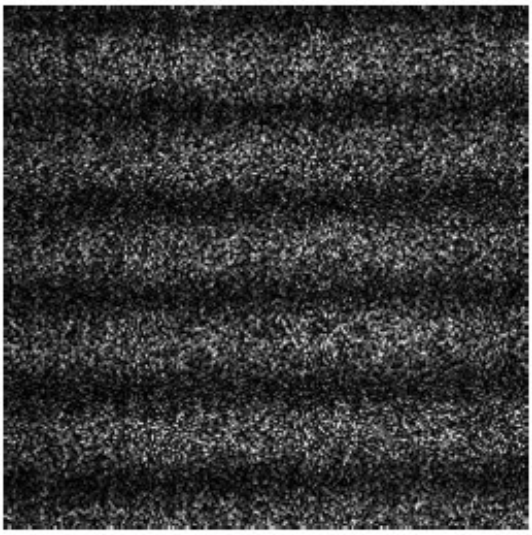

Figure 2.20. Correlation fringes [47].

The direct visualization of the correlation fringes allows the qualitative analysis of the displacement field for the illuminated surface. In order to obtain quantitative values of these displacements is necessary to determine the value of $\Delta\phi$, which is related with the optical path length traveled by the laser light from the source to the CCD of the camera, after and before deformation. The phase difference ($\Delta\phi$) corresponding to an optical path difference (OPD) caused by the displacement of the object surface can be written as [47]:

$$\Delta\phi = \frac{2\pi}{\lambda}(OPD) \qquad (2.16)$$

Where λ is the wavelength of the laser. The OPD can be expressed as [47]:

$$OPD = k \cdot d \qquad (2.17)$$

Where k is the sensitivity vector, and d is the displacement of the surface. By substituting Equation 2.17 into 2.16, it is derived an expression that relates the phase difference in each pixel of the image (resulting from subtract the two specklegrams) to the displacements of the surface:

$$\Delta\phi = \frac{2\pi}{\lambda}(k \cdot d) \qquad (2.18)$$

As can be seen from Equation 2.18, it is necessary to know the sensitivity vector of the interferometer in order to obtain the deformation magnitudes. For the measurement of deformations caused by slitting, is necessary in-plane sensitivity.

2.4.1 In-plane Sensitivity

The optical configuration for measuring in-plane displacements is based on a two-beam arrangement [50]. As shown in Figure 2.21, two beams from the same source with a wavelength λ, illuminate the surface forming the same angle (γ) in relation to its normal vector. Thus, two speckle distributions coming from the object surface, with their respective sensitivity vectors k_1 and k_2 , interfere in the image plane of a camera.

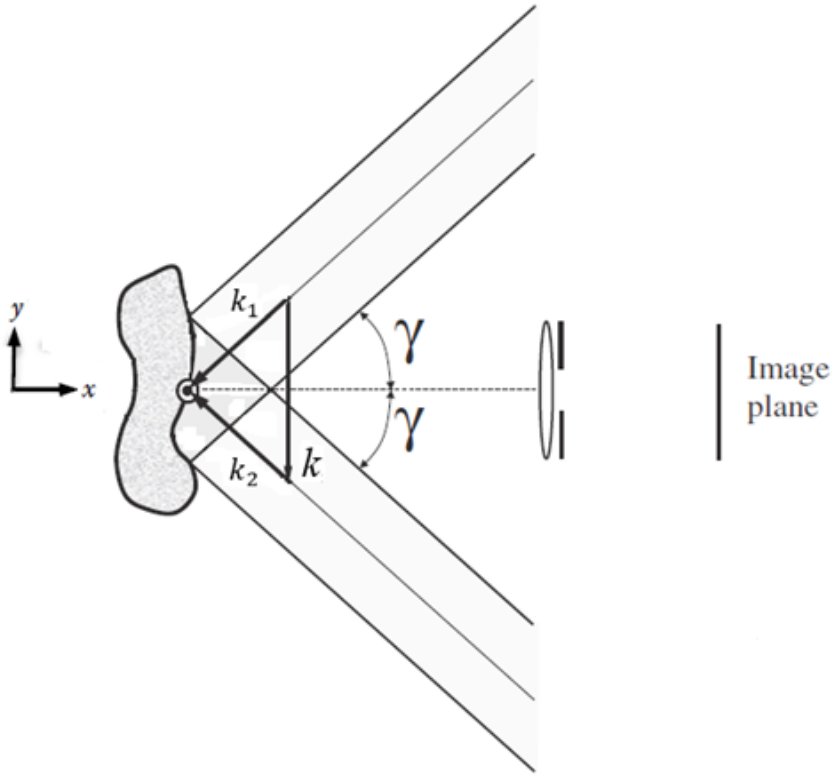

Figure 2.21. Two-beam arrangement for in-plane sensitivity. (Adapted from [47]).

The illumination vectors k_1 and k_2 can be written as:

$$k_1 = -(sin\gamma)\hat{n}_y - (cos\gamma)\hat{n}_x$$
$$k_2 = (sin\gamma)\hat{n}_y - (cos\gamma)\hat{n}_x \qquad (2.19)$$

Where $\hat{n}_x$ and $\hat{n}_y$ are the unitary vectors in the x and y direction respectively. The measurement sensitivity is given by the sensitivity vector k, which is obtained by subtracting both illumination vectors:

$$k = k_2 - k_1 = (2sin\gamma)\hat{n}_y \qquad (2.20)$$

Substituting Equation 2.20 into Equation 2.18:

$$\Delta\phi = \frac{2\pi(2sin\gamma)d}{\lambda} \qquad (2.21)$$

And isolating for the displacement:

$$d = \frac{\lambda}{4\pi(sin\gamma)}\Delta\phi \qquad (2.22)$$

The in-plane displacement of each point of the surface in the x-direction computed by Equation 2.22 can be converted in strain magnitudes, which are used to solve the inverse problem of the slitting method.

The challenge now is to determine the phase change ($\Delta\phi$) in each pixel due to the surface deformation. This is done in two steps as shown in Figure 2.22. The first step is called the acquisition step, where specklegrams and their respectively phase maps (optical phase in each pixel) ϕ_1 and ϕ_2, are acquired before and after the introduction of a perturbation. The next step is named the processing step, which enables to obtain the value of the phase difference and convert it in quantitative physical parameters [47].

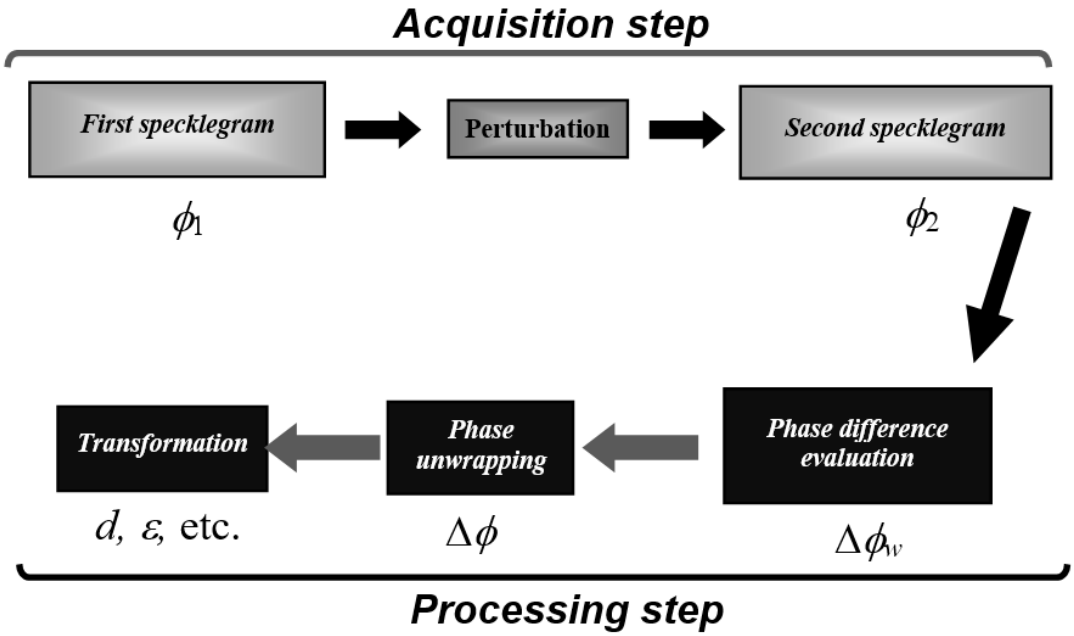

Figure 2.22. Steps to analyze DSPI specklegram. (Adapted from [47]).

2.4.2 Acquisition Step: Phase-Shifting

As previously described, each specklegram has a phase distribution that must be evaluated in order to compute the difference between the two states. There are many techniques to measure these phase maps**,** which can be classified in two main categories: (a) the phase data is acquired sequentially, and (b) the phase data is taken simultaneously. The former methods are called as temporal phase-shifting techniques and the latter are named as spatial phase-shifting methodologies [13].

The temporal methods are the most prevalent to quantify the optical phase distribution [47]. They involve the acquisition of a certain number of specklegrams, each one with a relative phase shift that is introduced by slightly changing the optical path traveled by one of the illumination beams that interferes in the image plane of the camera. Possibilities for phase shifting include the use of piezoelectric translators (PZT), diffraction plates and glass plates [47].

Equation 2.14 describes the specklegram intensity. It can be seen that it contains three unknowns ($I_0,\ V,\ \phi$), requiring a minimum of three measurements to determine the phase. The five-frame algorithm [51] use five images shifted by $\pi/2$ resulting in the following intensities for the reference condition:

$$\begin{aligned} I1 &= I_0\{1 + V\ cos\phi_1\} \\ I2 &= I_0\{1 + V\ cos(\phi_1 + \pi/2)\} = I_0\{1 - V\ sin\phi_1\} \\ I3 &= I_0\{1 + V\ cos(\phi_1 + \pi)\} = I_0\{1 - V\ cos\phi_1\} \\ I4 &= I_0\{1 + V\ cos(\phi_1 + 3\pi/2)\} = I_0\{1 + V\ sin\phi_1\} \\ I5 &= I_0\{1 + V\ cos(\phi_1 + 2\pi)\} = I_0\{1 + V\ cos\phi_1\} \end{aligned} \qquad (2.23)$$

Rearranging this set of equations, the value of ϕ_1 in each pixel can be obtained:

$$\phi_1 = tan^{-1}\left\{\frac{2(I4 - I2)}{I5 + I1 - 2I3}\right\} \qquad (2.24)$$

The same algorithm is applied in the deformed condition to obtain ϕ_2.

2.4.3 Processing Step: Unwrapping of the Phase Difference

Because of the multivalued *arctan* function in the Equation 2.24, the phase difference map $\Delta\phi_w = \phi_1 - \phi_2$ results in a sawtooth shape function wrapped in the range of $(-\pi,\ \pi)$, with discontinuities every time the phase difference rolls over the 2π boundary. For

this reason, is necessary to unwrap the phase by adding or subtracting an adequate multiple of 2π to all pixels for each phase jump. Figure 2.23 shows the phase unwrapping approach when $\Delta\phi_w$ is increased.

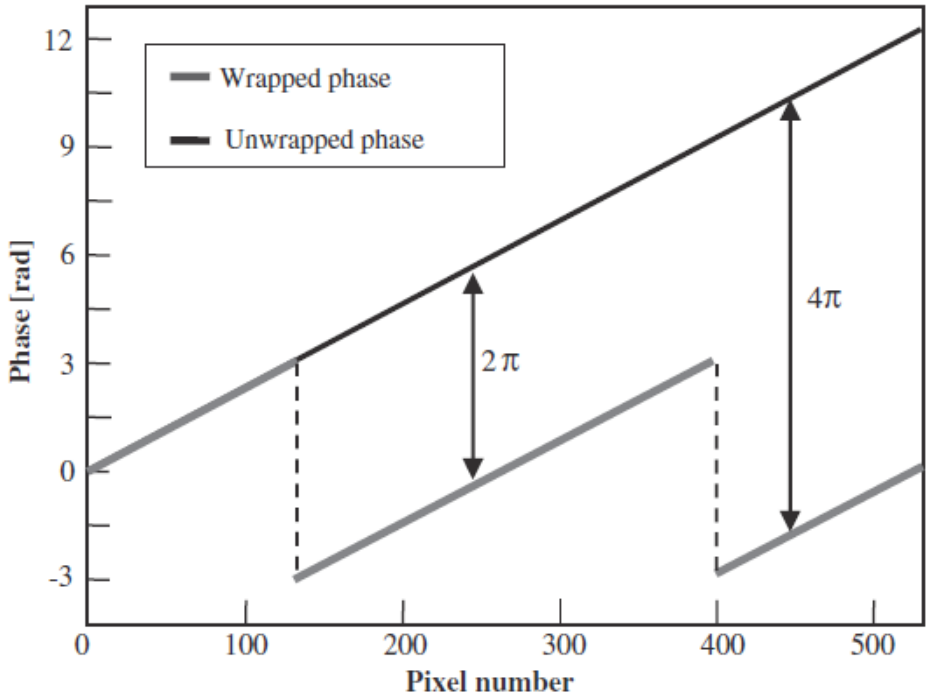

Figure 2.23. Unwrapped and wrapped phases [47].

The key to reliable phase-unwrapping algorithms is related to the ability to accurately detect the 2π phase jumps. Ghiglia and Romero [52] provided a family of global optimization methods which take the phase difference between adjacent pixels to identify these discontinuities, and seek the unwrapped solution by minimizing the difference between the gradients of the wrapped and unwrapped phase.

For a better understanding of unwrapping process, Figure 2.24.a shows a simulated fringe pattern resulting from the difference of two specklegrams, and its modulo 2π wrapped phase ($\Delta\phi_w$). Figure 2.24.b. shows the phase map after unwrapping ($\Delta\phi$).

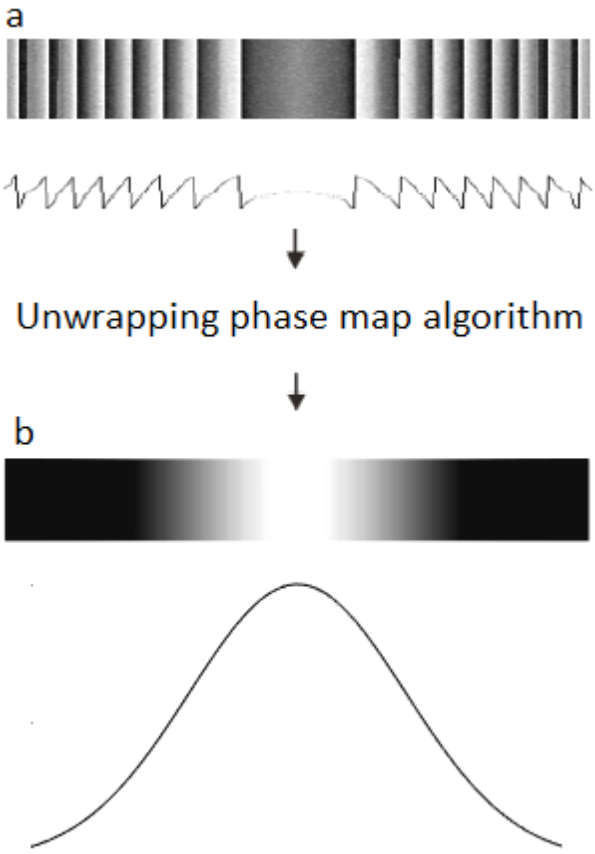

Figure 2.24 a) Phase difference map before phase unwrapping ($\Delta\phi_w$); b) Phase difference map after phase unwrapping ($\Delta\phi$). (Adapted from [53]).

Finally, the values of the unwrapped phase ($\Delta\phi$) are substituted in Equation 2.22 to obtain the magnitude of the relative displacements.

3 EXPERIMENTAL PROCEDURE

This chapter describes the methodology used to measure residual stress by combining the slitting method and DSPI. Section 3.1 summarizes the procedure to evaluate the feasibility of the slitting-DSPI technique. Section 3.2 describes the preparation of the specimens to be used, as well as the measurement of their near-surface residual stresses by the hole-drilling method. Section 3.3 describes the equipment applied to slit the specimens and the cutting parameters. Sections 3.4 and 3.5 present the slitting experiments made by using DSPI and strain gage. Section 3.4 also details the components of the DSPI system and the data management to compute strains.

3.1 Experimental Planning

The feasibility of the slitting method combined with DSPI to measure through-thickness residual stresses was evaluated by taking the following steps:

1. Specimens preparation: two types of specimens from the same material are made to be used as reference. Their respective near-surface stress distributions are obtained by the hole- drilling method to compare with the slitting results.
2. Experiment 1: Residual stresses in a stress-relieved specimen are computed by using DSPI measurements.
3. Experiment 2: Residual stresses in a plastically bent specimen are computed by using DSPI measurements.
4. Experiment 3: Residual stresses in a plastically bent specimen are computed by using strain gage measurements.

3.2 Specimens

Three A36 carbon steel beams with special stress conditions were used to validate the implemented methodology. The dimensions of their cross-section were chosen similar to a tensile armor wire cross-section. Figure 3.1 shows the A36 beams as received from the

manufacturer. Table 3.1 summarizes the dimensions and the stress condition for each sample. Additionally, it shows the way the strains are measured.

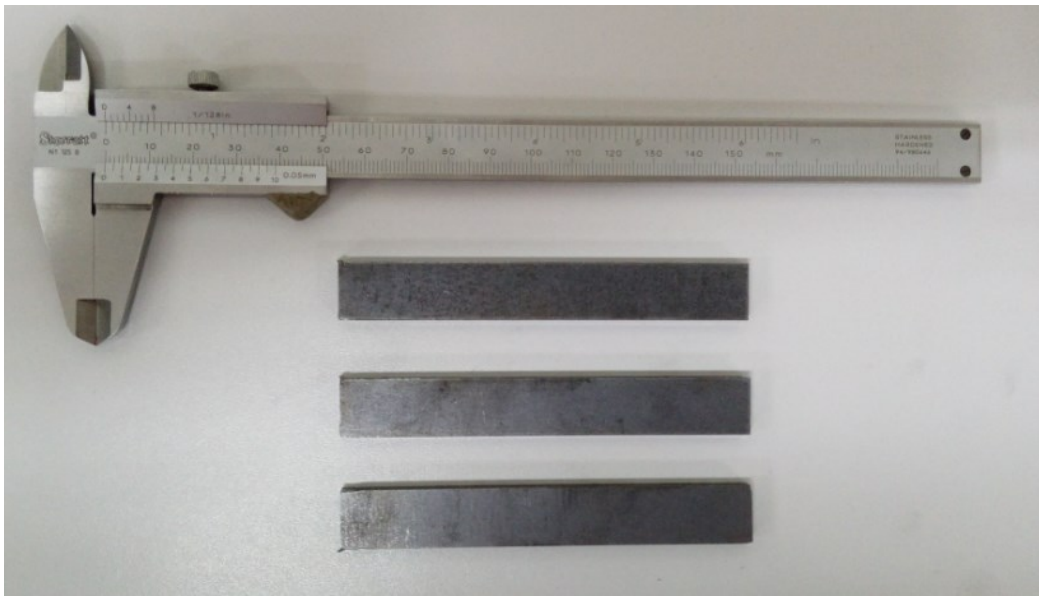

Figure 3.1. Steel beams specimens.

Table 3.1 – Dimensions and stress condition for the beam specimens.

	Specimens		
	1	**2**	**3**
Length (mm)	100	100	100
Width (mm)	14	14	14
Thickness (mm)	4.7	4.7	4.7
Stress condition	Relieved	Loaded	Loaded
Strains measurement by	DSPI (experiment 1)	DSPI (experiment 2)	Strain gage (experiment 3)

The beam 1 was subjected to a normalizing heat treatment in a furnace at a heating rate of 3.7 °C/min from the ambient temperature up to 915°C. After that, it was remained at this temperature for 30 minutes. Afterwards, it was cooled in air up to ambient temperature.

Specimens 2 and 3 were first subjected to the same stress-relief treatment described above. Next, they were plastically deformed using a four-point fixture (Figure 3.2) in order to introduce axial residual stresses in the central region (between the inner pins). The procedure involved loading the beams beyond the elastic limit, followed by unloading. This creates a

residual stress profile through the specimen's thickness that can be computed by using an elastic-plastic analysis [54].

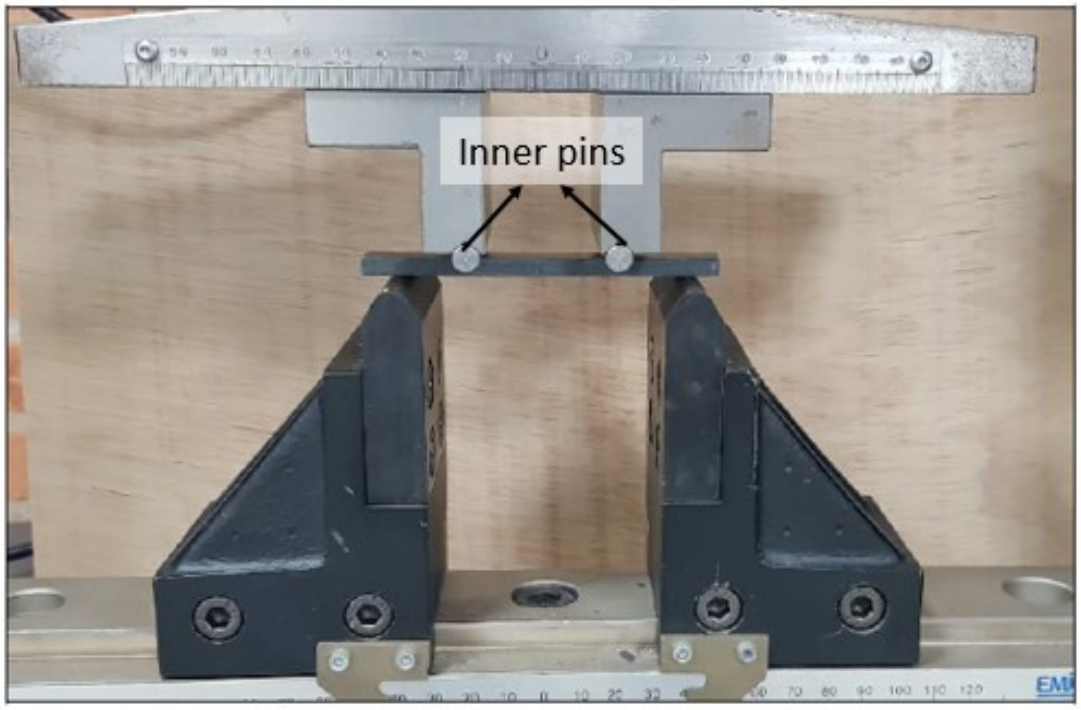

Figure 3.2. Four-point bending of beams 2 and 3.

The bending tests were controlled by an INSTROM universal testing system. The applied load was increased slowly such that the strain rate of the beams were 0.0001 s^{-1} (100 μstrain/s). The maximum force exerted in both cases was approximately 1.6 kN, reaching 0.0045 strain (4500 μstrain) in the middle-length of the specimens. Figure 3.3 shows the expected residual stress profile after the loading/unloading process, determined by finite element analysis. The model was built in ANSYS to simulate the beam size and the four-point bending diagram (load and support span), using the maximum force applied by the INSTROM system and the material properties provided by the beams manufacturer (Young's modulus = 200 GPa, Yield strength = 300 MPa).

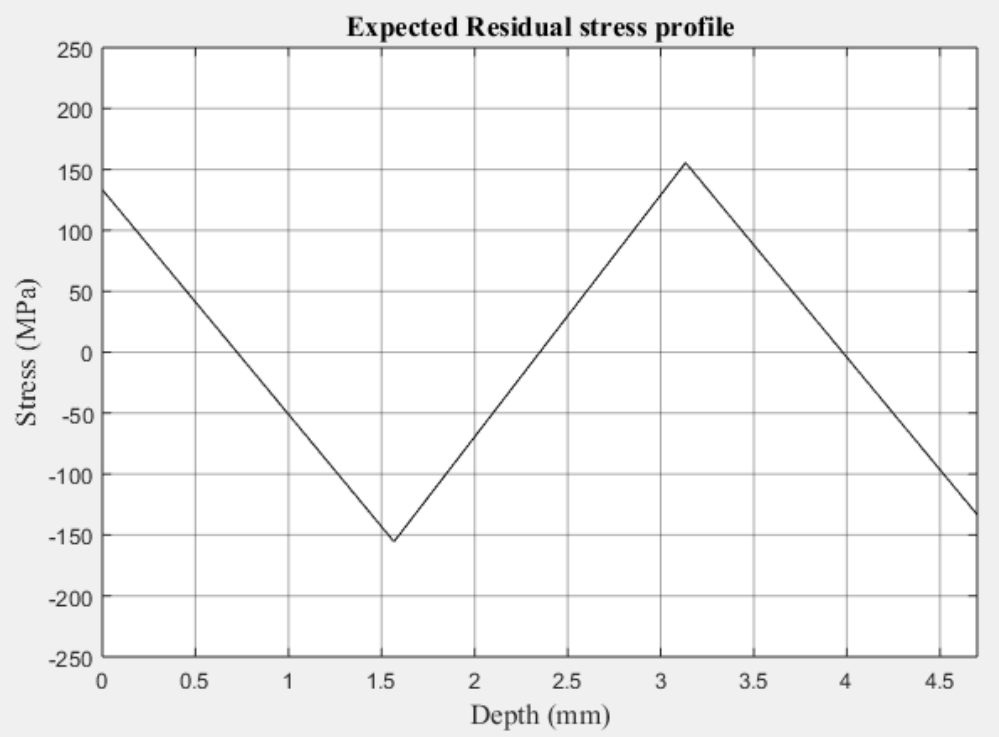

Figure 3.3. Expected residual stress profile after four-point bending.

Before conducting the slitting experiments, the near-surface residual stress distributions of specimens 1 and 2 were obtained by the hole-drilling method. For that, it was used a portable laser system for residual stress measurement (POLAR) developed at LABMETRO [27, 55].

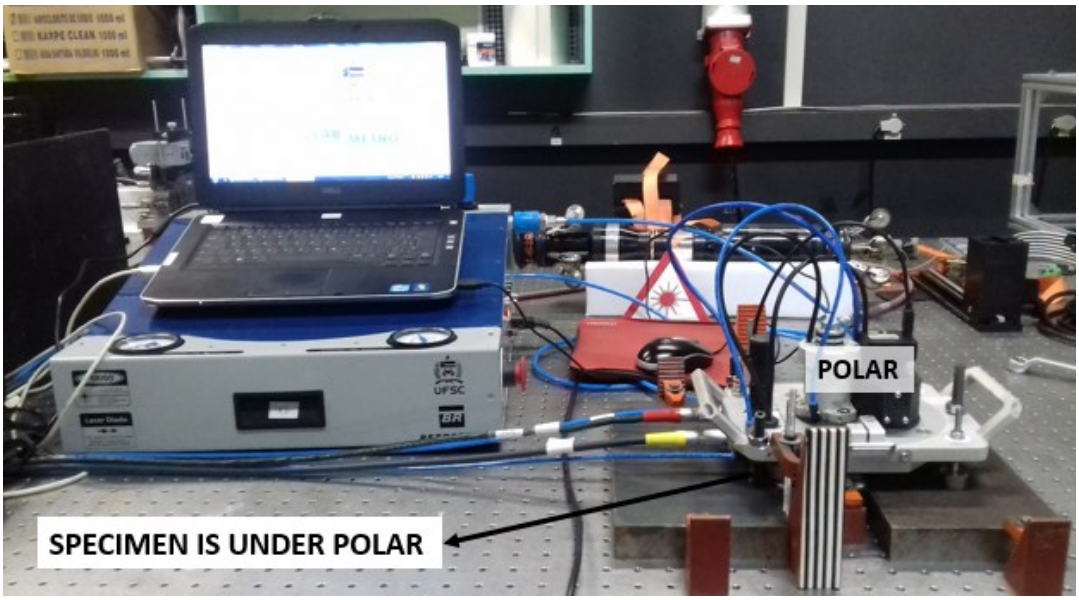

Figure 3.4. Near-surface residual stress measurement for specimens 1 and 2 by hole-drilling (POLAR).

The holes were drilled 10 mm away from the centerline of the specimens so as not to induce additional stresses in the region where the slit will be machined. Two blind holes were drilled in each beam, one at each surface (see Figure 3.5). The stress distributions obtained by POLAR system will be presented in chapter 4 as well as the comparison between them with the slitting results and expected distributions.

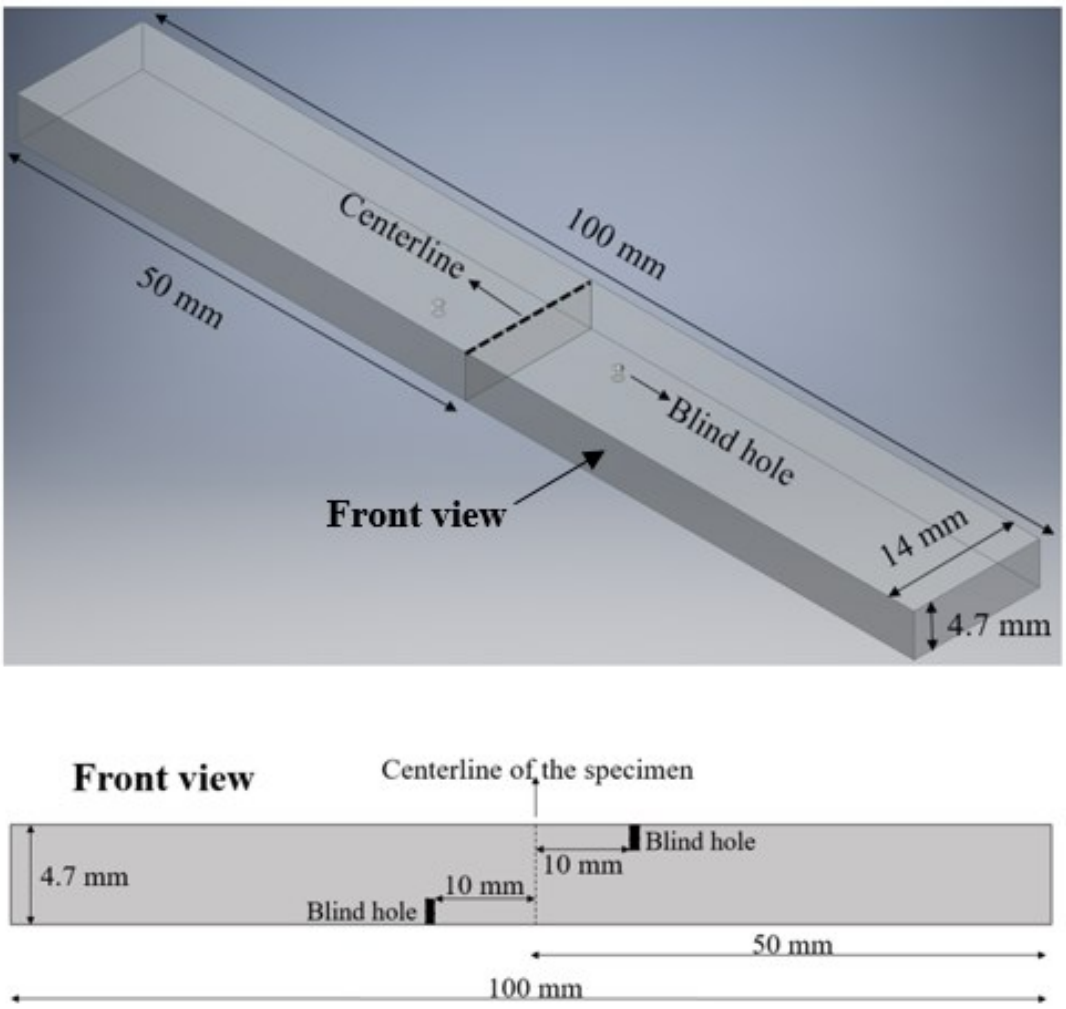

Figure 3.5. Blind holes drilled in specimens 1 and 2.

Once the near-surface residual stresses were obtained by POLAR, the specimens were cut in order to measure the through-thickness stress profiles by the slitting method.

3.3 Cutting Process

One side of the specimens was clamped to the top plate of a kinematic coupling, thus letting the opposite side to be free to deform (see Figure 3.6).

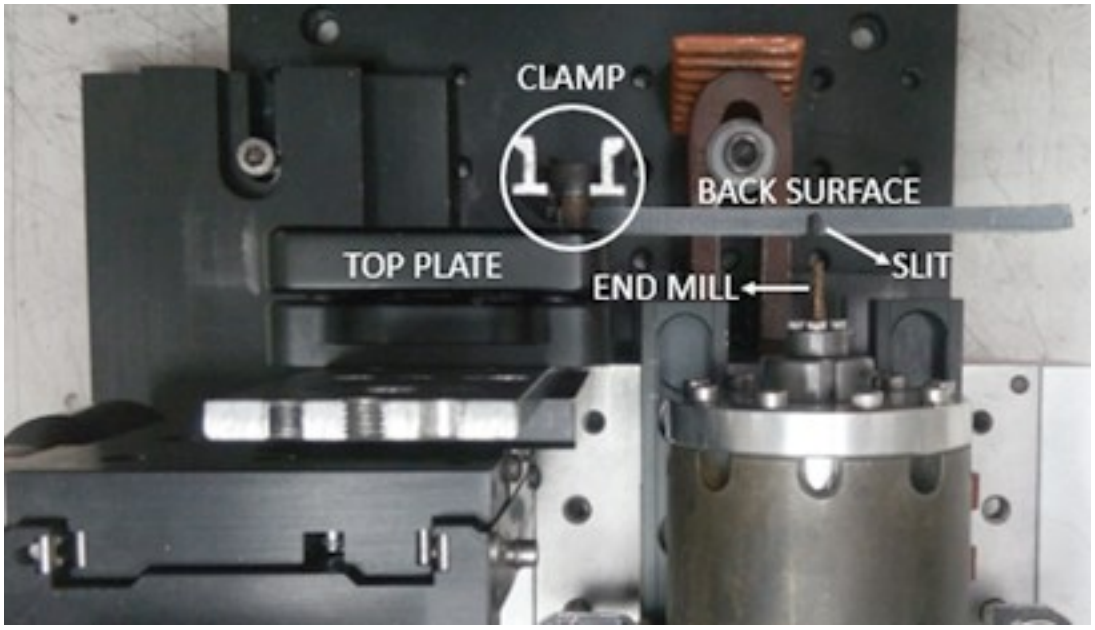

Figure 3.6. Clamped specimen.

The kinematic base was attached to a support fitted with stepper motor actuators capable to perform linear displacements along two directions. The slit was then introduced in the centerline of the specimens (see Figure 3.5) using an electric milling machine and moving the support along the *x* and *z* directions. Figure 3.7 shows the experimental setup for cutting.

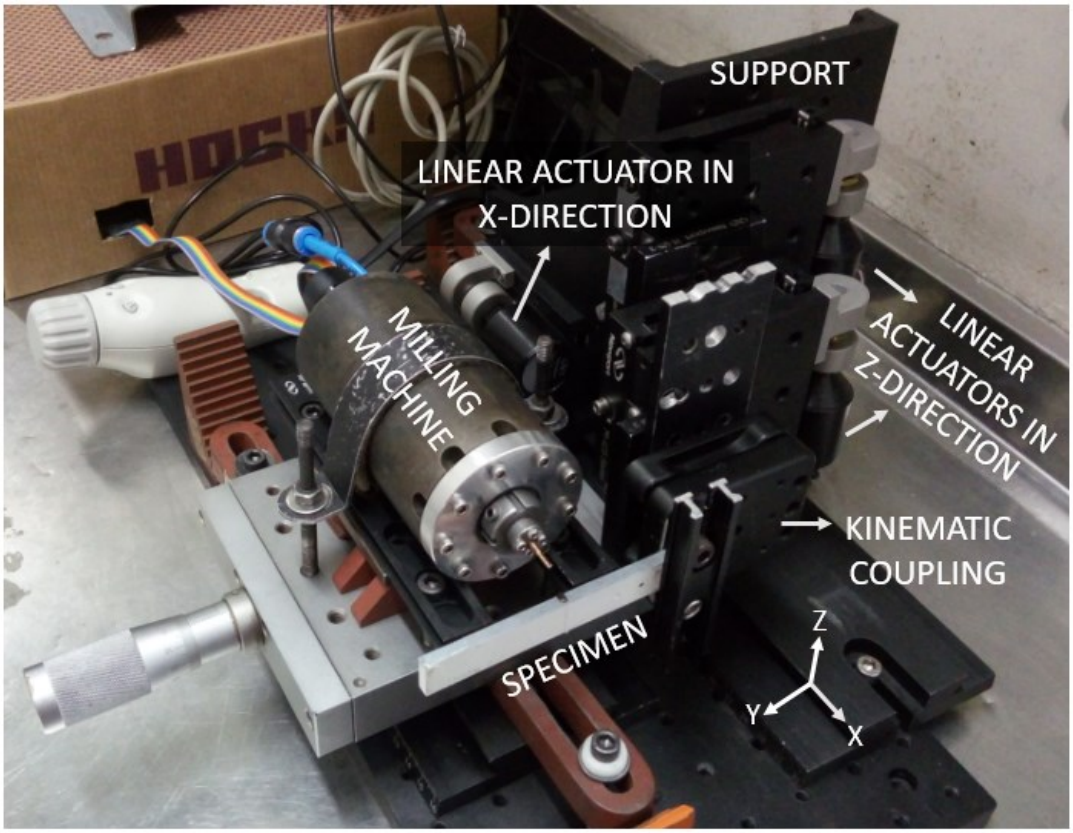

Figure 3.7. Cutting workbench.

The milling procedure was always repeated for all the specimens. It was controlled via a computer program to achieve good execution repeatability. The main information and parameters are below presented:

- Cutting tool: 2 mm diameter 4-flute titanium-coated end-mill. Figure 3.8 shows the milling cutter.
- Spindle speed: 5000 rpm.
- Depth increment for all slitting steps (in the *x*-direction, see Figure 3.7): 0.1 mm (100 μm).
- Final depth of the cut for all the specimens: 4 mm (40 increments).
- Velocity of the linear actuators in the *z*-direction (see Figure 3.7): 7.7 mm/min.

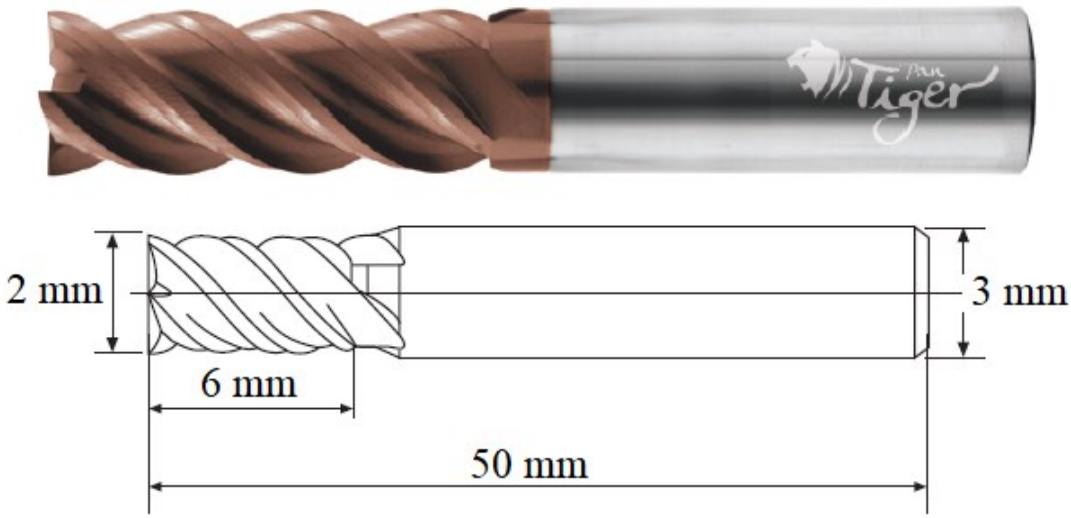

Figure 3.8. Milling cutter used to slitting. (Adapted from [56]).

In experiments 1 and 2, after each cut increment, the top plate where the specimen is clamped, was removed from the base and coupled in another kinematic fixture that is in front of the interferometer (which will be presented in the next section) to subsequently acquire digital images of the deformed back surface of the specimen. Once the images were obtained, the plate with the specimen was brought back to the cutting device to continue the experiment.

On the other hand, in experiment 3, the specimen was kept in the cutting workbench throughout the test, and the strains were measured in-place by the strain gauge at the completion of each slitting step.

3.4 Strain Measurement by Using a Dual Beam Interferometer

The DSPI technique was used in experiments 1 and 2 to obtain the strains in the back surface (see Figure 3.6) due to each slitting increment. As described in section 2.4.1, the configuration for measure this type of deformations is based on a symmetrical two-beam illumination. The following subsections will present information concerning to the strain measurements in both experiments, from the interferometer used up to the image processing.

3.4.1 Optical Setup

Figure 3.9 shows the speckle interferometer used in this work. It was assembly in an optical table in such a way that it allows to measure surface displacements in the *y*-direction (see Figure 3.7 and 3.9). Table 3.2 details the components of the DSPI system.

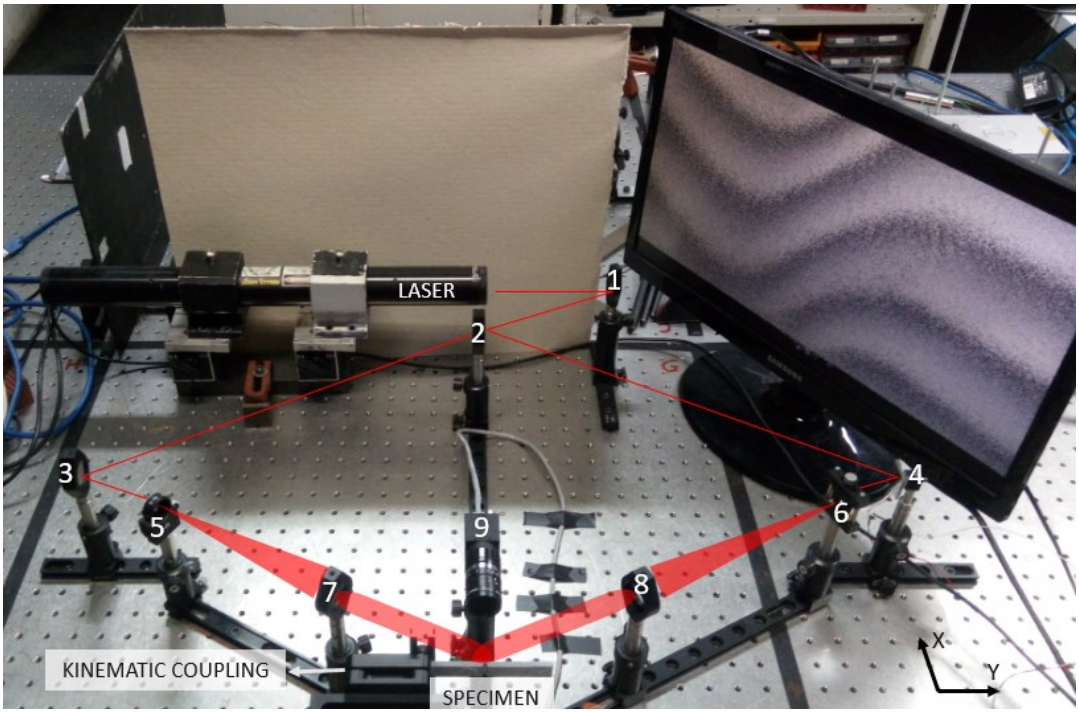

Figure 3.9. Dual beam interferometer.

Table 3.2 – Components of the interferometer.

Component	**Description**
Laser	Helium-neon laser. Wavelength: 632.8 nm
1	Flat mirror
2	Broadband dielectric beamsplitter
3	Flat mirror
4	Flat mirror mounted on a piezoelectric translator
5	Bi-concave lens
6	Bi-concave lens
7	Bi-convex lens. 25.4 mm diameter
8	Bi-convex lens. 25.4 mm diameter
9	CCD camera. Resolution: 1600 x 1200 pixels

In this arrangement, the light from the laser source is divided by the beamsplitter in two beams that travel the same optical path length to the back surface of the specimen. After the beamsplitter, both beams are reflected by mirrors 3 and 4, and expanded by lens 5 and 6. Lens 7 and 8 collimate the beams that interfere on the surface opposite to the slit with an illumination angle of 60° (which provided the maximum measurement sensitivity on the surface available to work in the optical table). Finally, a CCD camera records the interference pattern of the illuminated area.

3.4.2 Data Acquisition

The phase maps corresponding to the deformed state after each cut increment were obtained using the five-frame algorithm (described in section 2.4.2). The flowchart in Figure 3.10 depicts the procedure followed to obtain them.

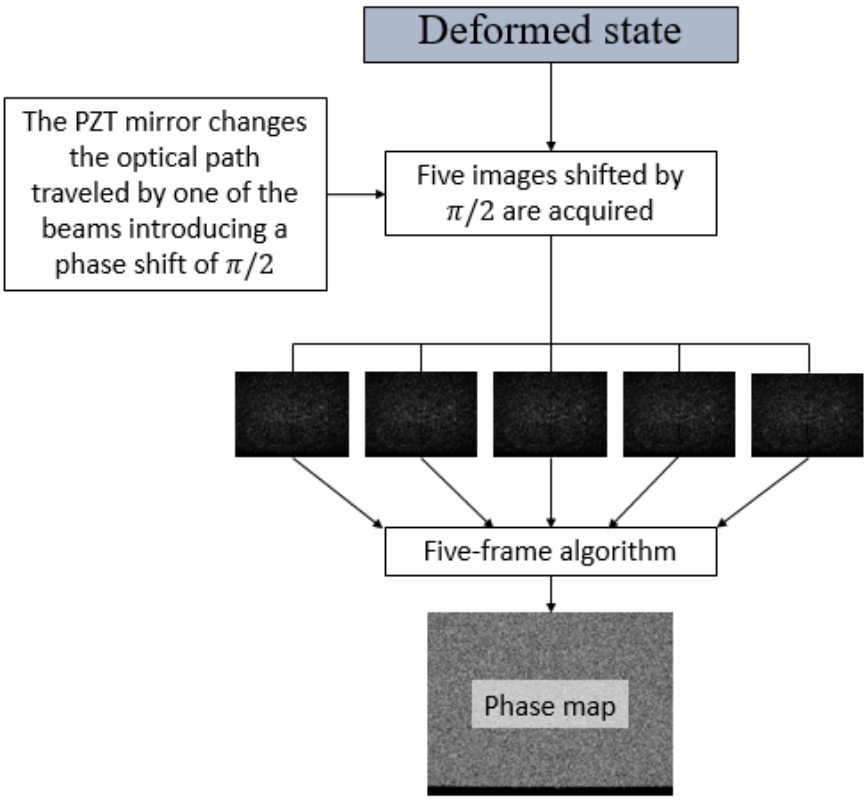

Figure 3.10. Procedure to obtain the phase maps.

Before the first cut increment, it was acquired a phase map of the undeformed surface to be used as reference. In total, 41 phase maps were acquired, one at each state.

Next, two consecutive phase maps (each phase map is used as reference for the next depth increment) are subtracted to obtain the wrapped phase difference caused by the surface deformation. Figure 3.11 depicts this procedure.

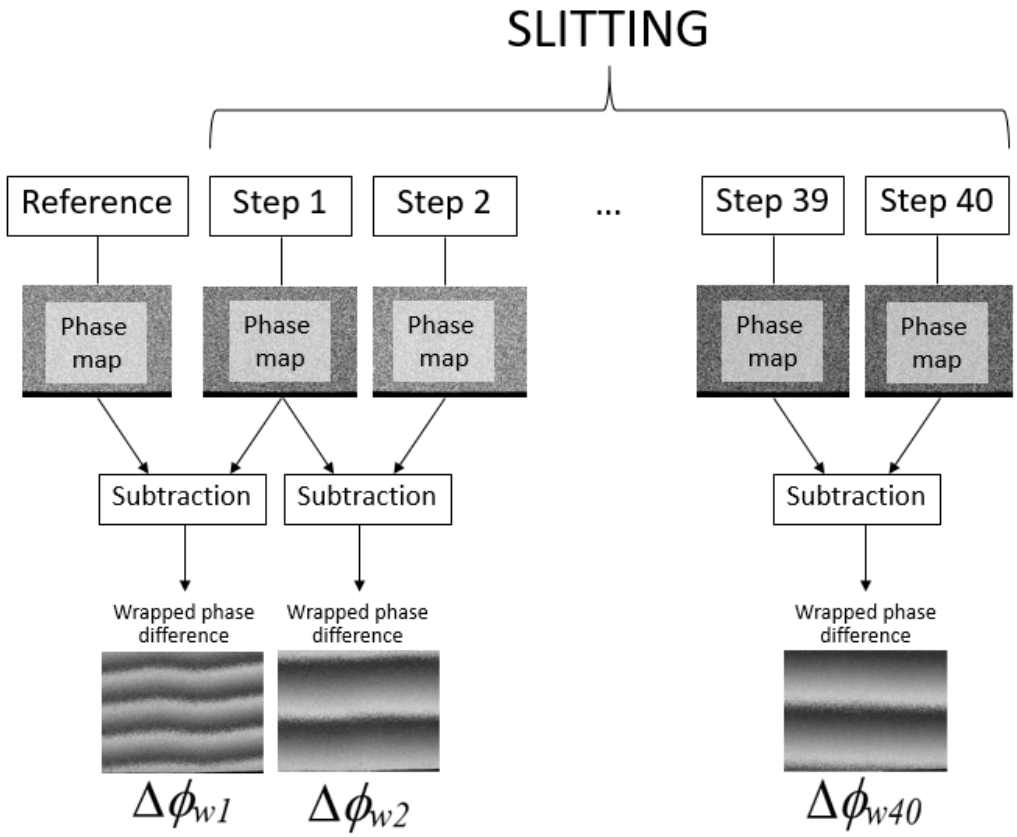

Figure 3.11. Procedure to obtain the wrapped phase difference.

A total of 40 phase difference maps were acquired (one for each increment) and stored in a computer for further processing. Figures 3.12 and 3.13 show the first nine wrapped phase differences for experiments 1 and 2.

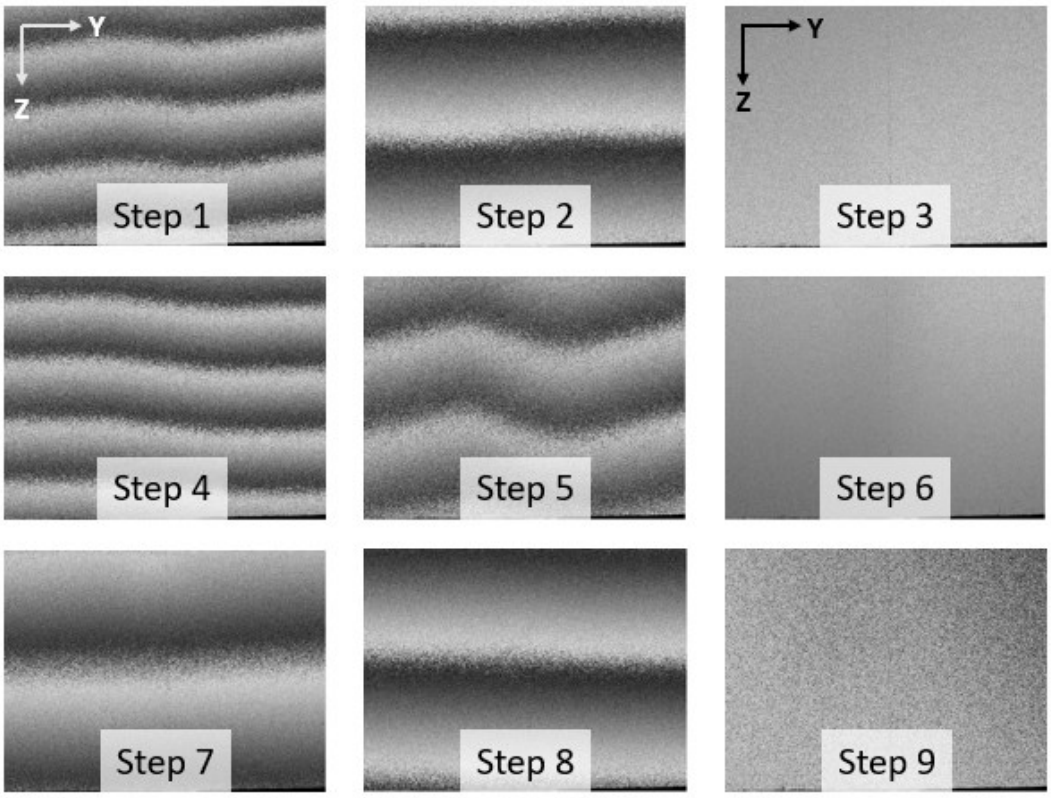

Figure 3.12. First nine wrapped phase differences for experiment 1 (relieved beam).

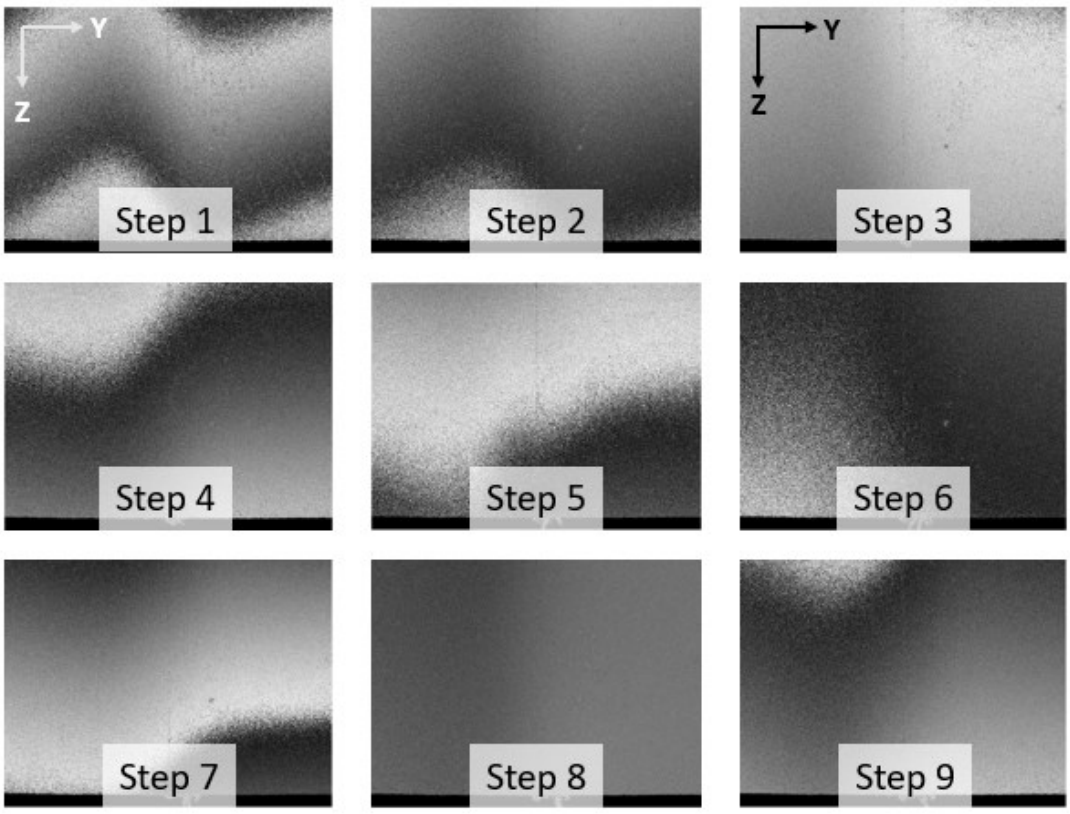

Figure 3.13. First nine wrapped phase differences for experiment 2 (loaded beam).

The images in Figures 3.12 and 3.13 contain the displacement information (between two consecutive increments) of the illuminated area. As can be seen, the fringes do not have a defined pattern. This is because they are a combination of deformations in the *y*-direction and rigid body motions due to the not perfect repositioning of the top plate in the kinematic coupling. Therefore, more fringes do not necessarily means a larger deformation. Moreover, images with no fringes represent both: small deformation and no rigid body motion.

3.4.3 Strain Calculation: Image Processing

In order to calculate strain magnitudes from DSPI images, it was necessary to remove the 2π discontinuities of the wrapped phase differences (as described in section 2.4.3). In this work it was used a phase-unwrapping algorithm based on Ghiglia and Romero method [52]. The unwrapping process and the further strain calculation were done via MatLab.

Figure 3.14 depicts the unwrapping of the phase difference for the final increment in experiment 1 (relieved beam). The process was always the same for all the deformed states in both experiments.

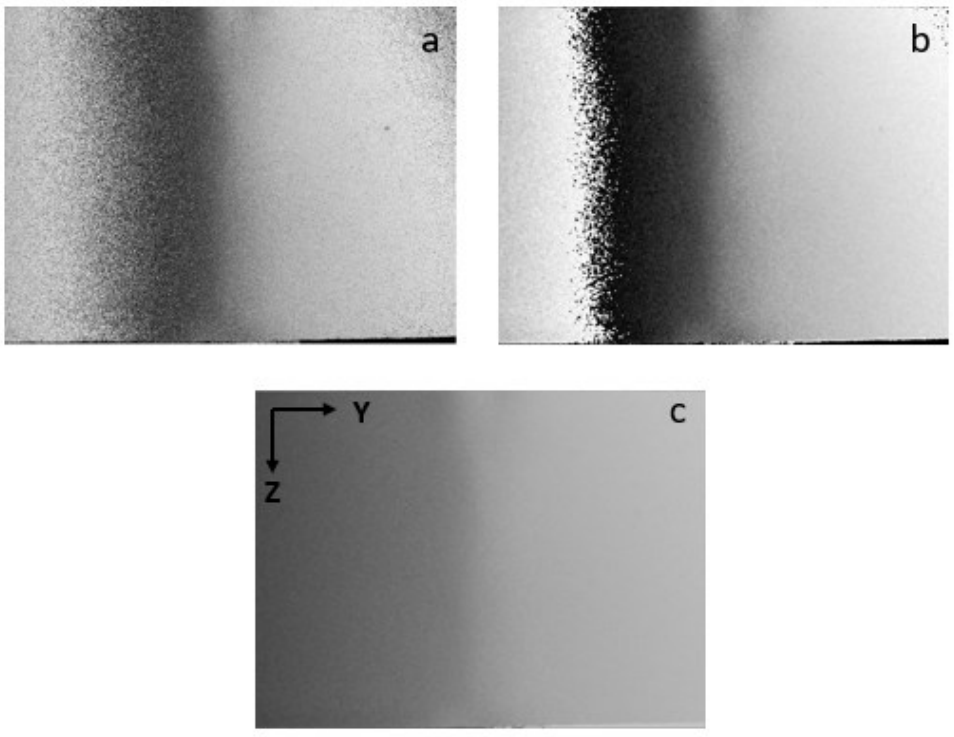

Figure 3.14. a) Wrapped phase difference; b) Filtered wrapped phase difference; c) Unwrapped (absolute) phase difference.

After the unwrapping process, the absolute phase difference ($\Delta\phi$) was substituted in Equation 2.22 to calculate the displacement map, i.e., the displacement magnitudes in the *y*-direction for all the pixels in the image.

$$d = \frac{\lambda}{4\pi(sin\gamma)}\Delta\phi \qquad (2.22)$$

Where the illumination angle (γ) was 60º (1.047 rad), and the wavelength of the laser (λ) was 632.8 nm (0.6328 µm).

The resulting displacements were then used to compute the strain magnitudes. For that it was necessary to know the pixel-mm relation of the interferometer (see Figure 3.15). In this case 1 mm corresponds approximately to 88 pixels.

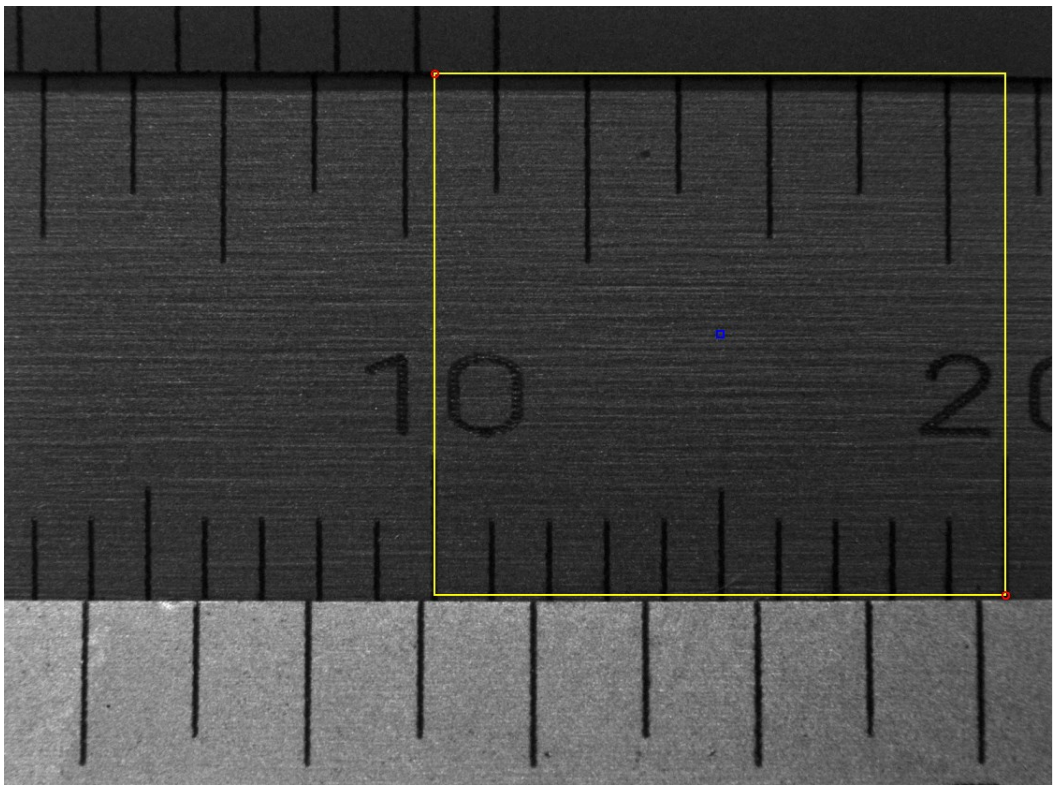

Figure 3.15. Pixel-mm relation of the interferometer. The base of the yellow square (10 mm) covers 875 pixels approximately.

Figure 3.16 depicts the process to compute the strain. The area of interest (yellow area in Figure 3.16.a) corresponds to the area that would be occupied by the grid of a 5 mm length strain gage mounted on the surface opposite the cut, oriented in the *y*-direction. The pixel column 800 in Figure 3.16.a corresponds to the centerline of the specimen, that is, the

strain gage would be aligned with the center of the slit (see configuration in Figure 2.15). Therefore, two points in the pixel row 600 are chosen (see Figure 3.16.b): y = 580 (at the pixel column 580) and y = 1020 (at the pixel column 1020).

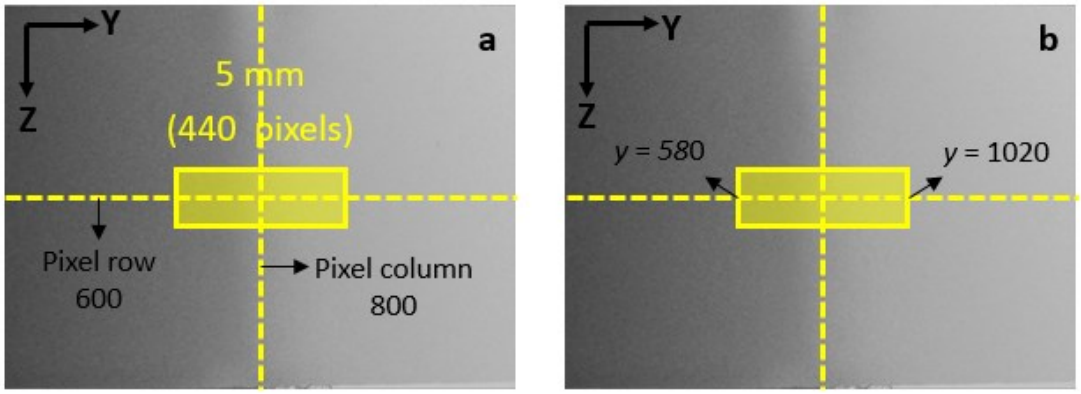

Figure 3.16. a) Area of interest; b) Selected points.

The strain is then calculated using the equation:

$$\varepsilon_{meas} = \frac{d(y = 580) - d(y = 1020)}{L} \qquad (3.1)$$

Where $d(y = 580)$ and $d(y = 1020)$ are the displacements at the selected points, and $L = 5\ mm$. This procedure is repeated for all cut increments in both experiments. Tables 3.3 and 3.4 present the cumulative strains for experiments 1 and 2.

Table 3.3 – Cumulative strains in experiment 1 (relieved beam).

Step	Depth (mm)	μstrain
1	0.1	-3.71
2	0.2	-8.87
3	0.3	-11.73
4	0.4	-21.48
5	0.5	-18.04
6	0.6	-22.91
7	0.7	-18.04
8	0.8	-19.18
9	0.9	-15.74
10	1	-23.20
11	1.1	-23.20
12	1.2	-22.91
13	1.3	-21.76
14	1.4	-23.20
15	1.5	-22.34
16	1.6	-30.65
17	1.7	-26.06
18	1.8	-27.21
19	1.9	-24.63
20	2	-30.65

Step	Depth (mm)	μstrain
21	2.1	-32.08
22	2.2	-26.06
23	2.3	-33.22
24	2.4	-35.80
25	2.5	-34.66
26	2.6	-40.39
27	2.7	-39.24
28	2.8	-42.68
29	2.9	-45.83
30	3	-49.84
31	3.1	-53.86
32	3.2	-54.14
33	3.3	-56.15
34	3.4	-80.22
35	3.5	-83.66
36	3.6	-101.14
37	3.7	-105.72
38	3.8	-124.35
39	3.9	-120.62
40	4	-165.04

Table 3.4 – Cumulative strains in experiment 2 (loaded beam).

Step	Depth (mm)	μstrain
1	0.1	-34.00
2	0.2	-46.01
3	0.3	-56.61
4	0.4	-73.51
5	0.5	-88.41
6	0.6	-99.59
7	0.7	-106.75
8	0.8	-119.93
9	0.9	-128.24
10	1	-144.86
11	1.1	-149.16
12	1.2	-154.32
13	1.3	-153.46
14	1.4	-158.61
15	1.5	-143.71
16	1.6	-134.54
17	1.7	-107.90
18	1.8	-83.54
19	1.9	-35.97
20	2	-22.22

Step	Depth (mm)	μstrain
21	2.1	36.52
22	2.2	69.76
23	2.3	130.22
24	2.4	139.97
25	2.5	175.21
26	2.6	171.20
27	2.7	184.38
28	2.8	170.05
29	2.9	170.05
30	3	143.69
31	3.1	104.15
32	3.2	71.48
33	3.3	62.60
34	3.4	41.11
35	3.5	13.89
36	3.6	-11.62
37	3.7	-56.32
38	3.8	-106.75
39	3.9	-158.61
40	4	-246.30

Figures 3.17 and 3.18 show the strain values above presented as function of the cutting depth.

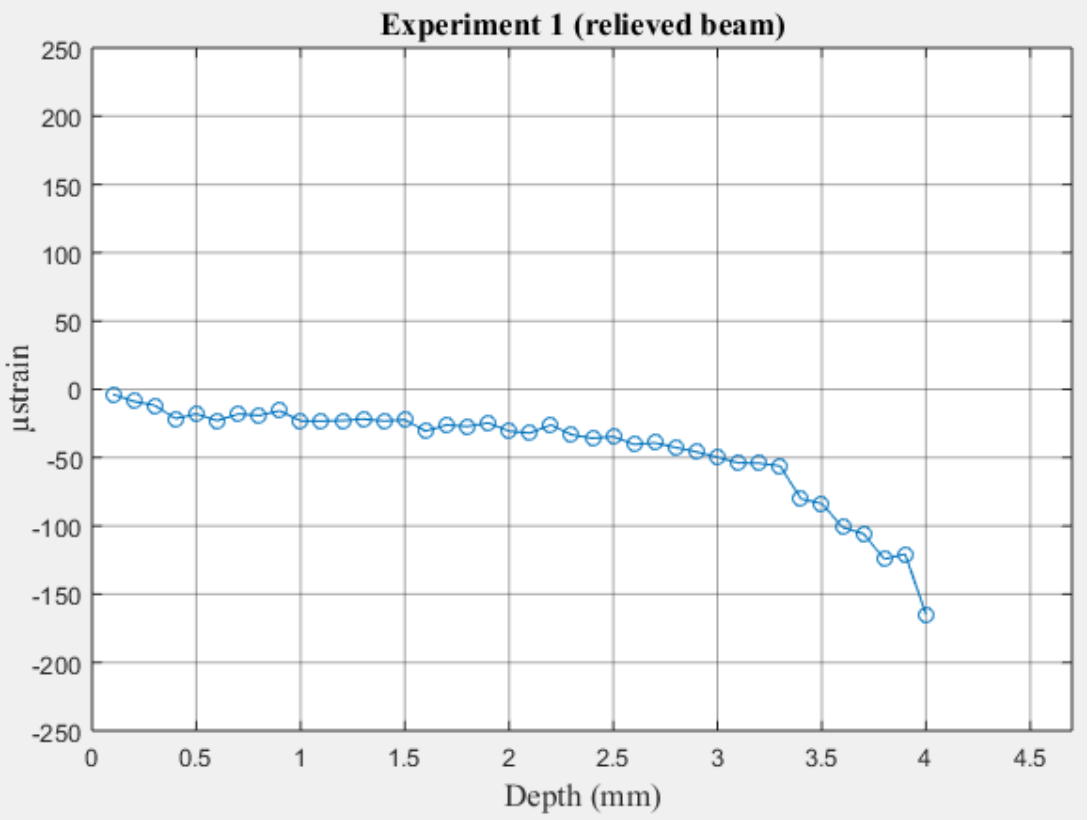

Figure 3.17. Cumulative strains in experiment 1 (relieved beam).

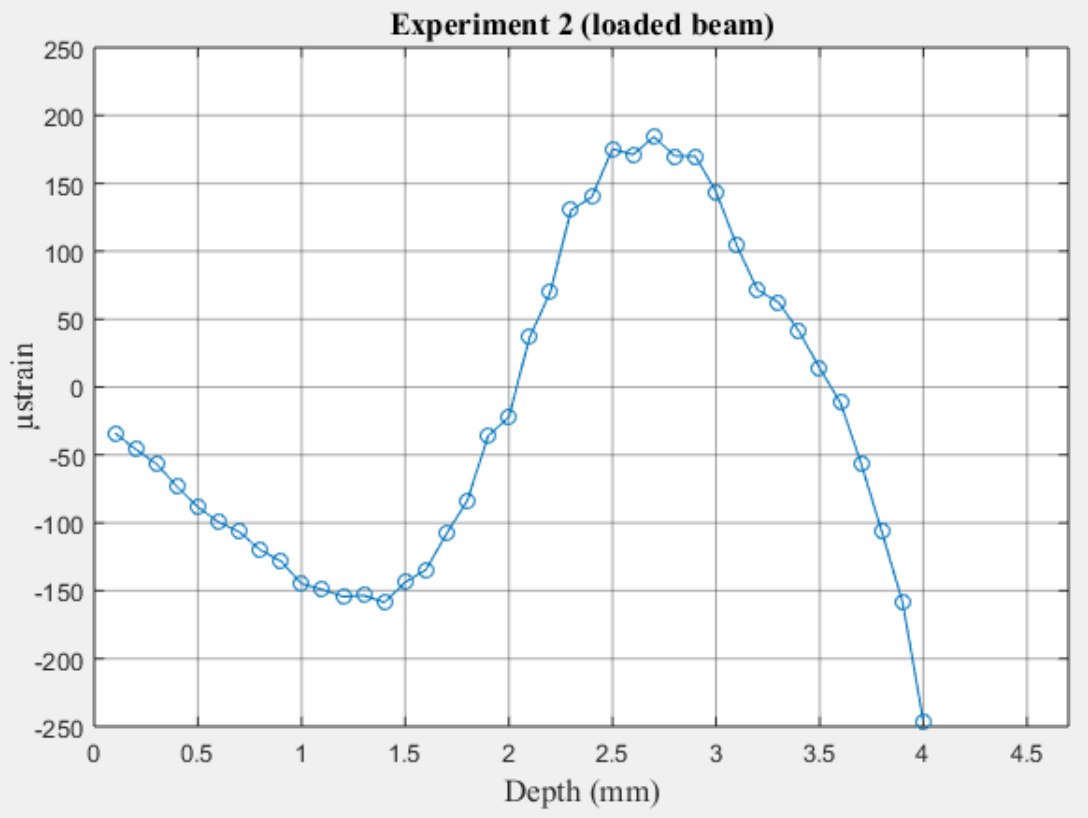

Figure 3.18. Cumulative strains in experiment 2 (loaded beam).

Figure 3.17 shows only compressive strains for the relieved beam. The graph is fairly uniform without relevant changes in its tendency.

On the other hand, Figure 3.18 shows both compressive and tensile strains. As can be seen, it seems that due to the load condition, the tendency (slope) of the graph changes as the cut depth increases.

These strain magnitudes are used to compute the residual stress profile of the specimens. The results will be presented in chapter 4.

3.5 Strain Measurement by Using Strain Gage

In the experiment 3 (loaded beam), the strains in the back surface due to slitting were measured with a 5mm length strain gage, mounted in a configuration similar to the one presented in Figure 2.15, that is, aligned with the center of the slit. Figure 3.19 shows an image of the strain gage glued on the specimen, the yellow area represents the area of interest described in section 3.4.3.

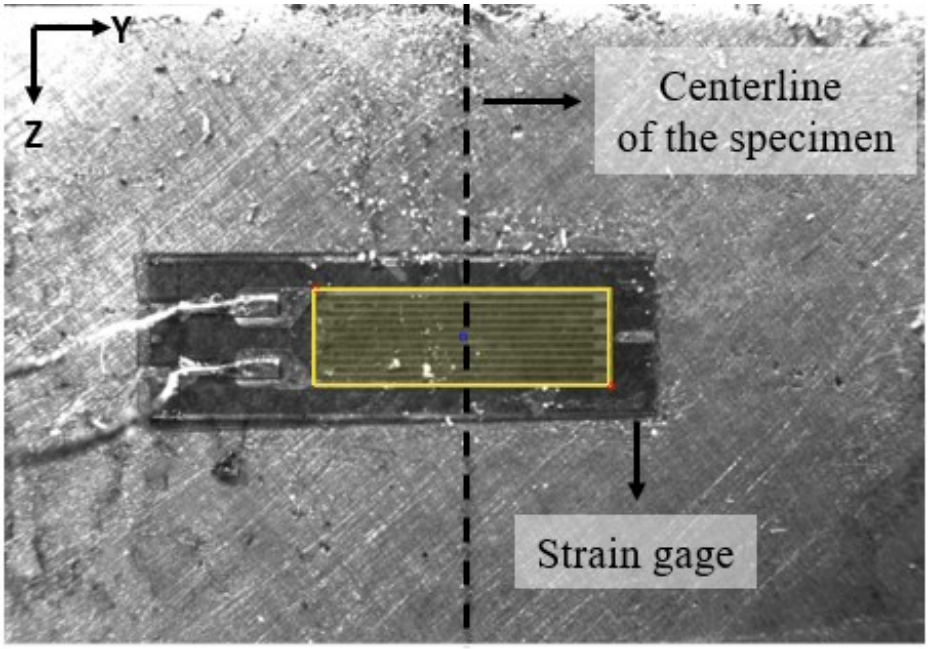

Figure 3.19. Strain gage glued in the surface opposite the slit.

The strain magnitudes after each slitting increment were obtained by using a quarter-bridge circuit. Figure 3.20 shows the workbench for experiment 3.

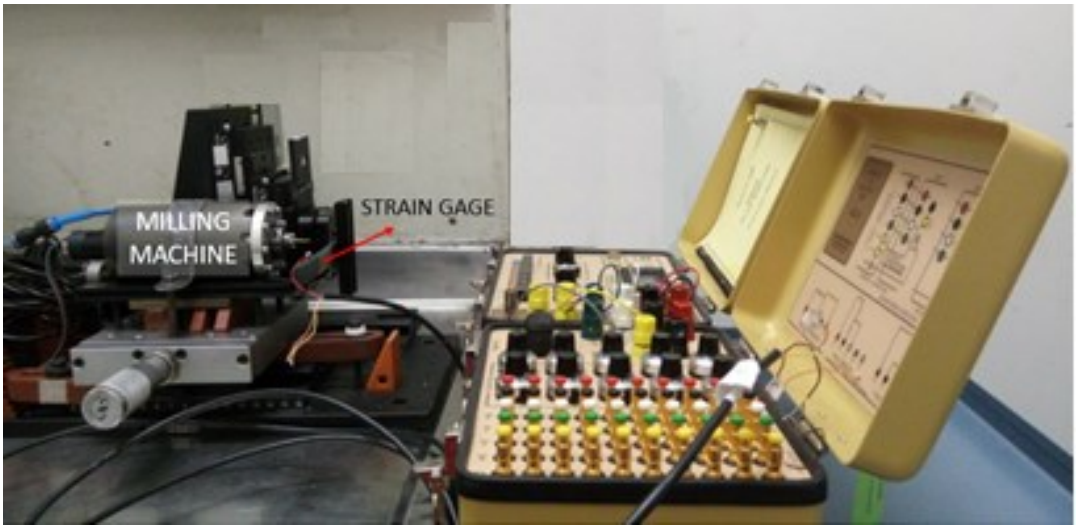

Figure 3.20. Experiment 3 (slitting – strain gage).

Table 3.5 presents the cumulative strains for this experiment, which will be used to compute the residual stress in chapter 4. Figure 3.21 shows the values as function of the cutting depth.

Table 3.5 – Cumulative strains in experiment 3 (loaded beam).

Step	Depth (mm)	µstrain
1	0.1	-37
2	0.2	-55
3	0.3	-73
4	0.4	-83
5	0.5	-82
6	0.6	-98
7	0.7	-111
8	0.8	-113
9	0.9	-109
10	1	-112
11	1.1	-110
12	1.2	-114
13	1.3	-118
14	1.4	-117
15	1.5	-100
16	1.6	-82
17	1.7	-53
18	1.8	-12
19	1.9	2
20	2	57

Step	Depth (mm)	µstrain
21	2.1	80
22	2.2	101
23	2.3	126
24	2.4	140
25	2.5	160
26	2.6	172
27	2.7	180
28	2.8	185
29	2.9	160
30	3	137
31	3.1	115
32	3.2	80
33	3.3	67
34	3.4	33
35	3.5	16
36	3.6	-4
37	3.7	-38
38	3.8	-40
39	3.9	-46
40	4	-52

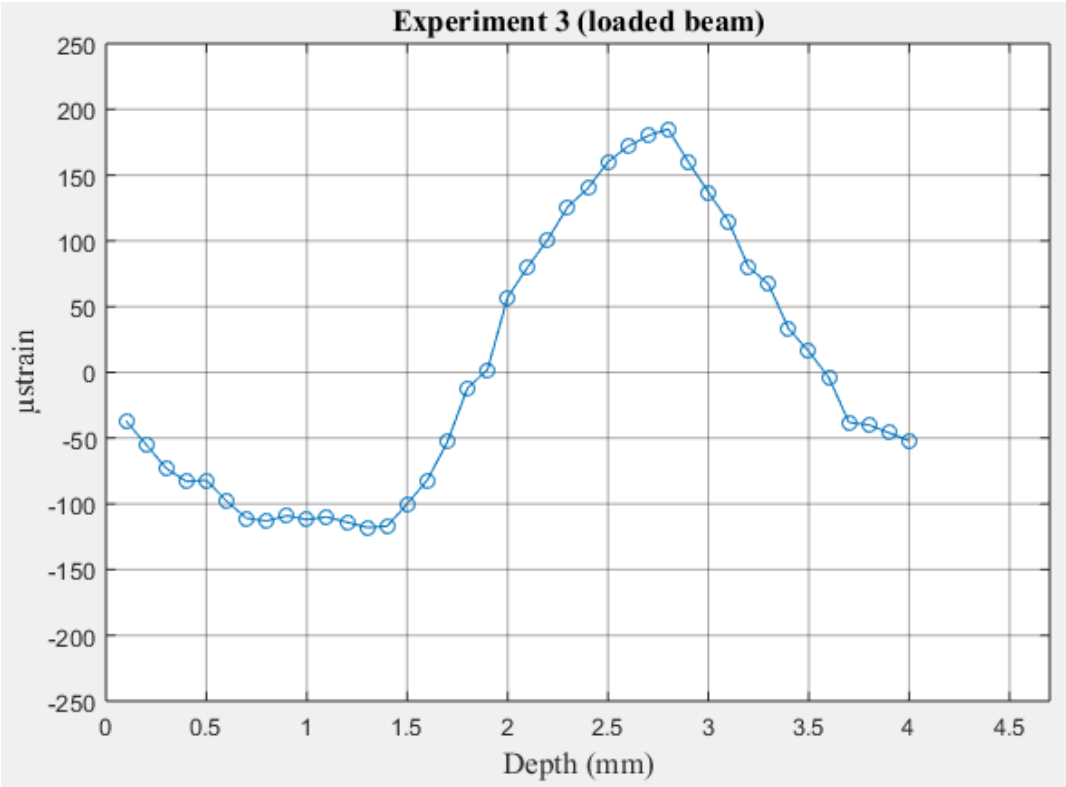

Figure 3.21. Cumulative strains in experiment 3 (loaded beam).

For a better comparison, Figure 3.22 shows the three strain profiles obtained in the experiments.

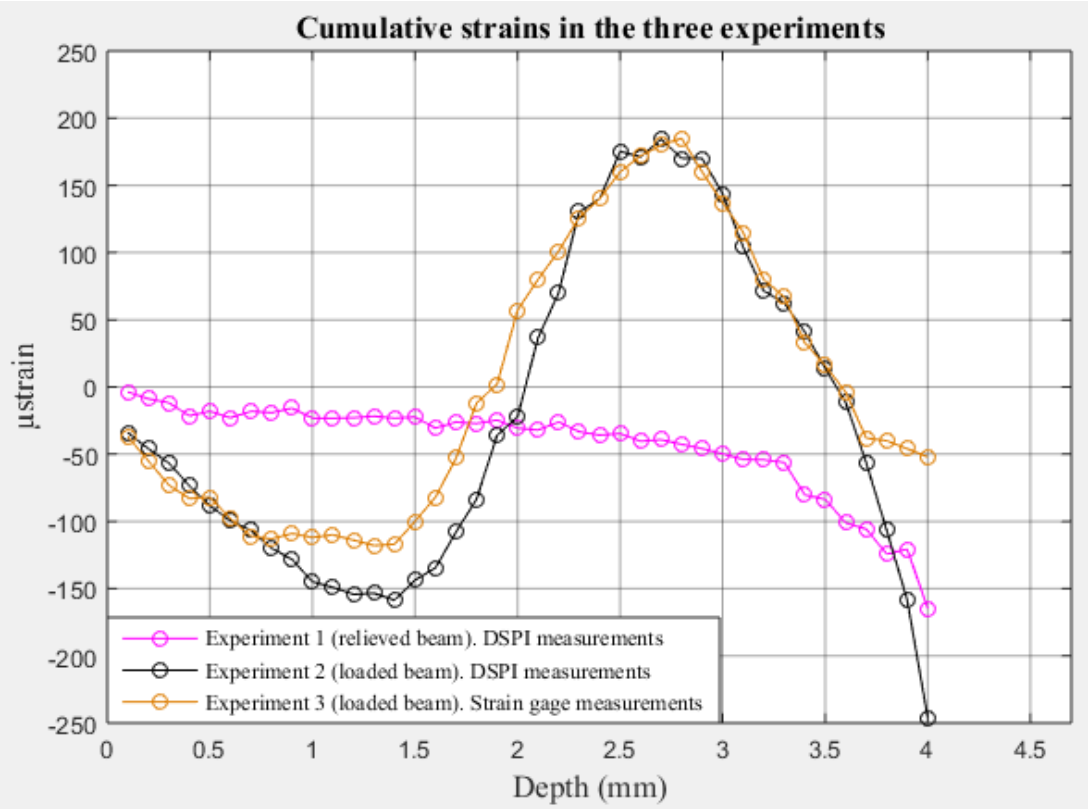

Figure 3.22. Cumulative strains in the three experiments.

As can be seen, the strains in experiments 2 and 3 (black and orange curves in Figure 3.22) are very similar. This agreement is because both specimens were subjected to the same bending process, and demonstrates that the interferometer is able to measure the deformations due to slitting. The difference of both curves at the final steps could be due to problems in the fixture used to slitting. Maybe at the end of the experiment the specimen 3 was not properly cut and therefore no significant deformations were measured in these last increments.

4 RESULTS AND DISCUSSION

This chapter presents the residual stress distributions obtained in the three experiments, as well as the discussion of these results. Section 4.1 describes the procedure used to estimate the residual stress distributions for the three specimens. Sections 4.2 and 4.3 show the through-thickness stress profiles calculated by the slitting method for specimens 1 and 2 respectively, and their near-surface residual stress distributions obtained by the hole-drilling method. Section 4.4 shows the residual stress profile calculated by the slitting method for specimen 3. Finally, section 4.5 presents the analysis of the experimental results.

4.1 Residual Stress Approximation

In order to use the compliances published in [40], the residual stress distribution as function of the slit depth for the three specimens was approximated by a 12^{th} order truncated Legendre polynomial. Thus, Equation 2.5 becomes:

$$\sigma_y(x) = \sum_{j=2}^{12} L_j(x) A_j \qquad (4.1)$$

Or, adopting matrix notation:

$$\{\sigma_y\} = [L]\{A\} \qquad (4.2)$$

Where $\{\sigma_y\}$ is a vector with 40 elements containing the stress magnitudes at the 40 slit depths, and $[L]$ is a 40×11 matrix with the values of the 11 Legendre terms at each slit depth.

The vector of the basis amplitudes $\{A\}$, was calculated using Equation 2.12:

$$\frac{1}{E'}\{A\} = ([C]^T[C])^{-1}([C]^T\{\varepsilon_{meas}\}) \qquad (2.12)$$

It was assumed plane strain state, that is, $E' = E/(1-\nu^2)$, with $E = 200$ GPa, and $\nu = 0.3$. The compliance matrix $[C]$ was obtained for the 40 slit depths using the closed form expression provided in [40]. The vector of measured strains $\{\varepsilon_{meas}\}$ contains the 40 strain values obtained in the experiments.

The residual stress distribution for each specimen was then estimated using a program written in Matlab following the next steps:

1. Obtain matrices $[L]$ and $[C]$ for the 40 slit depths.
2. Calculate the vector $\{A\}$ using Equation 2.12.
3. Calculate the stress vector $\{\sigma_y\}$ using Equation 4.2.

4.2 Experiment 1: slitting-DSPI (stress-relieved beam)

For specimen 1, the vector of measured strains $\{\varepsilon_{meas}\}$ in Equation 2.12 contains the 40 strain values of Table 3.3. Figure 4.1 shows the residual stress distribution as function of the specimen thickness, calculated with Equation 4.2. The points in the graphic correspond to the stress magnitudes for the 40 slit depths.

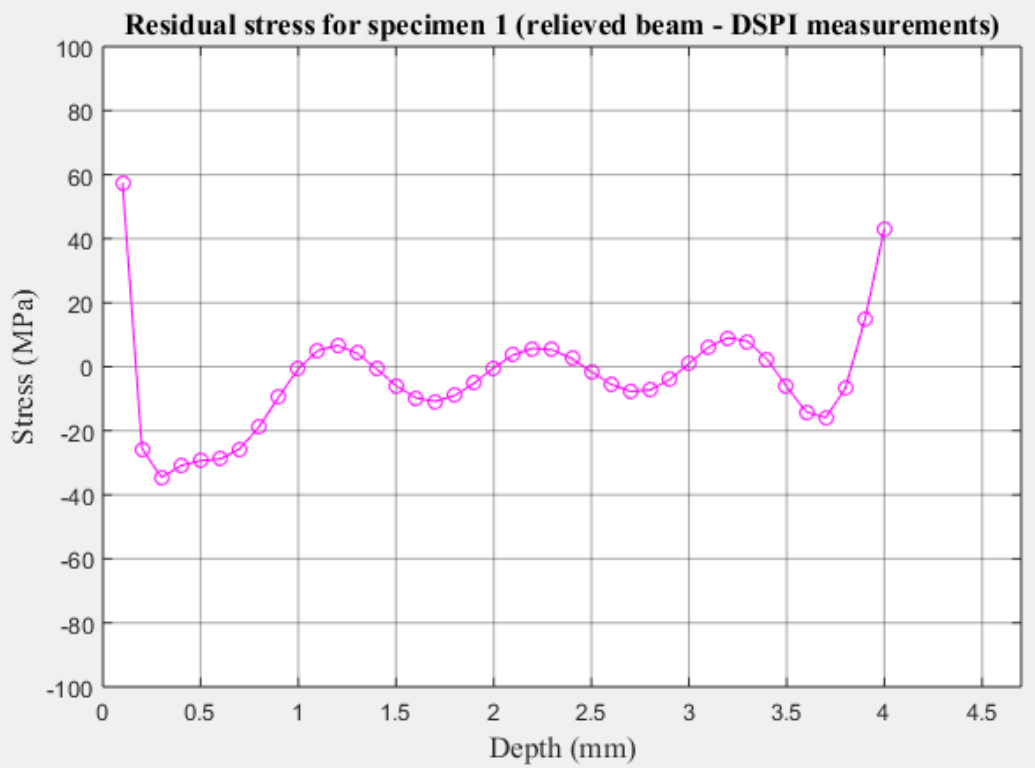

Figure 4.1. Residual stress profile as function of depth for specimen 1.

In order to compare the solution obtained with Legendre polynomials, it is also presented the residual stress distribution for specimen 1, calculated using unite pulse functions (described in section 2.3.3.2). This result was provided by PRIME, M. B., early developer of

the slitting method. He used the measured strains of Table 3.3 and the procedure described in [38]. Figure 4.2 shows the residual stress profiles estimated by both approaches.

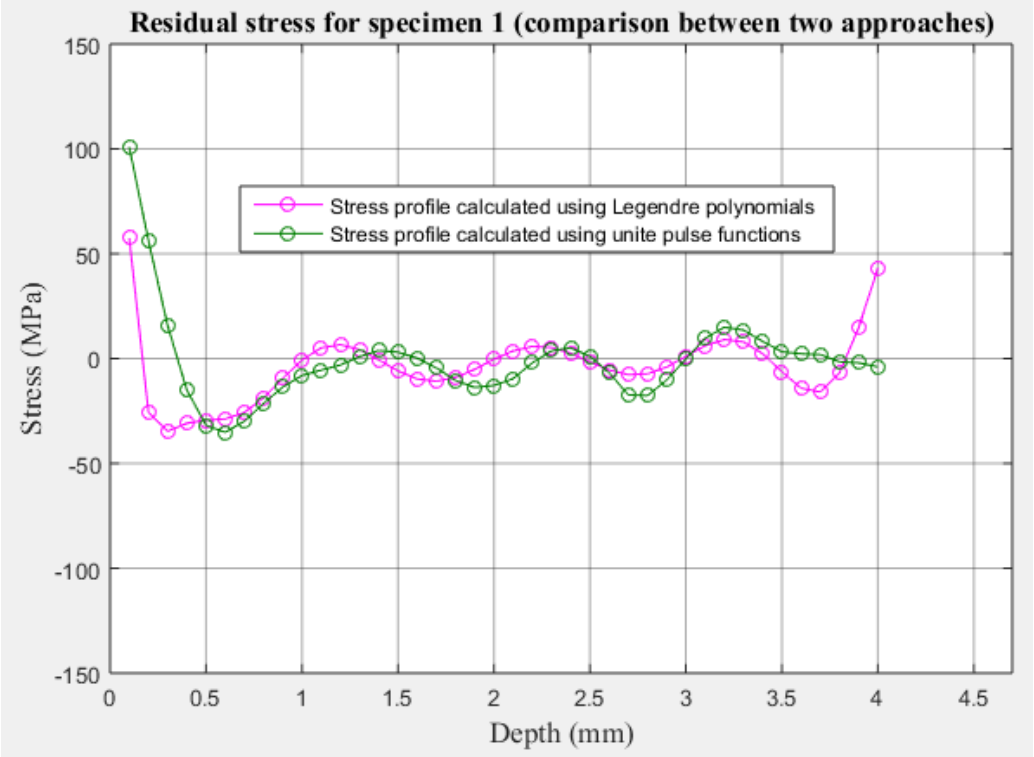

Figure 4.2. Residual stress distributions as function of depth for specimen 1. Comparison of the results estimated using both, Legendre and unite

Figure 4.3 shows the stress profiles presented above, and the near-surface stress distributions obtained by the hole-drilling method.

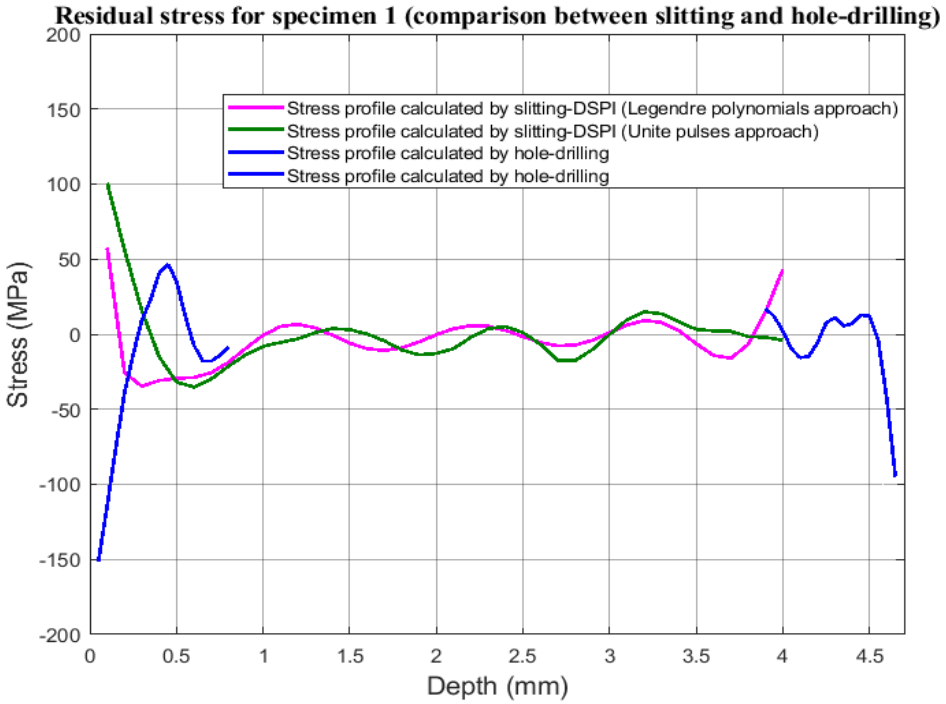

Figure 4.3. Residual stress distributions as function of depth for specimen 1. Comparison between slitting and hole-drilling results.

4.3 Experiment 2: slitting-DSPI (loaded beam)

For specimen 2, the vector of measured strains $\{\varepsilon_{meas}\}$ in Equation 2.12 contains the 40 strain values of Table 3.4. Figure 4.4 shows the residual stress distribution as function of the specimen thickness (calculated with Equation 4.2) and the expected profile of the bending process to which the beam was subjected (described in section 3.2).

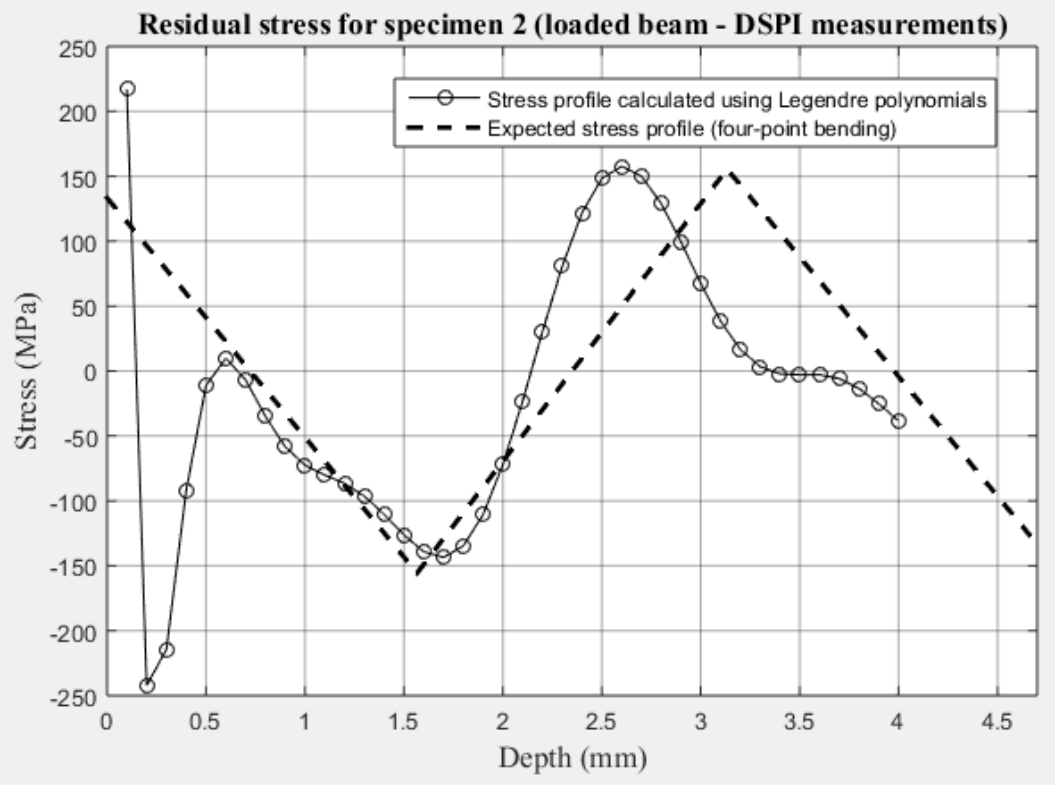

Figure 4.4. Residual stress profiles as function of depth for specimen 2. Comparison between expected and calculated distribution.

As for the specimen 1, PRIME, M. B. provided the residual stress distribution for specimen 2 estimated with unite pulse functions. This time he used the measured strains of Table 3.4. Figure 4.5 shows the residual stress profiles for specimen 2 estimated by both approaches.

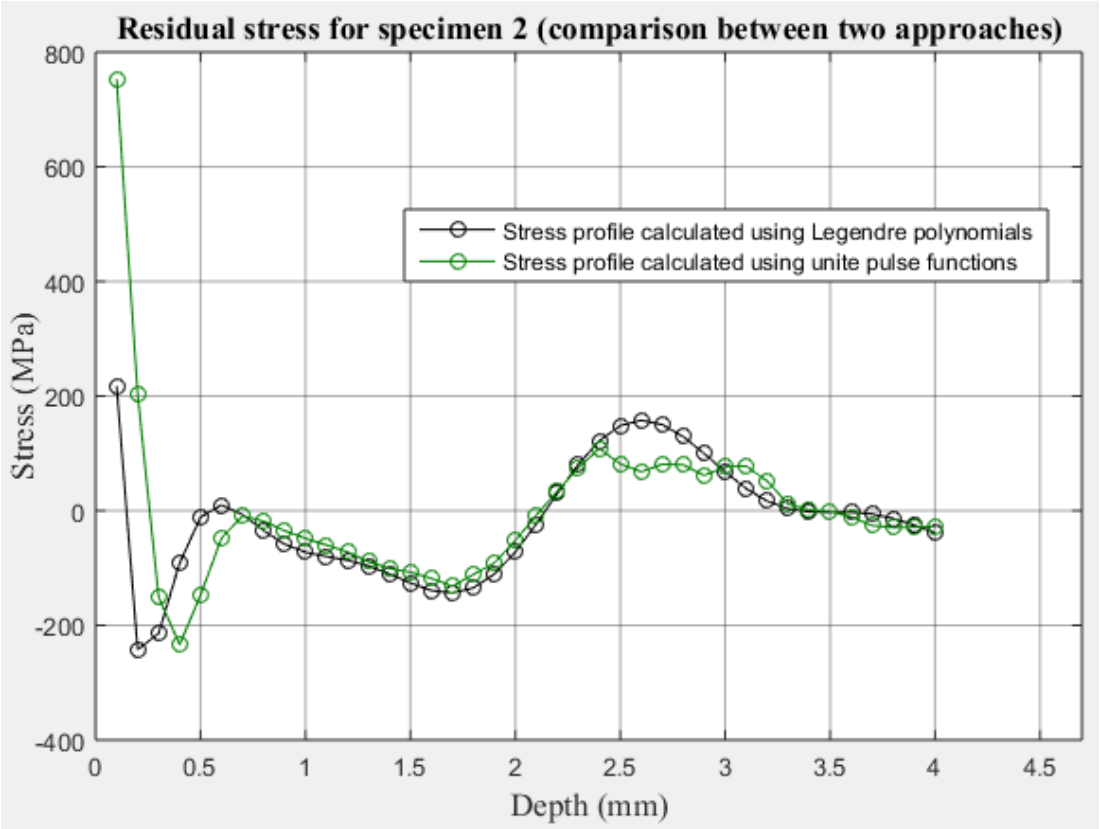

Figure 4.5. Residual stress distributions as function of depth for specimen 2. Comparison of the results estimated using both, Legendre and unite pulse approaches.

Figure 4.6 shows the stress profiles presented above, and the near-surface stress distributions obtained by the hole-drilling method.

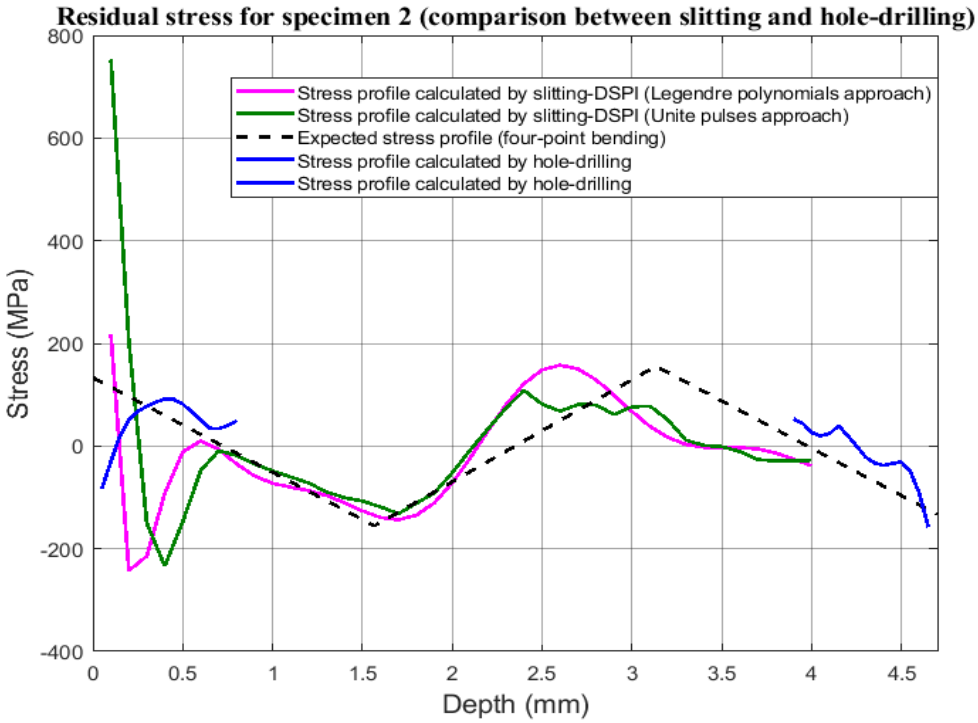

Figure 4.6. Residual stress distributions as function of depth for specimen 2. Comparison between slitting and hole-drilling results.

4.4 Experiment 3: slitting-strain gage (loaded beam)

For specimen 3, the vector of measured strains $\{\varepsilon_{meas}\}$ in Equation 2.12 contains the 40 strain values of Table 3.5. Figure 4.7 shows the residual stress distribution as function of the specimen thickness (calculated with Equation 4.2) and the expected profile of the bending process to which the beam was subjected (described in section 3.2).

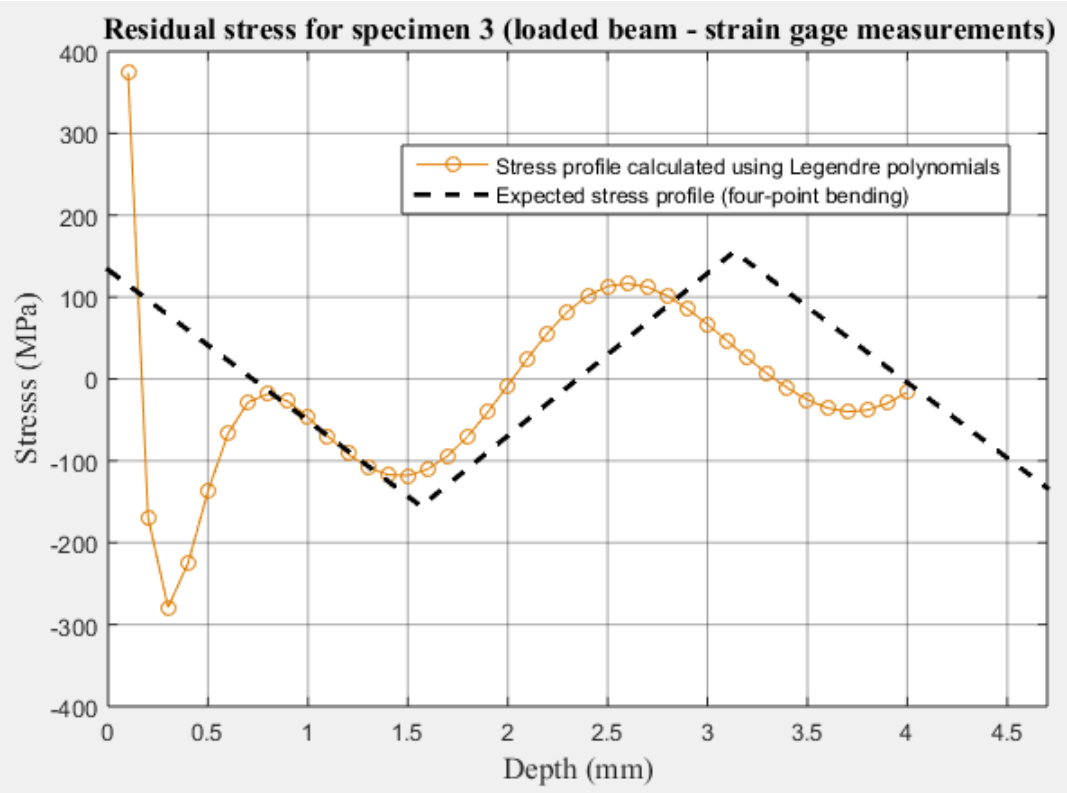

Figure 4.7. Residual stress profiles as function of depth for specimen 3. Comparison between expected and calculated distribution.

Finally, Figure 4.8 shows the stress profiles obtained in the three experiments following the procedure described in section 4.1.

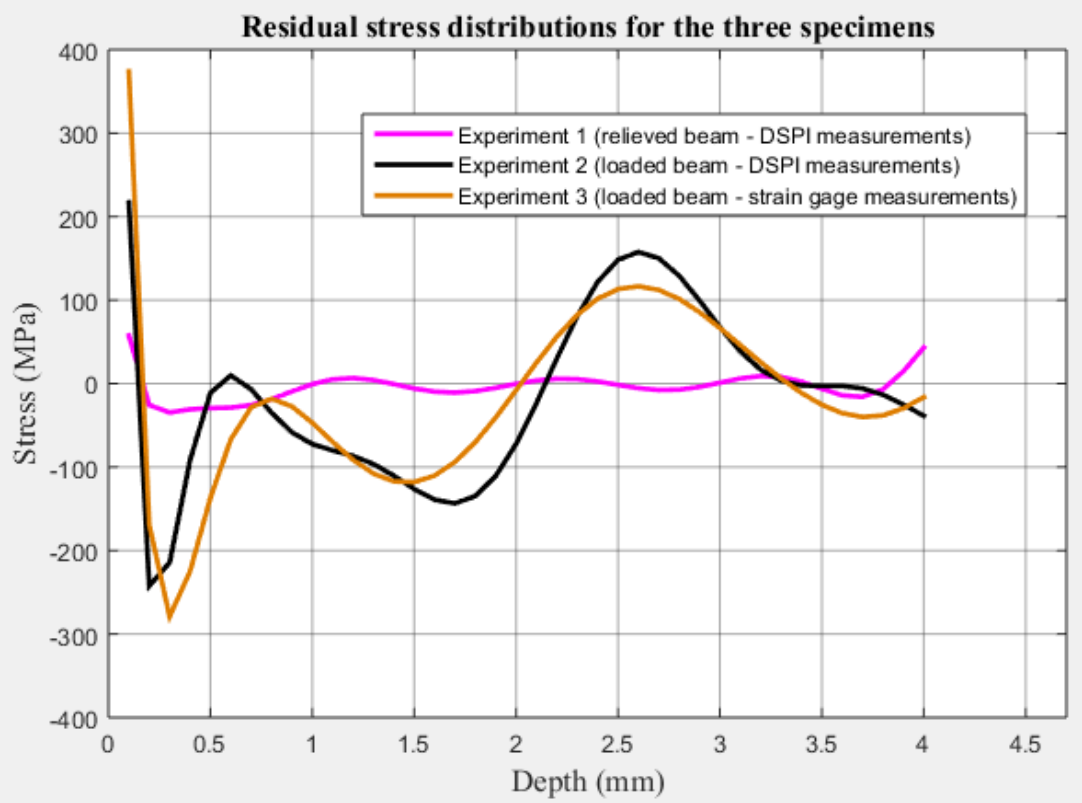

Figure 4.8. Residual stress profiles as function of depth for the three specimens. The profiles were estimated using Legendre polynomials.

4.5 Discussion

The result of experiment 1 (Figure 4.1) depicts low levels of residual stresses, mostly less than 20 MPa magnitude with higher near-surface stresses (almost 60 MPa). This low level of stress is expected because the specimen was subjected to a stress-relief treatment.

Moreover, as Figure 4.2 shows, the profile obtained with Legendre polynomials and the profile calculated by PRIME, M. B. agree significantly. That is good since the unite pulse approach has successfully demonstrated excellent results [38]. Therefore, taking as reference the unite pulse solution, it is seen that the stress-relieved profile was properly approximated by the 12^{th} order truncated Legendre polynomial.

However, Figure 4.3 shows discrepancy between the residual stresses estimated by slitting and those obtained by the hole-drilling method. In the first 0.2 mm approximately, the hole-drilling measured compressive stresses while the slitting measurements were tensile magnitudes. This exposes two important issues. First, the stresses estimated at this depth by

slitting were probably introduced by the cutting process, and two, considering the highest stress magnitudes (150 MPa) measured by the hole-drilling method, the normalizing treatment apparently did not relieve completely the near-surface region.

On the other hand, Figure 4.4 shows that the profile calculated for specimen 2 follows the expected trend for a plastically bent beam, except at the first slitting steps. This reinforces the presumption that stresses calculated at the beginning of the cut were introduced by the milling cutter. The differences after 0.5 mm are probably due to errors that arose from the application of load through the bending fixture to the specimen. In this work was used a commercial four-point bending system with fixed loading noses and knife edges supports (see Figure 3.2). This feature can affect the expected result since unwanted torsional forces could be present in the process, thus deviating from a state of pure bending [57]. This problem could be minimized by using a loading fixture having rollers instead of fixed noses, as described in [58]. It is also important to mention that the expected profile was calculated using theoretical values of Young's modulus and yield strength, which were provided by the beam manufacturer. The difference after 0.5 mm between the expected profile and that measured could also be due to the mechanical properties used in the numerical simulation. Therefore, it makes sense to think that the values provided by the manufacturer do not represent exactly the real material properties of the samples.

As for specimen 1, the Legendre approximation matches the distribution obtained by PRIME, M. B. (see Figure 4.5). However, as depicted in Figure 4.6, both estimations (Legendre and unite pulse) differ from the hole-drilling result in the first 0.5 mm. This discrepancy confirms the poor result obtained by slitting at the first cut increments.

Moreover, Figure 4.6 also shows significant differences in the first 0.2 mm between the hole-drilling result and the expected profile. A possible explanation for this discrepancy could be related to the near-surface compressive stresses that were not relieved by the normalizing treatment and that remain after the four-point bending. Another possible explanation would be related to unwanted stresses introduced in the near-surface region as consequence of friction or excessive indentation caused by the loading noses of the bending fixture [57].

Regarding to experiment 3, it can be seen that the obtained profile also follows the expected trend, except in the first 0.7 mm (Figure 4.7). Moreover, Figure 4.8 shows that the

stress distribution calculated with strain gage measurements (experiment 3) matches that calculated with DSPI measurements (experiment 2). This is a good result because shows that the slitting method combined with DSPI is able to provide a very similar result to that obtained using strain gages. However, the higher initial stresses calculated for specimen 3, confirms that at least in this work, the stresses calculated by the slitting method at the first steps are not realistic. On the other hand, analyzing the three distributions obtained in the experiments (Figure 4.8), it can be seen that all the profiles have the same behavior at the first cut increments, that is, larger tensile stress that rapidly become compressive. This strange behavior may be caused by cutting-induced stresses at the beginning of the cut. Here is important to mention that the cutting process always presented a lot of vibration and was very noisy. Therefore, it makes sense to think that maybe the milling cutter is introducing some stresses in the first slitting steps.

5 CONCLUSIONS AND SUGESTION FOR FUTURE WORK

In this work was evaluated the feasibility of the slitting method combined with DSPI to measure through-thickness residual stresses in steel beam specimens. Although it was possible to validate the proposed methodology, it is clear that improvements in the experimental procedure should be done in order to achieve better results.

The relevant conclusions resulting from the experiments are:

- The interferometer used in this work was able to measure the deformations due to slitting. This can be seen in Figure 3.22, where DSPI measurements closely agree with the strain gage measurements for the same type of specimen (loaded beams).
- The residual stress profiles calculated in experiments 1 and 2 by using 12^{th} order truncated Legendre polynomial are similar to those provided by PRIME, M. B. (see Figures 4.2 and 4.5). This demonstrates the suitability of the implemented approximation.
- Experiment 1 (Figure 4.2) showed low levels of residual stresses in the specimen. This was expected as consequence of the stress-relief treatment to which the beam was subjected.
- As shown in Figure 4.8, the profiles obtained for the loaded beams are very similar. Therefore, it is possible to conclude that there are not relevant differences between the traditional slitting measurement (by using strain gage) and the slitting-DSPI technique presented here.
- Although the stress distributions obtained in experiments 2 and 3 (Figures 4.4 and 4.7) did not match the expected values exactly, they followed the general trend and magnitudes of the profile, and after 0.5 mm approximately, the loaded specimens looked like plastically bent beams.
- The discrepancy between the expected profile and the stresses measured at the first steps (Figures 4.4 and 4.7) suggest that these initial stresses are affected by a unexpected factor, probably coming from the additional residual stress introduced by the milling cutter at the beginning of the cut.

- The residual stresses obtained by the hole-drilling method reveal two facts. First, as shown in Figure 4.3, the normalizing treatment did not relieve the near-surface stresses completely. And second, as depicted in Figure 4.6, the four-point bending did not introduce the expected magnitudes in the first 0.2 mm approximately. This error needs to be examined further, but is probably due to non-relieved compressive stresses that remain after the four-point bending, or maybe due to unwanted forces arising from the friction between the loading noses and the specimen's surface.

Three main actions are suggested to improve the methodology presented in this work:

- Design and construct a more compact and robust cutting device to make the process more stable and, thus do not induce unwanted stresses. This device should have an accessory to suck the chips created during the cutting increments in order to improve the quality of the captured images.
- Design and construct a four-point bending system capable to provide a state of pure bending in the specimens, minimizing the loading errors. This fixture must have rollers instead of fixed noses to properly load the beams.
- Investigate others materials that could be used as specimens in order to reduce the compressive residual stresses in the near-surface region measured by the hole-drilling, and therefore approximate to the ideal simulated condition.

REFERENCES

[1] WORLD ENERGY COUNCIL. **WORLD ENERGY RESOURCES**. London, United Kingdom, 2016.

[2] FMC TECHNOLOGIES. **PETROBRAS RONCADOR**. Access at September 19, 2018. http://www.fmctechnologies.com/en/SubseaSystems/GlobalProjects/South%20America/Brazil/PetrobrasRoncador.aspx?tab={8B96B00C-6FA5-47BF-BB1F-736A045B35E7}.

[3] WEPPENAAR, N; ANDERSEN, B. **INVESTIGATION OF TENSILE ARMOR WIRE BREAKS IN FLEXIBLE RISERS AND A METHOD FOR DETECTION**. Denmark: NOV Flexibles, 2014.

[4] FERNANDO, U. e*t al.* **EVOLUTION OF RESIDUAL STRESS IN TENSILE ARMOUR WIRES OF FLEXIBLE PIPES DURING PIPE MANUFACTURE**. ASME 2017 36th International Conference on Ocean, Offshore and Arctic Engineering. Norway, 2017.

[5] GAUTAM, M. **HYBRID COMPOSITE WIRES FOR TENSILE ARMOUR IN FLEXIBLE RISERS**. Thesis (Doctoral) – University of Manchester. United Kingdom, 2016.

[6] SCHAJER, G. S. **PRACTICAL RESIDUAL STRESS MEASUREMENT METHODS**. United Kingdom: John Wiley & Sons Ltd, 2013.

[7] REVIE, R. W. **OIL AND GAS PIPELINES: INTEGRITY AND SAFETY HANDBOOK**. New Jersey, United States: John Wiley & Sons Ltd, 2015.

[8] PRIME, M. B. **RESIDUAL STRESS MEASUREMENT BY SUCCESSIVE EXTENSION OF A SLOT: THE CRACK COMPLIANCE METHOD.** LA-UR-98-3857, United States: Los Alamos National Laboratory Report, 1999.

[9] CHENG, W; FINNIE, I. **RESIDUAL STRESS MEASUREMENT AND THE SLITTING METHOD.** New York, United States: Springer, 2007.

[10] PRIME, M. B. **EXPERIMENTAL PROCEDURE FOR CRACK COMPLIANCE (SLITTING) MEASUREMENT OF RESIDUAL STRESS.** LA-UR-03-8629, United States: Los Alamos National Laboratory Report, 2003.

[11] VIOTTI, M. R; KAUFMANN, G. H. **ACCURACY AND SENSITIVITY OF A HOLE DRILLING AND DIGITAL SPECKLE PATTERN INTERFEROMETRY COMBINED TECHNIQUE TO MEASURE RESIDUA STRESSES**. *Optics and lasers in engineering*, 2004.

[12] SIROHI, R. S. **INTRODUCTION TO OPTICAL METROLOGY.** Boca Raton, United States**:** CRC Press, 2015.

[13] GASVIK, K. J. **OPTICAL METROLOGY**. 3rd ed. United Kingdom: John Wiley & Sons Ltd, 2002.

[14] DONGES, A; NOLL, R. **LASER MEASUREMENT METROLOGY: FUNDAMENTALS AND APPLICATIONS.** New York, United States: Springer, 2015.

[15] HOFFMAN, D; ISMAIL, N. M; NIELSEN, R. **DESIGN OF FLEXIBLE MARINE RISERS IN DEEP AND SHALLOW WATER**. 23rd Annual Offshore Technology Conference. Houston, United States, 1991.

[16] BAI, Y; BAI, Q. **SUBSEA PIPELINES AND RISERS**. United Kingdom: Elsevier, 2005.

[17] COOEC SUBSEA. **SUBSEA UMBILICAL INSTALLATION**. Access at august 17, 2018. http://www.cooecsubsea.com/CoreBusiness/SURF/8.html.

[18] NOV COMPLETION & PRODUCTION SOLUTIONS. **FLEXIBLE PIPE SYSTEMS**. Access at august 17, 2018. http://www.nov.com/Segments/Completion_and_Production_Solutions/Subsea_Production_Systems/Flexible_Pipe_Systems/Designing_Flexible_Pipes/Materials_and_Profiles/Materials_and_Profiles.aspx.

[19] 4SUBSEA. **UN-BONDED FLEXIBLE RISERS – RECENT FIELD EXPERIENCE AND ACTIONS FOR INCREASE ROBUSTNESS**. Norway, 2013.

[20] HERMMAN. **REINFORCED FLAT WIRE RIGID ARMOURING MACHINE OF SUBMARINE FLEXIBLE PIPE PRODUCTION LINE**. Access at September 12, 2018. https://www.wire-cablemachine.com/sale-10437499-reinforcedflat-%20wire-rigid-armouring-machine-of-submarine-flexible-pipe-production-line.html.

[21] OFFSHORE TECHNOLOGY REPORT - OTO 98 019. **GUIDELINES FOR INTEGRITY MONITORING OF UN-BONDED FLEXIBLE PIPE**. Health & Safety Executive, 1998.

[22] PIPA, D. e*t al.* **FLEXIBLE RISER MONITORING USING HYBRID MAGNETIC/OPTICAL STRAIN GAGE TECHNIQUES THROUGH RLS ADAPTIVE FILTERING**. EURASIP Journal on Advances in Signal Processing, 2010.

[23] SÆVIK, S; THORSER, M.J. **TECHNIQUES FOR PREDICTING TENSILE ARMOR BUCKLING AND FATIGUE IN DEEP WATER FLEXIBLE RISERS**. 31st International Conference on Ocean, Offshore and Artic Engineering. Rio de Janeiro, Brazil, 2012.

[24] ØSTERGAARD, N.H; LYCKERGAARD, A; ANDREASE, J.H. **ON LATERAL BUCKLING FAILURE OF ARMOUR WIRES IN FLEXIBLE PIPES**. 30th International Conference on Ocean, Offshore and Artic Engineering. Rotterdam, The Netherlands, 2011.

[25] TOTTEN, G; HOWES, M; INOUE, T. **HANDBOOK OF RESIDUAL STRESS AND DEFORMATION OF STEEL**. United States: ASM International, 2002.

[26] AMERICAN SOCIETY FOR TESTING AND MATERIALS. **ASTM E837-13a: STANDARD TEST METHOD FOR DETERMINING RESIDUAL STRESSES BY THE HOLE-DRILLING STRAIN-GAGE METHOD.** United States, 2013.

[27] VIOTTI, M. R; ALBERTAZZI, A. G. **COMPACT SENSOR COMBINING DIGITAL SPECKLE PATTERN INTERFEROMETRY AND THE HOLE-DRILLING TECHNIQUE TO MEASURE NONUNIFORM RESIDUAL STRESS FIELDS**. *Optical Engineers*, May 7, 2013.

[28] TREUTING, R. G; READ, W. T. **A MECHANICAL DETERMINATION OF BIAXIAL RESIDUAL STRESS IN SHEET MATERIALS**. *Journal of applied physics*, 1951.

[29] PRIME, M. B. **CROSS-SECTIONAL MAPPING OF RESIDUAL STRESSES BY MEASURING THE SURFACE CONTOUR AFTER A CUT**. *Journal of Engineering Materials and Technology, Volume 123, 2001.*

[30] BRAGG, W.H; BRAGG W.L. **THE REFLECTION OF X-RAYS BY CRYSTALS**. *Proceedings of The Royal Society A*, 1913.

[31] CHENG, W; FINNIE, I. **THE CRACK COMPLIANCE METHOD FOR RESIDUAL STRESS MEASUREMENT**. *Welding in the World*, 1990.

[32] VAIDYANATHAN, S; FINNIE, I. **DETERMINATION OF RESIDUAL STRESS FROM STRESS INTENSITY FACTOR MEASUREMENTS**. *Journal of Basic Engineering*, 1971.

[33] LEE, K. J; HILL, M. R. **INTRALABORATORY REPEATABILITY OF RESIDUAL STRESS DETERMINED BY THE SLITTING METHOD**. *Society for Experimental Mechanics*, 2007.

[34] RANKIN, J. E; HILL, M. R. **MEASUREMENT OF THICKNESS-AVERAGE RESIDUAL STRESS NEAR THE EDGE OF A THIN LASER PEENED STRIP**. *Journal of Engineering Materials and Technology*, 2003.

[35] HILL, M. R; LIN, W. **RESIDUAL STRESS MEASUREMENT IN A CERAMIC-METALLIC GRADE MATERIAL**. *Journal of Engineering Materials and Technology*, 2001.

[36] HODGSON, D. Z. L; SMITH, D. J; SHTERENLIKHT, A. **RESIDUAL STRESS MEASUREMENT IN STEEL BEAMS USING THE INCREMENTAL SLITTING TECHNIQUE**. United States: International Centre for Diffraction Data, 2009.

[37] PRIME, M. B; HILL, M. R. **UNCERTAINTY ANALYSIS, MODEL ERROR AND ORDER SELECTION FOR SERIES-EXPANDED, RESIDUAL STRESS INVERSE SOLUTION.** *Journal of Engineering Materials and Technology*, 2006.

[38] SCHAJER, G. S; PRIME, M. B. **USE OF INVERSE SOLUTIONS FOR RESIDUAL STRESS MEASUREMENT**. *Journal of Engineering Materials and Technology*, 2006.

[39] BUECKNER, H. F. **THE PROPAGATION OF CRACKS AND THE ENERGY OF ELASTIC DEFORMATION**. *Transactions of the American Society of Mechanical Engineers*, 1958.

[40] LEE, M. J; HILL, M. R. **EFFECT OF STRAIN GAGE LENGTH WHEN DETERMINING RESIDUAL STRESS BY SLITTING**. *Journal of Engineering Materials and Technology*, 2007.

[41] RITCHIE, D; LEGGATT, R. H. **THE MEASUREMENT OF THE DISTRIBUTION OF RESIDUAL STRESSES THROUGH THE THICKNESS OF A WELDED JOINT**. *Strain*, 1987.

[42] MONTAY, G. e*t al.* **TWO DIMENSIONS RESIDUAL STRESSES ANALYSIS THROUGH INCREMENTAL GROOVE MACHINING COMBINED WITH ELECTRONIC SPECKLE PATTERN INTERFEROMETRY.** *Society for experimental mechanics*, 2008.

[43] CHENG,W; FINNIE, I; GREMAUD, M; PRIME, M. B**. MEASUREMENT OF NEAR SURFACE RESIDUAL STRESSES USING ELECTRIC DISCHARGE WIRE MACHINING**. *Journal of Engineering Materials and Technology*, 1994.

[44] MILAN, M. T. e*t al.* **SLOT MACHINING EFFECTS ON RESIDUAL STRESS MEASUREMENTS USING THE CRACK COMPLIANCE METHOD**. *Journal of Testing and Evaluation*, 2006.

[45] MATERIAL SCIENCE CENTRE. **RESIDUAL STRESS MEASUREMENT USING THE SLITTING METHOD**. The University of Manchester.

[46] RASTOGI, P. K. **DIGITAL SPECKLE PATTERN INTERFEROMETRY AND RELATED TECHNIQUES**. John Wiley & Sons Ltd, 2001.

[47] VIOTTI, M. R.; ALBERTAZZI, A. G. **ROBUST SPECKLE METROLOGY: TECHNIQUES FOR STRESS ANALYSIS AND NDT**. Washington, United States: SPIE, 2014.

[48] HECHT, E. **OPTICS**. 4th ed. United States: Adisson-Wesley, 2002.

[49] GOODMAN, J. W. **SPECKLE PHENOMENA IN OPTICS: THEORY AND APPLICATIONS**. United States: Roberts and Company, 2006.

[50] LEENDERTZ, J. A. **INTERFEROMETRIC DISPLACEMENT MEASUREMENT ON SCATTERING SURFACES UTILIZING SPECKLE EFFECT**. *Journal of Physics E: Scientific Instruments*, 1970.

[51] SCHWIDER, P. e*t al.* **DIGITAL WAVE-FRONT MEASURING INTERFEROMETRY: SOME SYSTEMATIC ERROR SOURCES**. *Applied Optics*, 1983.

[52] GHIGLIA, D. C; ROMERO, L. A. **ROBUST TWO-DIMENSIONAL WEIGHTED AND UNWEIGHTED PHASE UNWRAPPING THAT USES FAST TRANSFORM AND ITERATIVE METHODS**. *Journal of the Optical Society of America*, 1994.

[53] AN, W. **INDUSTRIAL APPLICATIONS OF SPECKLE TECHNIQUES: MEASUREMENT DEFORMATION AND SHAPE**. Doctoral Thesis, Royal Institute of Technology. Stockholm, 2002.

[54] DOWLING, N. **MECHANICAL BEHAVIOR OF MATERIALS (4TH EDITION)**. United States: Pearson, 2013.

[55] VIOTTI, M. R; ALBERTAZZI, A. G; KAPP, W. **EXPERIMENTAL COMPARISON BETWEEN A PORTABLE DSPI DEVICE WITH DIFFRACTIVE OPTICAL ELEMENT AND A HOLE DRILLING STRAIN GAGE COMBINED SYSTEM**. *Optics and lasers in engineering*, 2008.

[56] KC SOUL TOOLS. **CATALOGO 2017**. Brazil, 2017.

[57] BARATA, I. **REQUIREMENTS FOR FLEXURE TESTING OF BRITTLE MATERIALS**. Massachusetts, Unite States: Army materials and mechanics research center, 1982.

[58] MAYVILLE, R. S; FINNIE, I. **UNIAXIAL STRESS-STRAIN CURVES FROM A BENDING TEST**. United States: *Experimental Mechanics*, 1981.